UNIVERSIDADE FEDERAL DE SANTA CATARINA
CENTRO TECNOLÓGICO
PROGRAMA DE PÓS-GRADUAÇÃO EM ENGENHARIA MECÂNICA

João Humberto Serafim Martins

ANÁLISE TERMOECONÔMICA DE ARRANJOS DE ARMAZENAMENTO DE CALOR SENSÍVEL EM CENTRAIS HELIOTÉRMICAS

THERMOECONOMIC ANALYSIS OF SENSIBLE HEAT STORAGE ARRANGEMENTS FOR CONCENTRATED SOLAR POWER FACILITIES

Florianópolis
2021

João Humberto Serafim Martins

ANÁLISE TERMOECONÔMICA DE ARRANJOS DE ARMAZENAMENTO DE CALOR SENSÍVEL EM CENTRAIS HELIOTÉRMICAS

Dissertação submetida ao Programa de Pós-Graduação em Engenharia Mecânica da Universidade Federal de Santa Catarina para a obtenção do título de mestre em Engenharia Mecânica.

Orientador: Prof. Júlio César Passos, Dr. Eng.

Florianópolis
2021

Ficha de identificação da obra elaborada pelo autor,
através do Programa de Geração Automática da Biblioteca Universitária da UFSC.

Martins, João Humberto Serafim
Análise termoeconômica de arranjos de armazenamento de calor sensível em centrais heliotérmicas / João Humberto Serafim Martins ; orientador, Júlio César Passos, 2021.
150 p.

Dissertação (mestrado) - Universidade Federal de Santa Catarina, Centro Tecnológico, Programa de Pós-Graduação em Engenharia Mecânica, Florianópolis, 2021.

Inclui referências.

1. Engenharia Mecânica. 2. Energia solar concentrada. 3. Armazenamento de energia térmica. 4. Análise paramétrica. 5. Termoeconomia. I. Passos, Júlio César. II. Universidade Federal de Santa Catarina. Programa de Pós-Graduação em Engenharia Mecânica. III. Título.

João Humberto Serafim Martins

ANÁLISE TERMOECONÔMICA DE ARRANJOS DE ARMAZENAMENTO DE CALOR SENSÍVEL EM CENTRAIS HELIOTÉRMICAS

O presente trabalho em nível de mestrado foi avaliado e aprovado por banca examinadora composta pelos seguintes membros:

Prof. Júlio César Passos, Dr. Eng.
Presidente - Universidade Federal de Santa Catarina

Prof. Vicente de Paulo Nicolau, Dr.
Universidade Federal de Santa Catarina

Prof. Eduardo Lucas Konrad Burin, Dr. Eng.
Universidade Federal do Paraná

Prof. Mario Henrique Macagnan, Dr. Eng.
Universidade do Vale do Rio dos Sinos

Roberto Miguel Gutierrez Velasquez, Dr. Eng.
Facto Energy

Certificamos que esta é a **versão original e final** do trabalho de conclusão que foi julgado adequado para obtenção do título de mestre em Engenharia Mecânica.

Documento assinado digitalmente
Paulo de Tarso Rocha de Mendonca
Data: 09/02/2022 08:32:29-0300
CPF: 149.822.691-49
Verifique as assinaturas em https://v.ufsc.br

Coordenação do Programa de
Pós-Graduação em Engenharia Mecânica

Documento assinado digitalmente
Julio Cesar Passos
Data: 08/02/2022 17:46:58-0300
CPF: 550.357.447-87
Verifique as assinaturas em https://v.ufsc.br

Prof. Júlio César Passos, Dr. Eng.
Orientador

Florianópolis, 06 de dezembro de 2021.

I dedicate this work to my best friends and greater
examples; my beloved parents,
Estela and Carlos.

ACKNOWLEDGEMENTS

Although this work outlines only my name as the author, it is the product of collective effort, resulting from experiences I had, and interactions with people who have crossed my path over the last few years, to whom I sincerely express my gratitude. Of these, first I would like to thank my family, especially my parents, who have had so much patience and affection for me and, without a doubt, are the ones responsible for my curiosity and will to learn, as well as the main ones responsible for my worldview and character.

Afterward, I would like to convey my gratitude to professor Júlio César Passos who, from the first moment, supported my ideas, gave me exceptional guidance, attention, and valuable advice. I also extend these gratitude to the Federal University of Santa Catarina and all its professionals, which provided me with quality teaching and a welcoming environment, which has been my second home for the last eight years. Notably, that is only possible thanks to Brazilian society as a whole, which has been harshly financing its functioning, and to whom I am also eternally grateful.

I acknowledge the immense satisfaction of participating in the R&D project "Development and implementation of a 0.25 MW thermosolar power plant" for the Brazilian National Agency of Electric Energy (ANEEL) public call for R&D projects N° 019/2015. I thank Dr. Roberto Miguel Gutierrez Velásquez, Facto Energy, CGT Eletrosul, and Eudora Energia. They provided a fundamental role in my development as a researcher and engineer. Furthermore, I thank the Coordination for the Improvement of Higher Education Personnel (CAPES) for the financial support provided throughout this whole period.

I am thankful to Dr. Hans-Peter Wolf and STEAG Energy Services. They kindly granted me a license of their software, EBSILON Professional, as well as the continuous comprehensive support, without which this work would not be accomplished.

Next, I would also like to thank my new and old friends who have accompanied me during this journey and supported me much more than they can imagine. Finally, as most important, I would like to thank my sweetheart, who has always been by my side and encouraged me to never give up.

"The machine does not isolate man from the great problems of nature
but plunges him more deeply into them."

Antoine de Saint-Exupéry (1900-1944)

RESUMO

Entre as principais estratégias definidas para proporcionar a descarbonização da economia global, definidas no âmbito do Acordo de Paris em 2015, está a progressiva eletrificação do setor energético em um horizonte de poucas décadas, com a substituição da geração termelétrica convencional, altamente dependente de combustíveis fósseis, por fontes renováveis. Como consequência, prevê-se uma demanda de soluções de armazenamento de energia em grande escala para possibilitar a integração de fontes de geração intermitente e garantir suprimento de energia seguros e estáveis. Inserido nesse contexto, este estudo foca na comparação de arranjos de armazenamento de calor sensível empregados em usinas heliotérmicas (*Concentrated Solar Power* – CSP), apontadas como uma tecnologia que desempenhará um papel importante na transição energética. Para isso, foram realizadas simulações computacionais em um horizonte anual, por meio do software EBSILON Professional, considerando plantas CSP com coletores de calhas parabólicas (*Parabolic Trough Collectors* – PTCs) com capacidade útil de 125 MW_e, localizadas em Bom Jesus da Lapa (BA). Essas simulações visaram estimar o desempenho de quatro configurações de usina: as duas primeiras, com campo solar convencional, utilizando óleo sintético como fluido de transferência de calor (*Heat Transfer Fluid* – HTF), sendo uma com sal fundido como fluido de armazenamento térmico (*Heat Storage Medium* – HSM) empregado em um sistema indireto de duplo tanque (I2T), e outra sem capacidade de armazenamento; já as duas últimas, com na configuração de aquecimento direto de sais fundidos (*Direct Molten Salt* – DMS), empregando sal fundido como HTF, com uma alternativa também empregando-o em um sistema de armazenamento direto de duplo tanque (D2T), e outra sem capacidade de armazenamento. Em seguida, realizou-se uma análise paramétrica entre combinações de múltiplo solar (*Solar Multiple* – SM) e capacidade do sistema de armazenamento de energia térmica (*Thermal Energy Storage* – TES) para obter o menor custo nivelado de energia (*Levelized Cost of Energy* – LCOE) em cada arranjo. Para a configuração com óleo térmico e I2T, o menor LCOE foi de 16,77 ¢USD^{-1}, para um SM de 2,04 e capacidade de armazenamento de 2,42 h. Já sem armazenamento, esse custo foi de 17,14 ¢USD^{-1}, para um SM de 1,74. Por sua vez, na configuração com sal fundido e D2T, o menor LCOE foi de 14,18 ¢USD^{-1}, obtido para uma planta com SM de 3,00 e TES de 12,00 h, enquanto sem armazenamento esse valor foi de 17,38 ¢USD^{-1}, para um SM de 1,76. Tais resultados apontam grandes benefícios econômicos provenientes da utilização de sistemas de armazenamento de energia em centrais heliotérmicas, como a redução do LCOE e incremento da geração anual, fator de capacidade e receita, em detrimento de um maior custo de capital (*Capital Expenditure* – CAPEX). Além disso, ao comparar os arranjos de armazenamento de calor sensível, a alternativa D2T se destaca, com maior fator de capacidade e eficiência, uma vez que sua configuração otimizada apresenta maior capacidade de armazenamento a um menor LCOE que a alternativa I2T, indicando que o uso combinado de sal fundido como HTF e armazenamento na configuração D2T apresenta potencial para proporcionar uma maior competitividade para as usinas heliotérmicas de calhas parabólicas.

Palavras-chave: Energia solar concentrada. Armazenamento de energia térmica. Coletores de calhas parabólicas. Simulação quasi-dinâmica. Análise paramétrica. Termoeconomia.

RESUMO EXPANDIDO

Introdução

Para cumprir as metas do Acordo de Paris, as emissões de dióxido de carbono relacionadas à geração de energia precisam ser reduzidas em, pelo menos, 3,8% até 2050. Esse esforço requer uma mudança significativa nas atuais políticas energéticas, exigindo desde a rápida implementação de fontes de energia renovável até a descarbonização de processos industriais e de modais de transporte de cargas e passageiros, bem como uma mudança de padrões de consumo da sociedade. Como grande obstáculo para a primeira medida, há uma grande dependência das condições climáticas dentre tais tecnologias. Portanto, tanto a diversificação da capacidade instalada como a larga introdução de sistemas de armazenamento de energia são vitais para conciliar tal geração com a demanda mundial de energia.

Como consequência, o armazenamento de energia estará no centro da transição energética, prestando serviços em toda a cadeia de valor energético. A capacidade de armazenamento de energia possibilita sincronizar a disponibilidade de energia com a demanda na rede. Com as elevadíssimas participações de energia eólica e solar previstas para as próximas décadas, o armazenamento torna-se crucial para suavizar as flutuações diárias e sazonais no fornecimento de energia (IRENA, 2017).

Dentre as soluções de armazenamento de energia, destacam-se sistemas de armazenamento térmico (*Thermal Energy Storage* – TES); devido ao seu reduzido impacto ambiental e à boa interação com a energia heliotérmica (*Concentrated Solar Power* – CSP), eles apresentam um elevado potencial de desenvolvimento. Com sua capacidade de fornecer energia renovável despachável, as usinas CSP podem desempenhar um papel significativo na facilitação de participações cada vez mais elevadas de fontes intermitentes de energia (IRENA, 2019). Apesar disso, os custos dessa tecnologia ainda são um obstáculo: a geração heliotérmica tem o mais alto custo nivelado de energia dentre as renováveis.

Neste contexto, o presente estudo desenvolve a modelagem de plantas CSP de calhas parabólicas (*Parabolic Trough Collectors* – PTC) para Bom Jesus da Lapa (BA), uma localidade com clima semiárido no Nordeste brasileiro. Foram estudadas diferentes configurações de armazenamento de energia térmica, focando na análise de sua influência no desempenho técnico e econômico da usina, e avaliando a influência dos parâmetros de projeto no custo nivelado de energia (*Levelized Cost of Energy* – LCOE) e no fator de capacidade (*Capacity Factor* – CF). Dentre as configurações estudadas estão plantas PTC convencionais e leiautes com de uso direto de sais fundidos no campo solar (*Direct Molten Salt* – DMS), ou seja, que utilizam óleo sintético e sal fundido no campo solar, respectivamente. Quanto ao sistema de armazenamento, foram estudadas plantas com sistemas de armazenamento indireto de duplo tanque (I2T) e direto de duplo tanque (D2T), bem como casos especiais sem capacidade de armazenamento.

Objetivos

Este trabalho se concentrou em investigar os benefícios do uso de sistemas de armazenamento de calor sensível em centrais heliotérmicas, bem como em avaliar a influência do tipo de fluido de transferência de calor (*Heat Transfer Fluid* – HTF) e das alternativas de integração de sistemas de armazenamento de energia no desempenho técnico e econômico de tais empreendimentos. Para isso foram traçados os seguintes objetivos específicos:

a) Dimensionar, modelar e simular plantas heliotérmicas com coletores de calhas parabólicas utilizando sistemas de armazenamento de calor sensível baseados em sais fundidos como meio de armazenamento, além de considerar leiautes de integração direta e indireta do sistema de armazenamento, bem como utilizando óleo sintético e sais fundidos como fluido de transferência de calor;
b) Investigar a influência da parâmetros de projeto no desempenho termoeconômico das plantas e obter as configurações mais competitivas através de uma análise paramétrica para diferentes dimensões de campo solar e capacidade de armazenamento de energia;
c) Obter as especificações de cada alternativa que proporcionam o menor custo nivelado de energia;
d) Comparar o desempenho técnico e econômico das diferentes plantas selecionadas.

Metodologia

A fim de realizar tais comparações, modelou-se quatro arranjos de usinas heliotérmicas de calhas parabólicas: topologia (i) – planta com óleo sintético como HTF e sal fundido como meio de armazenamento de calor (*Heat Storage Media* – HSM), empregado em um sistema de armazenamento na configuração I2T; topologia (ii) – planta com óleo sintético como HTF e sem capacidade de armazenamento; topologia (iii) – planta com sal fundido como HTF e HSM, com sistema de armazenamento na configuração D2T; topologia (iv) – planta com sal fundido como HTF e sem capacidade de armazenamento. A modelagem das plantas deu-se no software EBSILON Professional por meio de simulações de séries temporais com resolução temporal de uma hora. O local selecionado foi Bom Jesus da Lapa (BA), a localidade brasileira com a maior irradiação direta normal anual registrada, 2198 kWh m^{-2}, acima dos 2000 kWh m^{-2} muitas vezes indicados como limiar de viabilidade técnica para plantas de geração heliotérmica. Na modelagem das plantas empregou-se a metodologia do ponto de projeto, a qual proporciona uma inter-relação entre a capacidade do bloco de potência, a capacidade de armazenamento e a extensão do campo solar, calculadas em regime permanente para uma condição específica da planta, neste trabalho selecionado o meio dia solar para o solstício de verão do hemisfério Sul.

Nessas condições, a equação característica dos coletores foi utilizada para estimar a dimensão do campo solar necessária para suprir a demanda de um bloco de potência com capacidade útil de 125 MW_e. A estimativa da massa de fluido de armazenamento

necessária em cada planta baseia-se na diferença de entalpia entre os tanques quentes e frio, bem como na duração dos seus ciclos carga e descarga.

Após essas etapas, empregou-se uma análise paramétrica entre as combinações de múltiplo solar *Solar Multiple* – SM e autonomia do sistema de armazenamento de energia para obter o menor LCOE em cada topologia. Variou-se o SM entre 1 e 3 com intervalo de 0,25; já a capacidade de armazenamento foi variada 1 e 12 horas para as topologias (i) e (ii), com intervalo de uma hora, enquanto para as topologias (ii) e (iv) variou-se apenas o SM, uma vez que essas não apresentam armazenamento. O conjunto de simulações resultantes de tal variação resultou em 234 simulações – 108 para a topologia (i), 9 para a topologia (ii), 108 para a topologia (iii) e 9 para a topologia (iv).

Resultados

Os resultados das análises paramétricas indicam que os menores custos são obtidos para configurações distintas das especificadas pelo método de ponto de projeto. Para as plantas com óleo sintético, os menores LCOEs obtidos foram de 16,77 e 17,14 ¢USD kWh^{-1} para SMs de 2,04 e 1,74; com capacidades de armazenamento de 2,42 e 0 horas, para as topologias (i) e (ii), respectivamente. Já ao analisar as plantas com sal fundido como HTF, os menores LCOEs obtidos foram de 14,18 e 17,38 ¢USD kWh^{-1}; para os SMs de 3,00 e 1,76; com capacidades de armazenamento de 12 e 0 horas.

Por outro lado, na análise da utilização da capacidade instalada, as plantas com óleo sintético como HTF apresentaram os maiores CFs, de 54.39% e 38.56%, para as configurações com o maior SM avaliado (3,00), e capacidades de armazenamento de 7,72 e 0 horas, respectivamente. Para as plantas com sal fundido como HTF, os maiores CFs foram de 60.45% e 38.56%, para SMs de 3.00 e capacidades de armazenamento de 12 e 0 horas, respectivamente. A ausência de trocadores de calor no arranjo (ii) deixa evidente, a maior temperatura e consequentemente maior densidade no armazenamento de energia, o que proporciona uma maior eficiência anual, 40% e 35% para as topologias (iii) e (iv) em comparação com 31% e 29% para as topologias (i) e (ii), respectivamente.

Considerações Finais

Este trabalho aborda de uma maneira pragmática o dimensionamento e a simulação de sistemas de armazenamento de calor sensível aplicados a usinas heliotérmicas com diferentes fluidos de transferência de calor (HTFs), tendo como finalidade a comparação por um viés de termoeconomia entre plantas sem armazenamento e os dois principais arranjos de armazenamento disponíveis comercialmente, um tema extremamente atual e até o momento pouco explorado na literatura.

Com base nessa análise, foi realizado o dimensionamento, modelagem e simulação de quatro plantas: duas com campo solar baseado em óleo sintético e em outras duas com

campo solar baseado em sal fundido, além da análise de ambos os casos utilizando ou não sistemas de armazenamento. A simulação de tais arranjos de plantas se deu em um grande intervalo de múltiplos solares (SMs) e capacidades de armazenamento por meio de uma análise paramétrica, que resultou na configuração mais economicamente atrativa para cada topologia, tendo como base a métrica o LCOE.

Ao comparar tais configurações ideais, confirmou-se que o uso de sistema de armazenamento de calor sensível reduz o LCOE. Além disso, tal redução foi mais acentuada quando sal fundido é empregado como HSM, enquanto essa redução é mais modesta quando óleo sintético é utilizado. Já ao comparar o uso dos diferentes HTFs, verificou-se que sais fundidos permitem alcançar maiores temperaturas no ciclo de potência, o que traz ganhos de eficiência térmica e fotoelétrica da planta, bem como tornam desnecessária a utilização de parte dos trocadores de calor entre os circuitos hidráulicos do campo solar e do TES, aumentando o aproveitamento do calor armazenado. Com maiores temperaturas, menos massa de HSM é requerida, também diminuído os investimentos relacionados ao armazenamento. Notou-se também que, para a maioria das topologias, a configuração que minimiza o LCOE difere da que maximiza o CF, ou seja, apesar do incremento na área do campo solar e da capacidade de armazenamento da planta proporcionarem aumentos na geração de energia, eles também resultam em maiores investimentos em coletores, absorvedores, tanques, fluidos, dentre outros equipamentos. Em detrimento disso, nem sempre ao armazenar e gerar mais energia, haverá uma redução em seu custo, sendo fundamental conciliar tais requisitos de projeto por meio de otimizações. Dessa forma, os resultados encontrados estão alinhados com a tendência mundial de intensificação do uso de TES em usinas CSP e verificam que o uso de sais fundidos tanto para a absorção da energia solar, quanto para o seu armazenamento, são tecnologias promissoras para proporcionar maior competitividade para CSP.

ABSTRACT

Among the main strategies defined to provide the decarbonization of the global economy, defined under the Paris Agreement in 2015, is the progressive electrification of the energy sector, over the horizon of a few decades, with the replacement of conventional thermoelectric generation, highly dependent on fossil fuels, by renewable sources. Consequently, large-scale demand for energy storage solutions is expected to integrate intermittent generation sources into the global energy matrix and ensure a secure and stable power supply. In this context, this study focuses on the comparison of sensible heat storage arrangements employed in CSP, pointed out as an important technology in the energy transition. To this end, computer simulations were performed within an annual time horizon, using EBISILON Professional, considering PTC CSP plants with a net power of 125 MW_e, located in Bom Jesus da Lapa (BA). These simulations aimed to estimate the performance of four plant configurations: the first two, using thermal oil as HTF, with and without molten salt as HSM, employed in a I2T system; the last two, using molten salt in the solar field, and with and without a molten salt-based TES, in a D2T layout. Then, a parametric analysis was employed between combinations of SM and storage capacity to obtain the lowest LCOE in each arrangement. For the I2T configuration with storage, the lowest LCOE was 16.77 ¢USD kWh^{-1}, for an SM of 2.04 and TES with a storage capacity of 2.42 h. Whereas without storage, this cost was 17.14 ¢USD kWh^{-1}, for an SM of 1.74. In the D2T configuration with storage, the lowest LCOE was 14.18 ¢USD kWh^{-1}, obtained for a plant with an SM of 3 and a TES of 8 h, while without storage it was 17.38 ¢USD kWh^{-1}, for an SM of 1.76. The results point to large economic benefits from the use of energy storage systems in CSP plants, such as reduced LCOE and increased annual power output, capacity factor, and revenue, at the expense of higher CAPEX. When comparing the sensible heat storage arrangements, the D2T alternative stands out, with a higher capacity factor and efficiency, since its optimized configuration presents higher storage capacity at a lower LCOE than I2T, indicating the combined use of molten salt as HTF and D2T as TES can provide greater competitiveness for CSP.

Keywords: Concentrated solar power. Thermal energy storage. Parabolic trough collector. Quasi-dynamic simulation. Parametric analysis. Thermoeconomics.

LIST OF FIGURES

LIST OF TABLES

LIST OF ABBREVIATIONS AND ACRONYMS

ANEEL	Brazilian Electricity Regulatory Agency *Agência Nacional de Energia Elétrica*
BA	Bahia (Brazilian state)
BCE	before the Common Era (equivalent to before Christ)
BEIS	British Department for Business, Energy and Industrial Strategy
BES	battery energy storage
BOP	balance of plant
BUS	backup system
CAPES	Coordination for the Improvement of Higher Education Personnel *Coordenação de Aperfeiçoamento de Pessoal de Nível Superior*
CAPEX	capital expenditure
CF	capacity factor
COP21	United Nations Climate Change Conference 2015
CSP	concentrated solar power
CST	concentrated solar thermal
D2T	direct two-tank
DHI	diffuse horizontal irradiance
DLR	German Aerospace Center *Deutsches Zentrum für Luft- und Raumfahrt*
DMS	direct molten salt
DNI	direct normal irradiance
DSG	direct steam generation
DTC	direct thermocline
EBSILON	Energy Balance and Simulation of the Load response of power generating or process controlling Network structures
EPC	engineering, procurement and construction
EU	European Union
EUR	Euro (€)
FIT	feed-in tariff
GHG	greenhouse gas
HPS2	High Performance Solar 2
HSM	heat storage medium
HTF	heat transfer fluid
HVAC	heating, ventilating and air conditioning
I2T	indirect two-tank
IAM	incidence angle modifier

IPCA	extended national consumer price index *Índice Nacional de Preços ao Consumidor Amplo*
IRR	internal rate of return
ITC	indirect thermocline
LBE	lead-bismuth eutectic alloy
LCOE	levelized cost of energy
LCOS	levelized cost of storage
LFR	linear Fresnel reflector
LTES	latent thermal energy storage
MENA	Middle East and North Africa
Mio.	million (used for currencies)
NaK	sodium–potassium alloy
NPV	net present value
NREL	United States National Renewable Energy Laboratory
OPEX	operational expenditure
PB	power block
PCM	phase change material
PDC	parabolic dish collector
PPA	power purchase agreement
PSA	Plataforma Solar de Almería
PTC	parabolic trough collector
PV	photovoltaic
RS	Rio Grande do Sul (Brazilian state)
SAM	System Advisor Model
SC	Santa Catarina (Brazilian state)
SCA	solar collector assembly
SEGS	Solar Electric Generating Station
SELIC	special clearance and escrow system *Sistema Especial de Liquidação de Custódia*
SF	solar field
SHIP	solar heat for industrial processes
SM	solar multiple
SolarPACES	solar power and chemical energy systems
SP	São Paulo (Brazilian state)
SPT	solar power tower
SSP	shared socioeconomic pathways
STES	sensible thermal energy storage
SUT	solar updraft tower
TCES	thermochemical energy storage

TDC	total direct costs
TES	thermal energy storage
TIC	total indirect costs
TMY	typical meteorological year
TOA	top of atmosphere
TRL	technology readiness level
UAE	United Arab Emirates
UN	United Nations
USA	United States of America
USD	United States Dollar (US$)
VALCOE	value adjusted levelized cost of energy

LIST OF SYMBOLS

Roman alphabet

A	area	m^2
C	cost	USD or USD yr^{-1}
$CAPEX$	capital expenditure	USD
c	specific heat; specific cost	J kg^{-1} K^{-1}; USD kW^{-1}
c_p	specific heat at constant pressure	J kg^{-1} K^{-1}
c_v	specific heat at constant volume	J kg^{-1} K^{-1}
CF	capacity factor	–
E	electricity	J or Wh
f	solar field defocus; vapor extraction fraction	–
G	solar irradiance; global horizontal irradiance	W m^{-2}
G_{SC}	solar contant (1367)	W m^{-2}
H	daily solar irradiation	J m^{-2}
h	specific enthalpy	J kg^{-1}
I	hourly solar irradiation	J m^{-2}
i	i-th term	–
k_T	hourly clearness index	–
K_T	daily clearness index	–
$k_{\tau\alpha}$	incidence angle modifier	–
k	generic coefficient	–
L	length	m
$LCOE$	levelized cost of energy	¢USD kWh^{-1}
m	mass	kg
$\dot{m}$	mass flow rate	kg s^{-1}
n	quantity; n-th therm	–
$OPEX$	operational expenditure	USD yr^{-1}
P	pressure	kPa or bar
Pr	Prandtl number	–
Q	heat	J or Wh
$\dot{Q}$	heat flow rate	W
q'	length-specific heat flow rate	W m^{-1}
q''	area-specific heat flow rate	W m^{-2}
r	interest rate	–
T	temperature	K or ℃
TDC	total direct costs	USD
TIC	total indirect costs	USD
t	t-th therm	–

V	volume	m^3
v	specific volume	$m^3\ kg^{-1}$
W	work	J or Wh
z	solar azimith angle	rad or °
z_s	surface azimith angle	rad or °

Greek alphabet

α	absortivity	–
β	surface tilt angle	rad or °
Δt	timespan	s or h
ΔT	temperature difference	K
η	efficiency	–
$\eta_{opt,0}$	peak optical efficiency	–
γ_θ	intercept factor	–
Γ	coefficient in Spencer equation	–
ϕ	fraction	–
Φ	zenith angle	rad or °
π	pi (3.1415...)	–
ψ	solar azimuth angle	rad or °
ρ	density; reflectance	$kg\ m^3$; –
τ	transmittance	–
θ	incidence angle	rad or °
θ_z	zenith angle	rad or °

Subscripts

0	extraterrestrial
abs	absorber tubes
avail	available
b	beam
bel	bellows
BOP	ballance of plant
BUS	backup system
cha	storage system charge
clean	mirror cleanliness
col	solar collector
cond	condenser
cont	contingencies

CT	cold tank
d	diffuse
dis	storage system discharge
end	collector endlosses
eff	effective
EPC	engineering, procurement and construction
fix	fixed
foc	focal distance
fuel	fuel
gross	gross
heel	storage tank heel
HSM	heat storage media
HT	hot tank
HTF	heat transfer fluid
i	i-th term
impr	improvement
in	inlet
ins	insurance
land	land
loss	loss in absorbers
n	direct normal
net	net
opt	optical
out	outlet
PB	power block
pipe	loss in piping
pb	pump
row	rows between solar collector assemblies
sat	saturation
SF	solar field
shad	collector shading effect
solar	solar energy
spillage	structure deformation by windloads
t	t-th therm
TES	thermal energy storage
th	thermal
trans	transversal
turb	steam turbine
var	variable

CONTENTS

1 INTRODUCTION

Energy plays a significant role in economic prosperity and society's living standards. With the advent of the Industrial Revolution in the second half of the eighteenth century, anthropic activities became more and more dependent on fossil fuels to fulfill their ever-growing energetic needs. As a result, greenhouse gases have been discharged into the atmosphere at an unprecedented rate in history.

According to IPCC (2021), each 1000 $GtCO_2$ released into the atmosphere is likely to cause a 0.45 ± 0.18 ℃ increase in global surface temperature (see Figure 1.1). To date, yearly emission rates are about 35 $GtCO_2$ and 49 $GtCO_2e$ [(1)] for all GHGs (see Figure 1.2), accounting for a cumulative amount of 2424 $GtCO_2$, contributing to disruptions in Earth's climate and sea-level rise, as well as severe threats to fauna, flora, and human health. Nonetheless, they need to reach net-zero to mitigate global warming rapidly.

In line with the Kyoto Protocol, signed in 1992, state parties commit to reduce GHGs emissions based on the consensus that global warming is occurring due to human-made actions. More recently, in the Paris Agreement, signed at COP21, stricter agreements were reached to limit the warming up to 2℃ above pre-industrial levels. In this event, 196 representatives of UN member states committed to establishing rigid decarbonization actions.

Figure 1.3 shows the possible paths of annual energy-related CO_2 emissions and reductions according to three scenarios delineated by IRENA (2020a): the baseline energy scenario (indicated by the orange line); the planned energy scenario (yellow line); and the transforming energy scenario (blue line). Large-scale electrification and shift to renewables could deliver three-quarters of those reductions (IRENA, 2020a).

Energy-related carbon dioxide emissions need to be reduced by at least 3.8% per year from now until 2050 to set the world on a pathway towards meeting the aims of the Paris Agreement. Nevertheless, trends over the past years show annual growth of 1.3% in CO_2 emissions. If this pace were maintained, the planet's carbon budget would be largely exhausted by 2030, setting the planet on track for a temperature increase of 3℃ or more by the end of the century, as represented in the baseline energy scenario. Despite that, several countries have made efforts to implement policies and revise their targets in line with the higher deployment of clean energy technology. Most of the efforts and ambition are oriented towards increasing renewable power generation capacities, followed by energy efficiency improvement targets and a subsequent rise in electrified transport and heat applications (IRENA, 2020a).

Supposing the current pledges are met, the energy-related CO_2 yearly emissions are expected to increase until 2030, before dipping slightly by 2050 to just below today's

(1) $GtCO_2e$ stands for gigaton (1×10^6 kg) of carbon equivalent, accounting for all all greenhouse gases (GHGs).

Figure 1.1 – Average global surface temperature increase due to CO_2 emissions

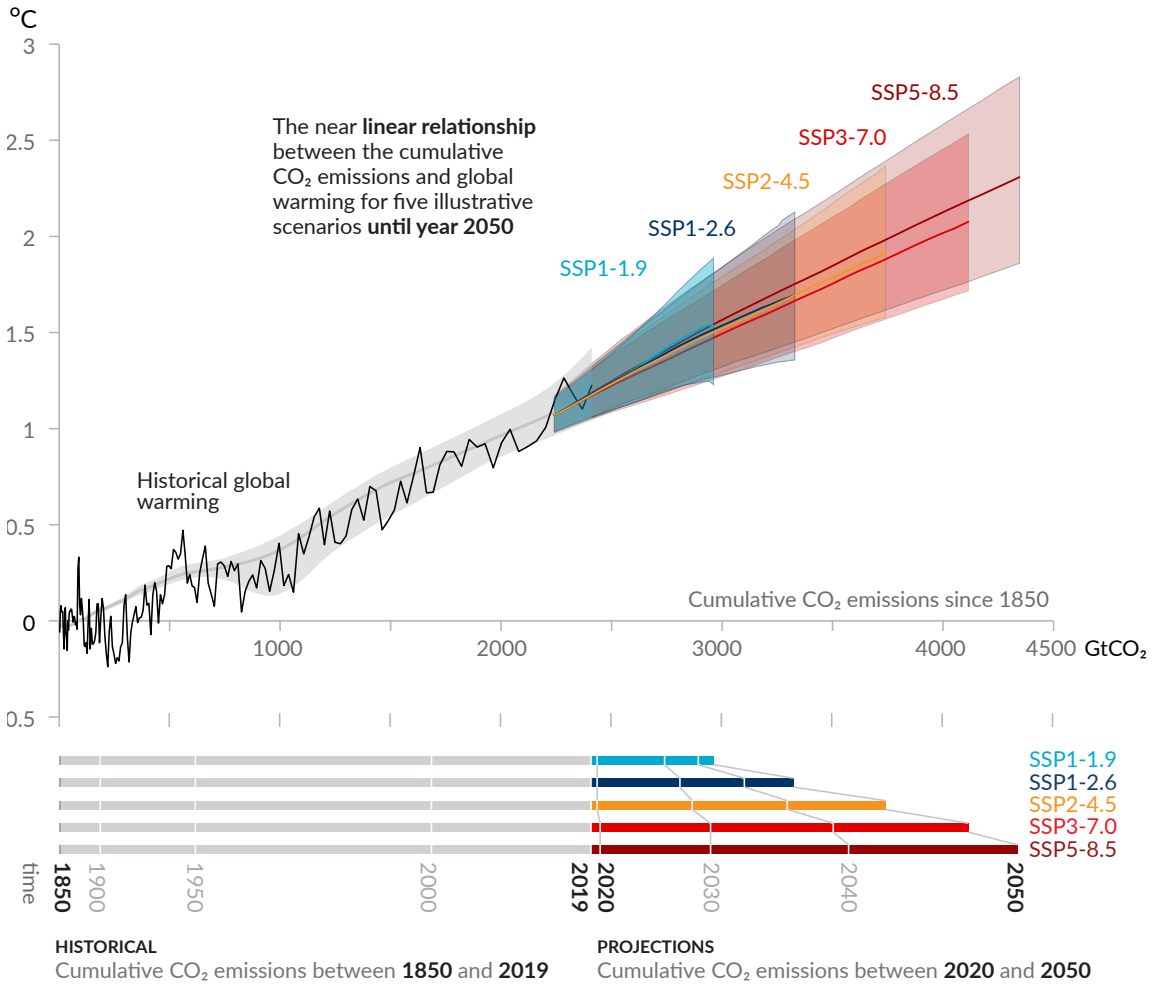

Source: IPCC (2021).

Note: The five illustrative scenarios are referred to as SSP. The first index describes the socioeconomic trends underlying the scenario, and the second to the approximate level of radiative forcing (in W m^{-2}) resulting in the year 2100.

level, as reflected in the planned energy scenario. Nevertheless, to limit the global temperature well below 2 ℃ and towards 1.5 ℃ as per the Paris Agreement targets, annual energy-related CO_2 emissions would need to fall more than 70% from now until 2050, from 35 to below 10 $GtCO_2$ (IRENA, 2020a).

This endeavor requires a significant shift at the energetic status-quo, ranging from rapid deployment of renewable power generation capacities such as wind, PV, and CSP, to deeper renewables-powered electrification of transport (e.g. [(2)], electric vehicles) and heating (e.g., heat pumps), direct renewable heat use (e.g., SHIP, biomass), energy efficiency (e.g., process improvement, thermal insulation of buildings), and infrastructure investment (e.g., power grids, flexibility measures such as storage) (IRENA, 2020a). According to IEA (2014).

As presented in Figure 1.4, nuclear energy and intermittent renewables present

(2) e.g. is short for *exempli gratia* that means "for example."

Figure 1.2 – Annual carbon dioxide emissions

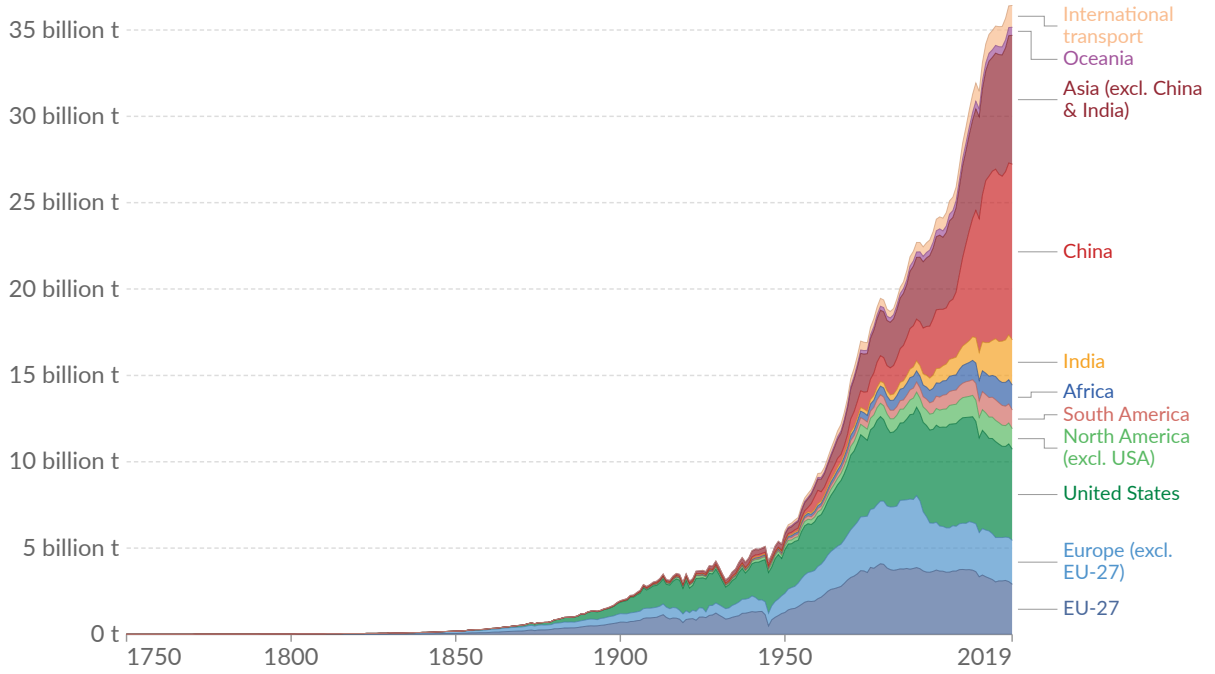

Source: Ritchie and Roser (2020a).
Note: EU-27 are the constituent members of the EU.

smaller carbon footprints. Nevertheless, the latter accounts just for 10.7% and 29.0% of energy and electricity generation, respectively, whereas the most significant share of remaining is performed fossil fuels burning (see Figure 1.5) (RITCHIE; ROSER, 2020b).

The transforming energy scenario presented by IRENA (2020a) is focused on energy-related CO_2 emissions reductions, which make up around three-quarters of global GHGs emissions (see Figure 1.6) (RITCHIE; ROSER, 2020a). According to it, a climate-friendly pathway requires a reduction to 9.5 $GtCO_2$ of remaining energy-related emissions by mid-century (see Figure 1.3). Of the remainder, under one-quarter would be emitted for electricity generation and transport, one-third in industry, 5% in buildings, and 15% in other sectors. It can be performed by a mass deployment of renewables, changing their share in the global energy mix from 11% in 2020 to 66% in 2050, with a increase in their participation in the electricity mix from around 29% to 86% in the same period Ritchie and Roser (2020b) and IRENA (2020a).

Beyond that date, further efforts will also be needed, and emissions will need to reach net-zero. The solutions needed to these further reductions have yet to be thoroughly analyzed, although some solutions are in sight. In the transport sector, freight, air, and shipping could be decarbonized through a mix of electrification, biofuels, carbon-neutral synthetic fuels, and green hydrogen. In industry, synthetic materials from biomass and CO_2 could replace petrochemical products. Zero-carbon steel and chemical industries would need to be achieved through a circular economy and hydrogen and biomass feedstocks. Most buildings would need zero energy through high efficiency

Figure 1.3 – Annual energy-related carbon dioxide emissions in different scenarios

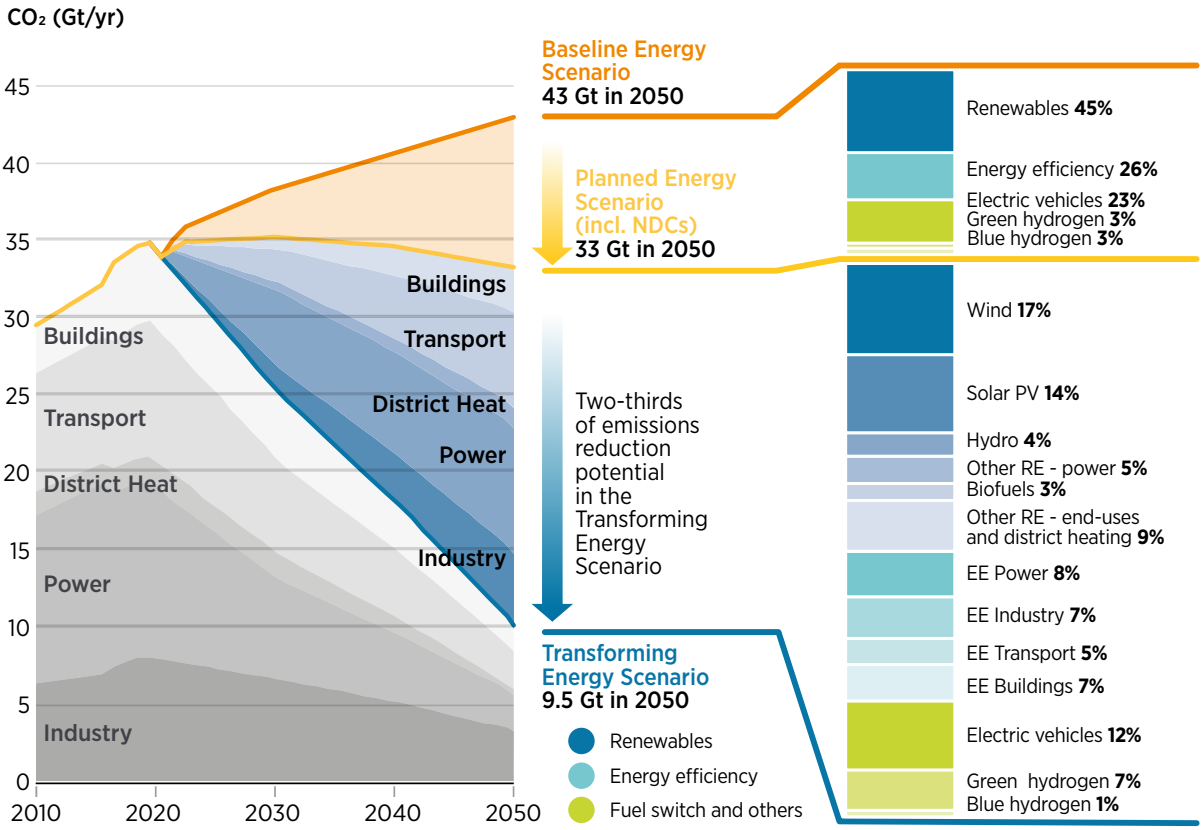

Source: IRENA (2020a).
Note: The percentages account for the emissions reduction between scenarios due to a policy or technology deployment.

and building-integrated renewables. Innovative and sustainable city and infrastructure planning would need to become omnipresent.

Most renewable sources have a greater or lesser degree of dependence on weather conditions, such as radiation to support solar plants, favorable winds for wind generation, and rainfall to refilling hydroelectric reservoirs and irrigating crops for biofuels production. Therefore, to conciliate such generation with the world's energy demand, both the diversification of the installed capacity and the introduction of large-scale energy storage systems are vital.

Energy storage will be at the heart of the energy transition, providing services throughout the energetic value chain. Electricity storage capacity can reduce constraints on the transmission network and can defer the need for significant infrastructure investment. Along with providing multiple services and user benefits, an electricity storage project can unlock multiple revenue streams by synchronizing energy dispatch and peak demand. With the very high electricity shares of wind and solar power expected beyond 2030 (70-80% in some estimates), the need for energy storage becomes crucial to smooth daily and seasonal fluctuations in energy supply (IRENA, 2017).

Although pumped hydro storage is the largest single source of electricity storage

Figure 1.4 – Carbon footprint by energy source

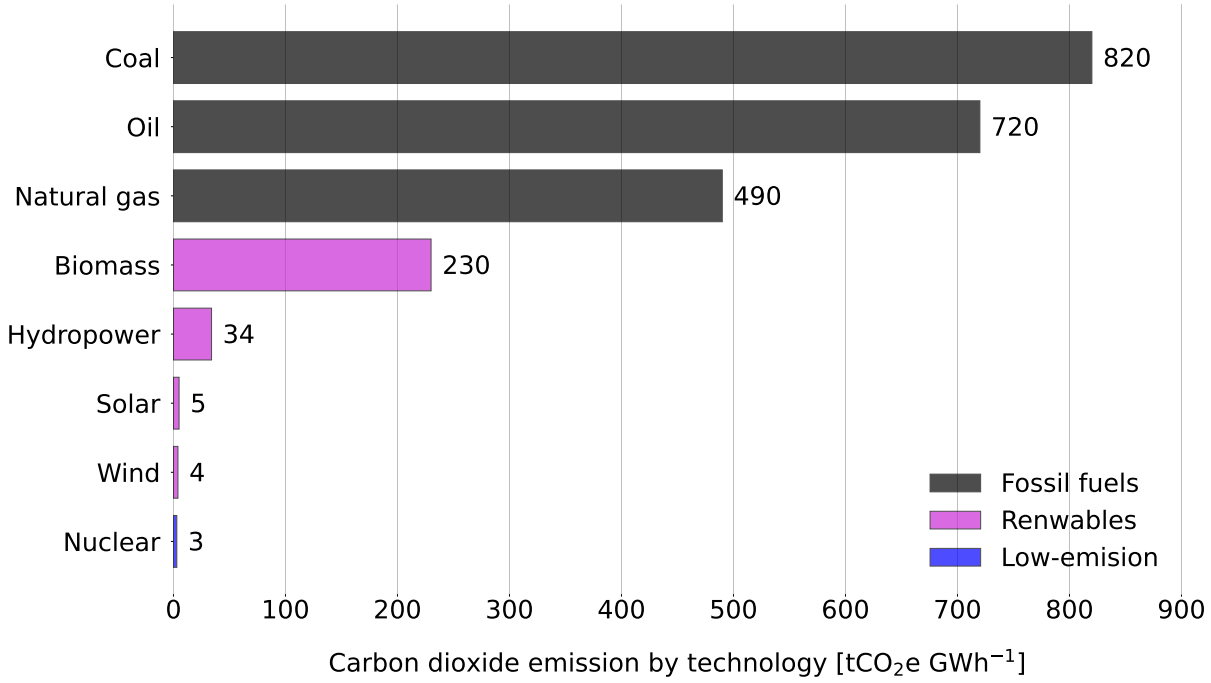

Source: Elaborated using Matplotlib (HUNTER, 2007) with data from Ritchie and Roser (2020a).
Note: Biomass emissions range from 78-230 $tCO_2e\ GWh^{-1}$.

Figure 1.5 – Global energy and electricity mixes

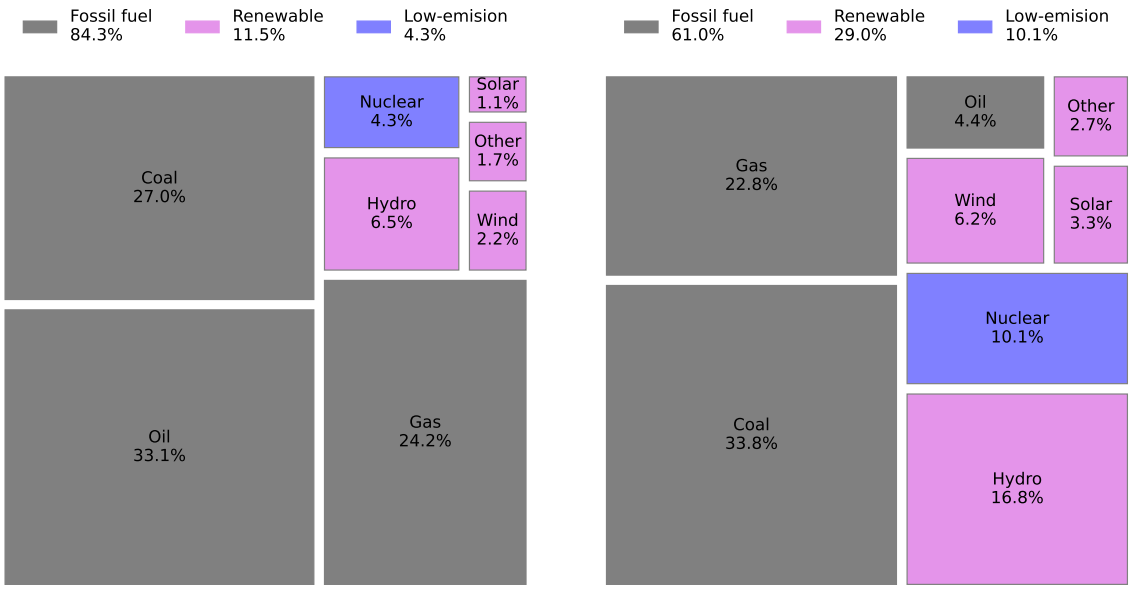

(a) Energy mix (b) Electricity mix

Source: Elaborated using Matplotlib (HUNTER, 2007) with data from Ritchie and Roser (2020b).
Note: Other renewables include biomass, biofuels, geothermal, wave and tidal energy.

capacity today, it is a mature technology with site-specific cost. As a result, there is little potential to reduce the total installed cost from a technology perspective. Among the remaining storage solutions, hydrogen, BES, and TES stand out (IRENA, 2017).

Figure 1.6 – Greenhouse gases emissions by economic activity

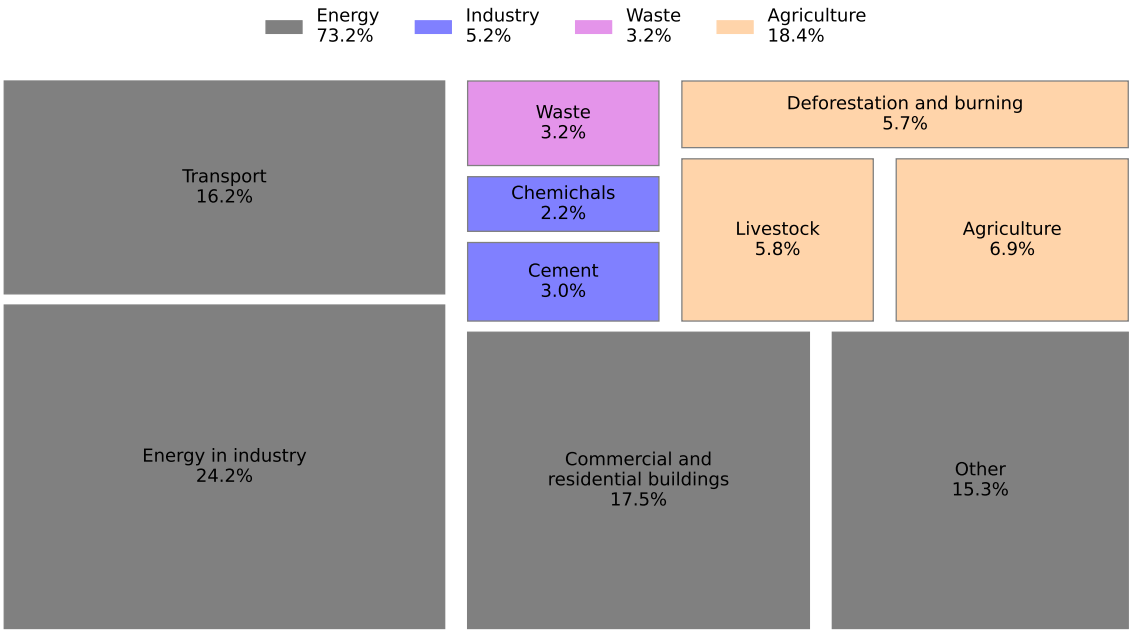

Source: Elaborated using Matplotlib (HUNTER, 2007) with data from Ritchie and Roser (2020a).

Most hydrogen is produced by steam reforming of natural gas, partial oxidation of methane, and coal gasification, as it emits GHGs, it is called gray hydrogen. The blue variety is made similarly, but carbon capture technologies prevent GHGs releases. Turquoise hydrogen is produced via methane pyrolysis. In contrast, green hydrogen results in zero carbon emissions. It is produced using water electrolysis powered by renewables, therefore being pointed out as an essential alternative for decarbonization (IRENA, 2020b).

These technologies provide a high storage density, facilitating energy transport and stocking. Therefore, it is feasible to replace fossil fuels in economic sectors in which electrifying is challenging, such as maritime and air transport (see Figure 1.7). Due to all these characteristics, it already accounts for many underway initiatives for large-scale deployment (IRENA, 2020b).

Besides that, batteries are considered one of the most suitable approaches for energy storage. BES systems are developing rapidly with falling costs and improving performance. By 2030, the installed costs of battery storage systems could fall by 50-66%. Extensive research exists for different technologies and applications of BES; however, they have not yet reached economic feasibility for large-scale installations (AKINYELE; RAYUDU, 2014), and their environmental impacts remain a significant challenge that still requires development (IRENA, 2017).

Similarly, TES systems can store heat or cold to be used later, involving three basic steps: charge, storage, and discharge, giving a complete storage cycle. Their primary use is to overcome the mismatch between energy generation and energy use,

Figure 1.7 – Green hydrogen production, conversion and end uses

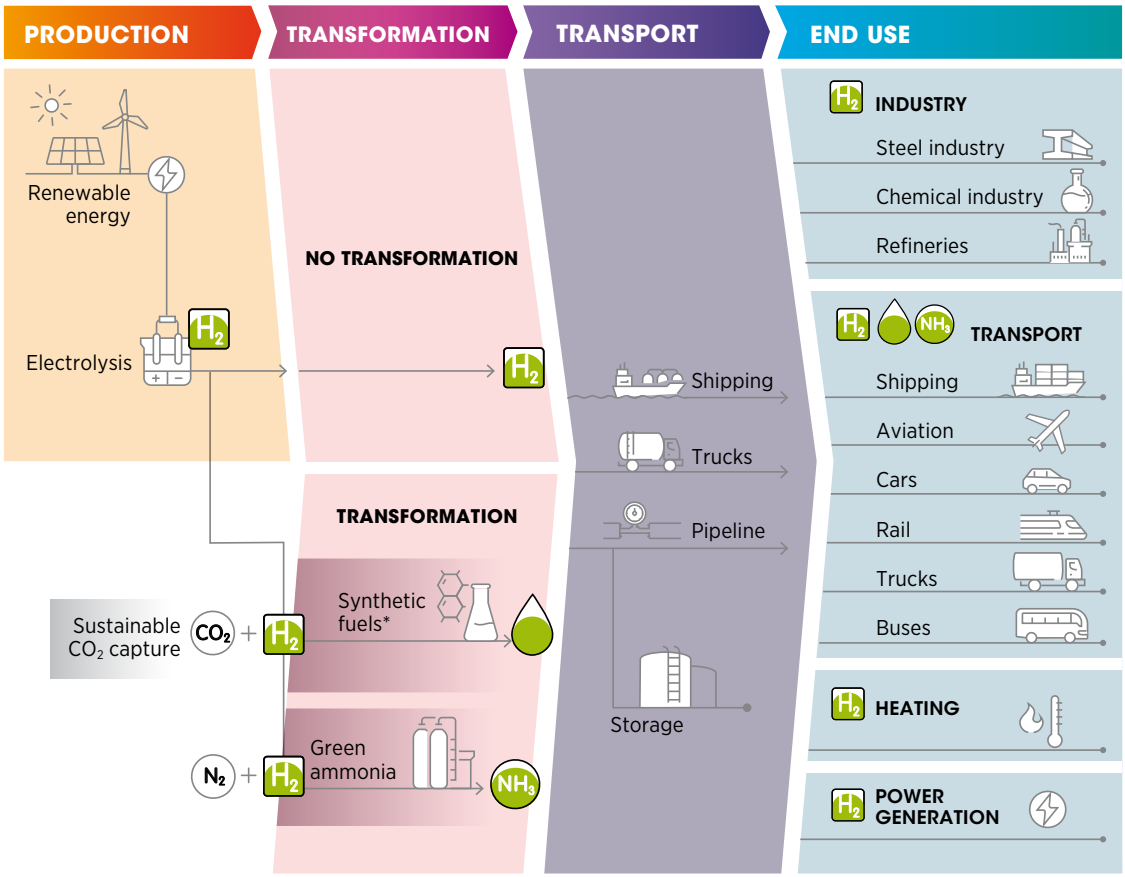

Source: IRENA (2020b).

especially in solar thermal applications (CABEZA, 2021).

As technical and economic problems and risks are reduced through proven performance, TES is expected to be accepted as an attractive option in the industrial and commercial sectors that will lead to ensuring energy security, increasing energy efficiency, and environmental benefits. TES has been identified as a method for substantially reducing peak electrical demands, an important feature to lessen power shortages in the future. In addition, TES provides a potentially economic means of using waste heat and climatic energy resources to meet a significant portion of our growing needs for heating and cooling, especially for industrial facilities and commercial buildings. Environmental benefits also follow TES in many applications (DINÇER; ROSEN, 2011).

The combined use of concentrating solar collectors and heat engines enables thermal, mechanical, and electrical energy harnessing from the Sun. Different from other renewables, with CSP, there are no complicated silicon manufacturing processes, as in PV modules; no deep holes to drill, as in geothermal systems; and sky-high structures that need constant maintenance, as in wind power. According to IEA (2014), CSP plants avoided merely 8 $MtCO_2$ during 2013. Yet, they can be responsible for emission reductions up to 2.1 $GtCO_2$ yr^{-1} in 2050.

Moreover, in contrast to other intermittent renewables, CSP holds a distinguished potential for TES integration. While the conventional design of solar plants is mainly focused on high process efficiency, market requirements increasingly target operating flexibility due to the continuing shift towards renewables.

Solar thermal energy technologies can also extract helpful heat to residential acclimatization, water heating, and power low-temperature (bellow 150 ℃) industrial processes via flat plates and evacuated tubes (HAHN et al., 2017). On the other hand, concentrating collectors enable higher operating temperatures, with applications, from electricity generation, to supply heat for medium (between 150 and 400 ℃) and high-temperature (above 400 ℃) industrial processes.

These industrial applications are commonly called CST or SHIP. They are of high interest since a large part of industrial demand is thermal energy. This economic sector holds great potential for decarbonization and integration with renewables. Hahn et al. (2017) bring an in-depth analysis of such perspectives for the Brazilian economy. The most suitable industrial niches for integrating solar thermal energy are beverage and foods, paper and cellulose, chemical, and textile, all with great vapor demands in low and medium temperatures. Furthermore, it was also concluded that there is a good spatial correlation between appropriate DNI and industrialized areas, which provides favorable conditions for this integration.

According to SolarPACES (2021), there are currently 113 operational CSP projects, accounting for 6.4 GW, meanwhile in Brazil, there are no currently operational CSP plants. Despite that, the country has invested in research activities involving this technology. As an example, it is possible to point out the pilot plants in the scope of the Public Calls for R&D Projects 19/2015 by ANEEL, such as the Porto Primavera solar thermal power plant, in Rosana (SP), without storage and with a rated capacity of 0.580 MW_e (GAZOLI et al., 2018), and the Passo São João solar thermal power plant, in Roque Gonzales (RS), with a power block rated capacity of 0.125 MW_e and oil-based direct thermocline storage, with 1.5 hours of capacity (MARTINS et al., 2020).

In the last decade, the weighted average LCOE of CSP plants fell by 68%, from 34.00 ¢USD kWh^{-1} to 10.80 ¢USD kWh^{-1} (see Figure 1.8a). In the same period, newly commissioned plants' weighted-average CF increased from 30% to 42% (see Figure 1.8b), with new CSP plants being built with improved technology and know-how. Moreover, recent auction and PPA results suggest it can promote decreases into the range of 7.00-8.00 ¢USD kWh^{-1}, with potential for even further reductions (IRENA, 2021). With its ability to provide dispatchable renewable power, CSP could play a significant role in facilitating ever-higher shares of variable solar and wind (IRENA, 2019).

Despite all these qualities, this technology costs are still an obstacle; CSP has the highest LCOEs among renewables, as presented in Figure 1.8a). According to

Figure 1.8 – Characteristics of newly commissioned utility-scale renewables

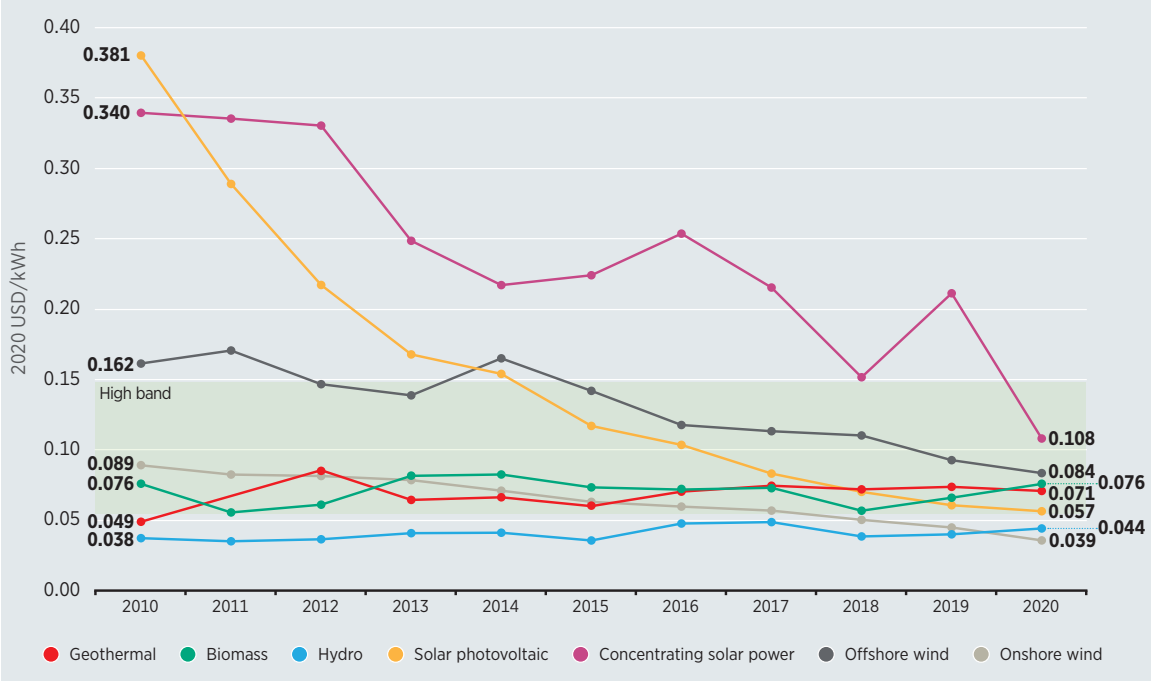

(a) Levelized cost of energy

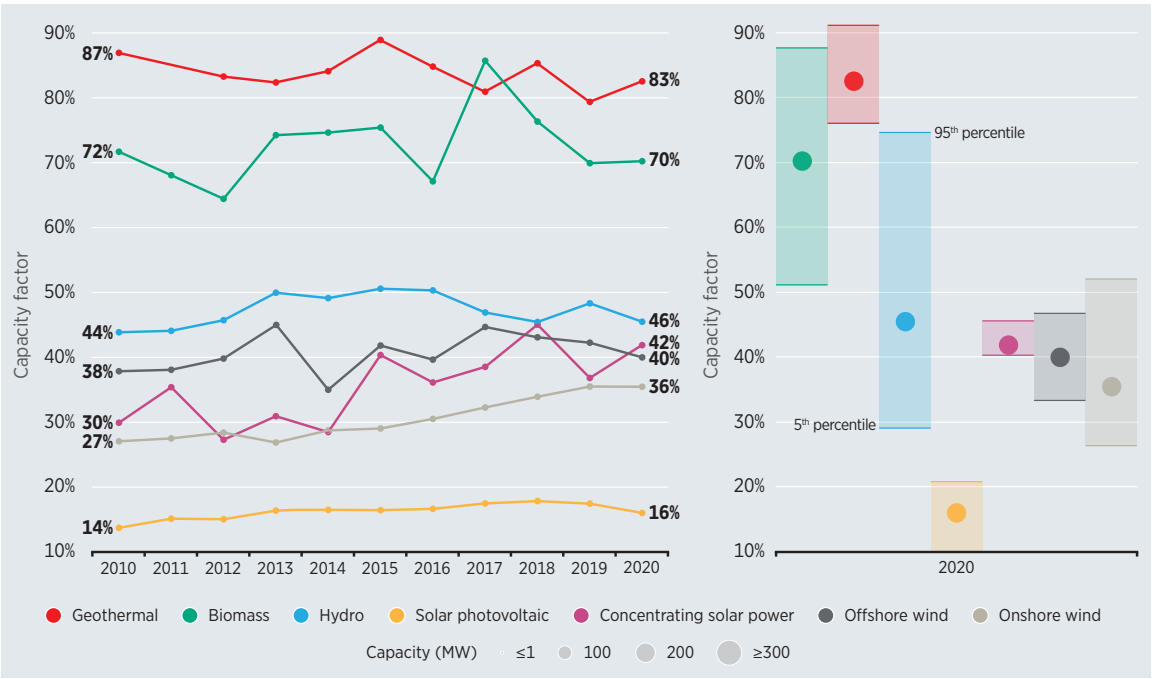

(b) Capacity factor

Source: IRENA (2021).

IRENA (2012), the key areas in which cost reductions need to be achieved are:

- *Solar field*. Mass production and cheaper components, as well as improvements in design, can help to reduce costs;
- *Heat transfer fluid*. New HTFs capable of reaching higher temperatures will help

to improve storage possibilities and reduce costs. DSG and DMS are possible breakthroughs to achieve that, with several prototypes being erected around the world;

- *Storage system*. It is closely tied to the HTF, as higher temperatures, notably from SPTs, will reduce the cost of storage;
- *Power block*. There is still room for cost reductions, although these will be more modest than the other components once these components are already highly mature.

In this context, the present study develops the modeling of CSP-PTC plants for Bom Jesus da Lapa (BA) in the Brazilian Northeastern semi-arid region. First, different TES configurations were studied, focusing on the analysis of their influence on the plant's technical and economic performance, analyzing the influence of design parameters mainly on LCOE reductions and CF increases. Then, plants with conventional and DMS configurations were analyzed, i.e. [(3)], running synthetic oil and molten salt at the solar field, respectively. As for the TES, plants with I2T and D2T arrangements were observed, as well as cases without storage capacity.

Among the analogous studies identified Montes et al. (2009a) and Marugán-Cruz et al. (2019) stand out, being used as the basis for the procedures applied in this work. The first describes a methodology to optimize the LCOE through a parametric analysis for a 50 MW_e CSP-PTC plant without storage, using oil as HTF, obtaining the lowest LCOE of 15.71 USD kWh^{-1} [(4)] for an SM of 1.16. The second study conducted a parametric analysis aiming to optimize the LCOE as a function of SM and TES capacity for a CSP-LFR-DSG 50 MW_e plant with a sensitive-latent storage system, located in Seville, Spain. It was concluded without using storage, the smallest LCOE is 13.61 ¢USD kWh^{-1}, for an SM of 1.72. It is reduced to 13.44 ¢USD kWh^{-1} when using storage, obtained for an SM of 1.99 and a storage capacity of 1.7 hours.

Another important study was carried by Lopes et al. (2021). A conventional PTC plant (using synthetic oil as HTF with a I2T salt-based storage) was compared with a facility in a DMS configuration with a D2T TES, both with a rated capacity of 50 MW_e and 7.5 full-load hours of storage. Using SAM, the study investigated pressure drops, heat transfer coefficients, anti-freezing solutions, costs, and power block design. It was concluded: (1) the pressure drops in the solar field are smaller running molten salts instead of thermal oil, thanks to higher operating temperature ranges; (2) HitecXL molten salt leads to lower parasitics consumption than Therminol VP-1 and Solar Salt; (3) a reduction of the LCOE from 17.48 ¢USD kWh^{-1}, when running HitecXL, to 18.66

[(3)] i.e. is short for *id est* that means "in other words."

[(4)] Originally in euros. Converted considering the exchange rate of 1.00 EUR = 1.18 USD, referent to September 2021.

¢USD kWh^{-1} [(5)] using Therminol VP-1 as HTF; (4) simpler power block designs can be considered for the higher operating temperatures of molten salts, resulting in higher efficiencies and lower costs.

Although the optimization methodology of LCOE through parametric analysis is widely applied in the literature, the present study differs by using this procedure to compare alternatives of STES and HTFs used in PTC plants.

1.1 MOTIVATION

This work was developed under the research and development project of the Brazilian Electricity Regulatory Agency (ANEEL) in association with CGT Eletrosul, Facto Energy, and Eudora Energia, entitled "Development and implementation of a 0.25 MW_e thermosolar power plant". It has as its primary objective the promotion of academic research activities and the elaboration of technical reports about the potential of CSP technology in Brazil.

In addition, the project foresees the construction of a pilot plant in the country's Southern region. Initially, it was planned to be installed in Laguna (SC). However, after detailed studies, it was decided to relocate it to Roque Gonzales (RS), representing a 20.7% increase in annual direct normal irradiation. Moreover, this location accounts for the Passo São João hydroelectric complex; consequently, substation structures and qualified personnel are already available, contributing to the project's cost reduction.

That CSP plant was dimensioned with a PTC solar field, using thermal oil as HTF, a power block with a nominal capacity of 0.25 MWe, and relies on a storage system to supply the power block for 1.5 full-load hours. Due to manufacturing simplicity, low cost, and small storage capacity design requirements, it was chosen. The TES configuration is unconventional, using direct thermocline; it employs a single stratified tank where the HTF is also used as HSM.

An oil-based TES was also employed in the first solar thermal plant with storage capacity constructed in 1982, Solar One. However, after a fire in 1999, the system was discontinued. It was later replaced by a salt-based system, which has become mainstream ever since, enabling higher temperatures and system efficiencies (PALACIOS et al., 2020). Since then, the use of thermal oil as HSM has fallen into disuse in CSP plants and now cannot be found in operational plants (SOLARPACES, 2021).

In addition, it has been possible to identify a few studies directly comparing the alternative TES configurations, such as salt-based thermoclines, I2T, and D2T. It contrasts to the vast material comparing different solar field technologies (PTC, SPT and LFR and PDC), as well as comparing CSP and PV plants. Because of this, the present work was planned to fill this gap and provide data to better ground this kind of

[(5)] Similar to Footnote (4).

decision.

In this regard, the present work compares two STES alternatives commercially available for CSP plants, I2T and D2T combined with DMS, also comparing them with layouts without storage for Bom Jesus da Lapa (BA), in the Brazilian semi-arid region.

1.2 SCOPE

Because of what was discussed in the previous sections, this work focuses on evaluating the benefits of using sensible heat storage systems versus plants without storage and evaluating the influence of storage alternatives on solar thermal energy developments' technical and economic performance. It was done aiming to attend the following specific objectives:

- Size, model and simulate PTC-CSP with different STES;
- Investigate the influence of design parameters on the thermoeconomic performance of the plants and obtain the configuration that provides the lowest LCOE for each storage alternative through a parametric analysis;
- Interpolate the points of the parametric analysis in order to elaborate a characteristic surface for each plant, involving SM, storage capacity and LCOE;
- Compare the technical and economic performance of the different selected plants.

1.3 DOCUMENT STRUCTURE

This document has been organized into five chapters, starting with this introduction. In Chapter 2 a literature review is done regarding CSP plants, focusing on their operating principles, as well as on their development process over the years, the description of the state of the art and future trends. It also contains a survey of the various techniques of TES, with emphasis on the HSMs, its current state of development, and applicability in CSP. That section also presents the fundamentals of simulations and thermoeconomic analysis of CSP plants, which provides the basis for the metrics chosen used in this study. In its final part, conclusions are drawn concerning the bibliography and concepts analyzed. Chapter 3 describes the methodology applied in plants modeling and thermoeconomic analyses. In that section, the CSP arrangements considered are detailed. At the end of the chapter, conclusions regarding the methodology are presented. In chapter 4 the findings of the analyses of four arrangements of STES in CSP plants are disclosed and discussed. Then, the main results are synthesized in the final part of the chapter. Finally, chapter 5 presents the final considerations, as well as recommendations for future work.

This document also includes two appendices and one annex. Appendix A contains a list of studies developed by the author throughout his Master of Science; Appendix B contains the results from the parametric analyses conducted for the CSP plants.

2 BACKGROUND AND LITERATURE REVIEW

This chapter aims to briefly introduce the main topics connected with this study, making an overview of up-to-date enterprises and bibliographies. First, the main concepts behind CSP technology are presented, giving relevance to its working principle, HTF used, main characteristics, current progress around the world, and trends for future developments. Then, TES systems are introduced and further explored, presenting their different classifications and HSM used for solar thermal applications. After that, an exploration of tools for simulating CSP plants is presented alongside relevant thermoeconomic variables definition. At the chapter's end, a summary of the bibliography explored is presented.

2.1 SOLAR ENERGY CONCEPTS

First, it is crucial to establish some nomenclature used throughout this work, which are often misused in the literature. Radiation is a broad concept, which expresses the transmission of energy through space via electromagnetic waves. On the other hand, irradiance is the areal density rate at which radiation hits on a surface, usually expressed in W m^{-2} and denoted by G. Its cumulative value over time is called irradiation, given in J m^{-2}. The irradiation for an hour and a day are expressed by the symbols I and H, respectively (DUFFIE; BECKMAN, 2013).

The irradiance at the Earth's TOA is called extraterrestrial irradiance (G_0 or G_{TOA}). According to Spencer's Equation (2.1), it fluctuates about 6.9% over the year due to the elliptical trajectory described by Earth around the Sun. Its average over the year is 1.367 kW m^{-2}, traditionally called the solar constant (G_{SC}).

$$\frac{G_0}{G_{SC}} = 1.00011 + 0.34221\cos\Gamma + 0.00128\sin\Gamma + 0.000719\cos(2\Gamma) + 0.00007\sin(2\Gamma) \quad (2.1)$$

$$\Gamma = \frac{2\pi(n-1)}{365} \quad (2.2)$$

where, n is the umpteenth day of the year (from 1 to 365).

The extraterrestrial solar radiation passes through the Earth's atmosphere, whereby it is partially absorbed or scattered by atmospheric components, such as aerosols, gases, and particles (see Figure 2.1). So, those scattering effects strongly dependent on weather conditions, more specifically, on the atmospheric clearness index (k_T and K_T for hourly and daily periods, respectively). Additionally, about 30% of the incoming extraterrestrial irradiance is reflected to space, thus without being absorbed by the atmosphere and Earth's surface.

Figure 2.1 – Solar irradiance components

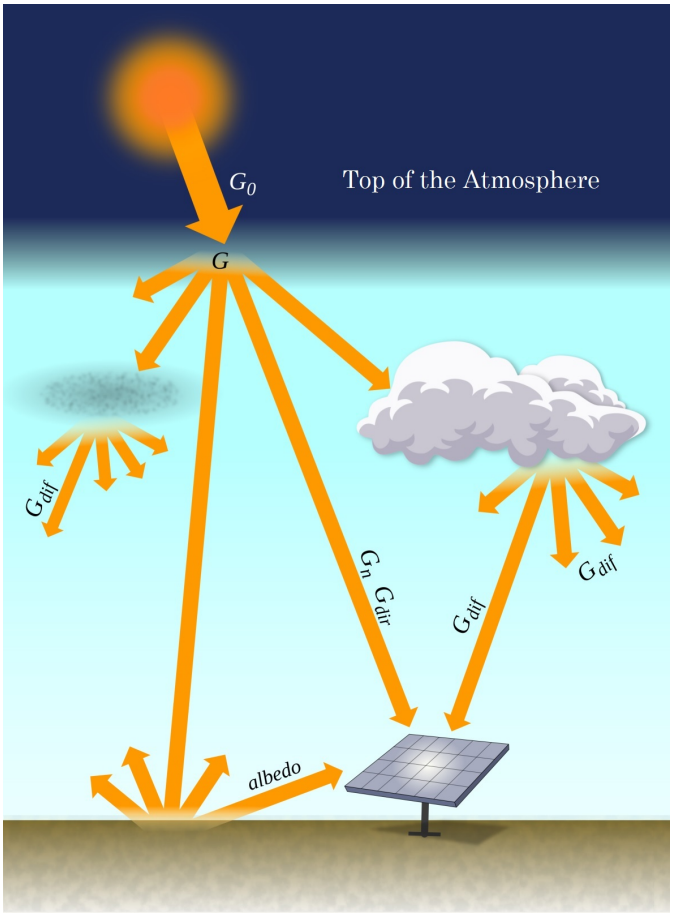

Source: Adapted from Pereira et al. (2017).

Finally, the scattered solar radiation reaching Earth's surface is called diffuse irradiance (G_d) and may be experienced as glare on overcast days. Its perpendicular projection over a horizontal surface is named as DHI. In contrast, the solar radiation reaching surface without changing its trajectory, the portion able to cast a shadow, is called direct or beam irradiance (G_b). Its perpendicular projection over a surface is called DNI, represented by G_n (DUFFIE; BECKMAN, 2013; BLANCO; SANTIGOSA, 2017). The following expressions denote the relationship among those components.

$$k_T = \frac{I}{I_0} \quad and \quad K_T = \frac{H}{H_0} \tag{2.3}$$

$$G = G_d + G_b = G_d + G_n \cos\theta_z \tag{2.4}$$

where θ_z or Φ is the solar zenith angle, the angle between the vertical and the line to sunrays trajectory, as displayed in Figure 2.2.

Figure 2.2 – Solar angles diagram

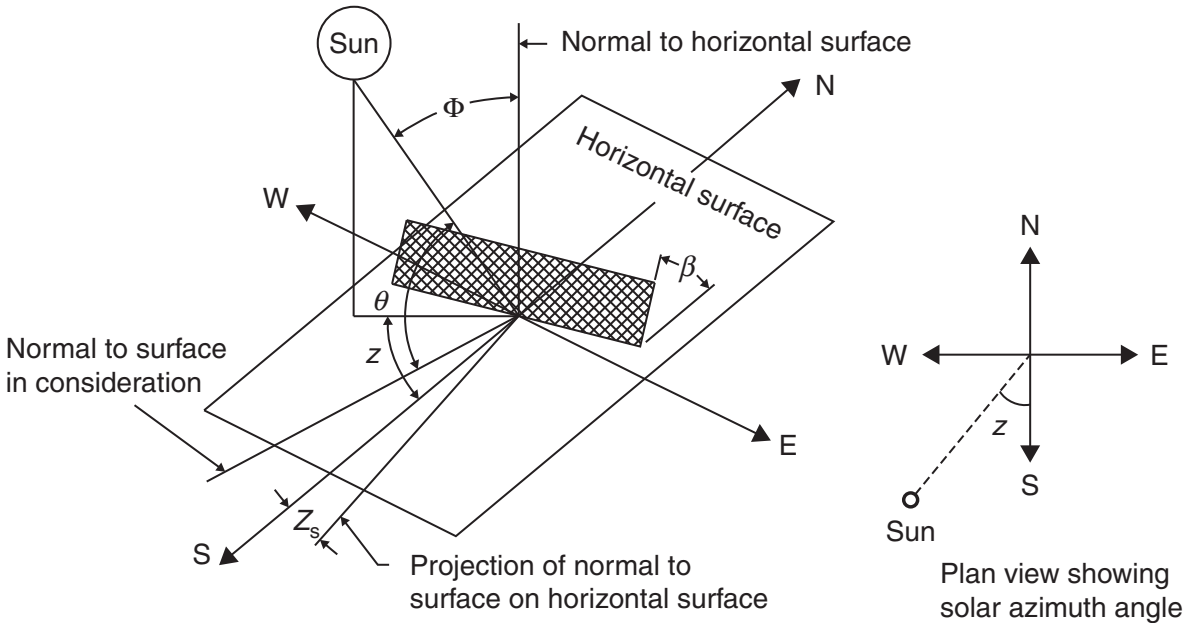

Source: Kalogirou (2014).
Note: β represents the surface tilt angle from horizontal, z_s or Γ is the surface azimuth angle, θ is the solar incidence angle, Φ or θ_z is the solar zenith angle, z or ψ is the solar azimuth angle. More details of their calculation are given by Duffie and Beckman (2013).

2.1.1 History of solar thermal energy

Since prehistory, the Sun has played a fundamental role on behalf of humankind, from providing the energy for drying and preserving food to evaporating seawater to salt yielding. Consequently, humans recognized the Sun as the power behind every natural phenomenon; on this account, many ancient tribes considered it a God (KALOGIROU, 2014).

Its first records date back to the Fertile Crescent, circa 2000 BCE, and describe the use of polished bowls by clergy members to light fires at religious practices (BUTTI; PERLIN, 1981). Later, other cultures would adopt this practice, such as Chinese, Greeks, and Romans. For example, the legend of the Archimedes (287-212 BCE) mirror, from around 212 BCE, states that Greek soldiers used multiple reflective surfaces (supposedly war shields) to converge sunlight onto Roman warships and set them on fire (see Figure 2.3) (KALOGIROU, 2014). The mathematician Diocles (240-180 BCE), also from Greece, described those optics notions around the same period (BUTTI; PERLIN, 1981).

The use of solar energy for architectural purposes was already known in the fifth century BCE by Socrates (470-399 BCE), who recorded techniques for controlling room temperature by orienting openings regarding the Sun's position. The Romans documented records of similar applications (BUTTI; PERLIN, 1981).

Al-Haitham (965-1040), an Egyptian mathematician, and important influence

Figure 2.3 – Archimedes and the Battle of Syracuse

Source: Cowen (1981).
Note: The Siege of Syracuse lasted from 214-212 BCE. It was fought as part of the Second Punic War, between Rome and Carthage.

on Renaissance intellectuals, condensed this ancient knowledge in his book, Opticae Thesaurus (BUTTI; PERLIN, 1981). Leonardo da Vinci (1452-1519) perfected concepts involving parabolic concentrators and aroused interest in their applications. He glimpsed an enormous concave mirror to be built in an excavated bowl-shaped in the ground. His notes suggest that a huge stationary mirror could be used as a source of heat to run commercial enterprises, not as a weapon of war (KRYZA, 2003). Comte de Buffon (1707-1788) described the development of heliostat designs in 1746 (BUTTI; PERLIN, 1981).

This subject gained significant momentum during the industrial revolution, impelled by concern on the long-term supply of coal, the primary fuel at the time (KRYZA, 2003). During the eighteenth century, solar furnaces capable of melting iron, copper, and other metals were constructed of polished iron, glass lenses, and mirrors. The furnaces were in use throughout Europe and the Middle East. One of its first large-scale applications was the solar furnace built around 1774 by Lavoisier (1793-1794), using large lenses to concentrate sunlight he attained remarkable temperatures, around 1750 ℃ (see Figure 2.4) (KALOGIROU, 2014).

Augustin Mouchot (1825-1912) was one of the pioneers in converting solar radiation into mechanical energy. He built a solar machine, presented at the 1878 Universal Exposition, using a solar-driven steam engine for the first time. Mouchot's concentrator included a layer of glass to intensify heating (see Figure 2.5). The boiler concept has underlain the design of modern rooftop water heaters (KRYZA, 2003).

A more recent landmark is Frank Schuman's (1862-1918) successful parabolic

trough-driven pumping system in Egypt in 1913. With an area of around 1020 m^2, it delivered approximately 55 horsepower (41 kW) (LOVEGROVE; STEIN, 2020).

Figure 2.4 – Solar furnace used by Lavoisier in 1774

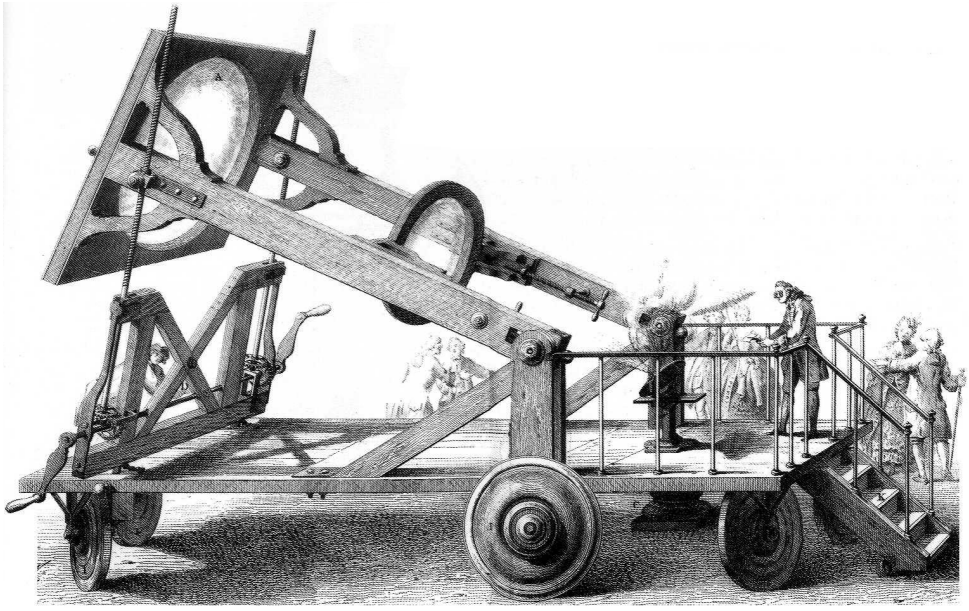

Source: Kalogirou (2004).

Figure 2.5 – Augustin Mouchot's sun machine

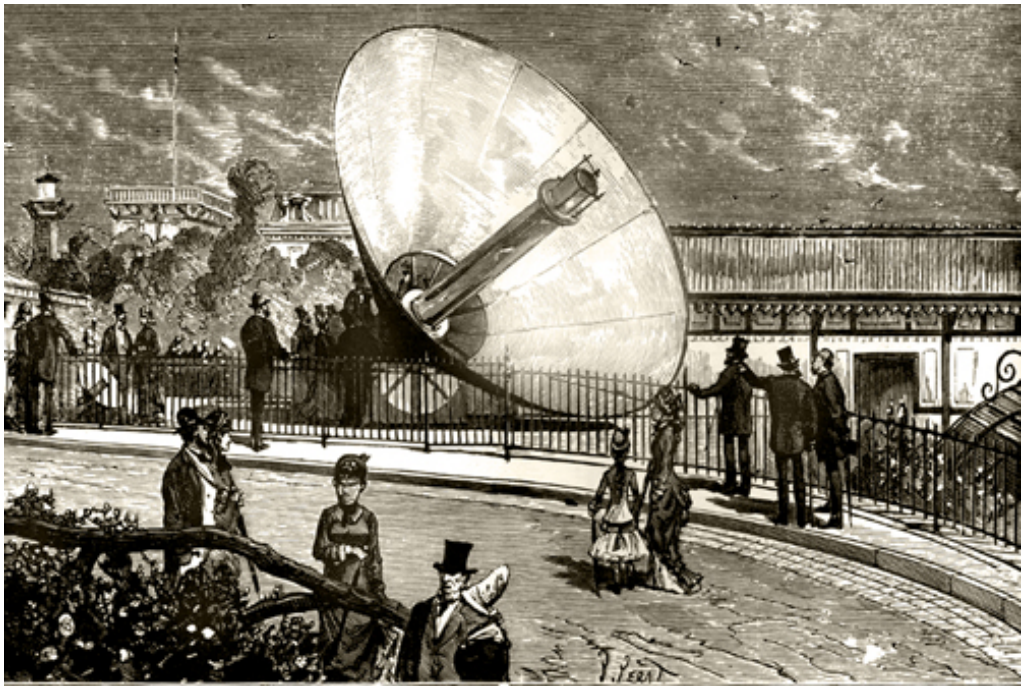

Source: Butti and Perlin (1981).
Note: The machine was displayed at the Universal Exposition, in Paris, 1878.

Figure 2.6 – Concentrated solar power development from 1982 to 2030

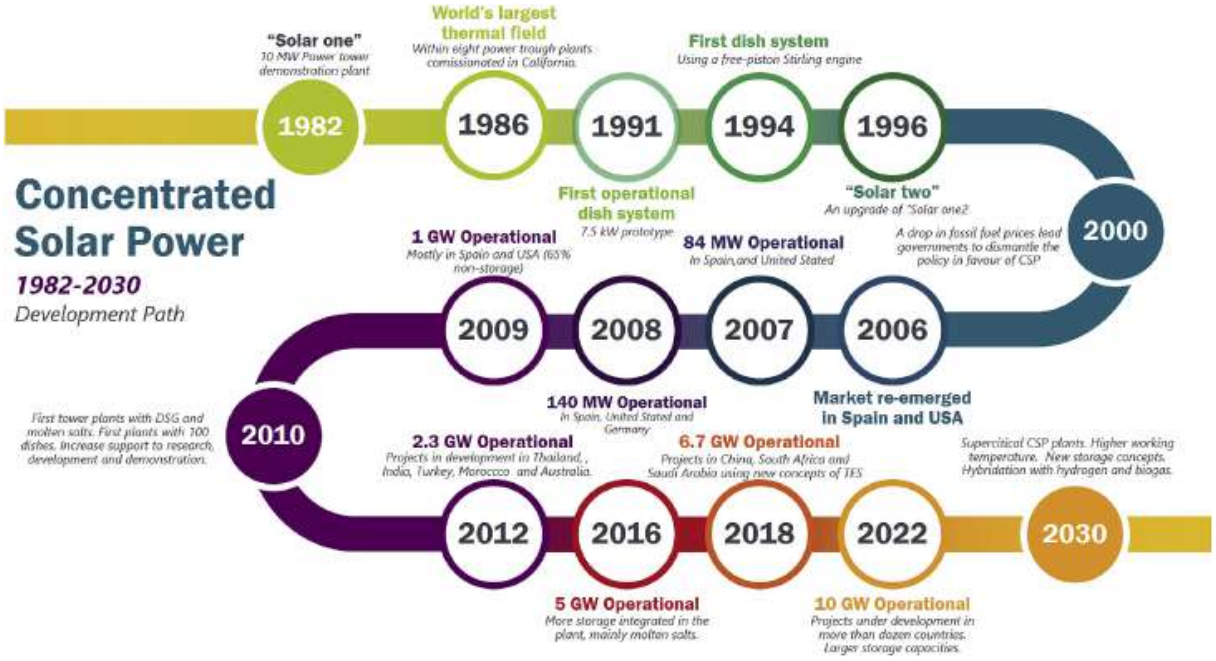

Source: Adapted from Palacios et al. (2020).

Experiments and small-scale CSP prototypes were developed throughout the whole twentieth century. Numerous pilot plants have been built and operated, including a 5 MW_e plant in Russia, a 2.5 MW_e plant in France, and 1 MW_e plants in Japan, Italy, Spain, and the USA (DUFFIE; BECKMAN, 2013). However, the birth of modern CSP as a commercial industry occurred in California in the 1980s. Favorable government policies led to the commission of Solar One in 1982, the first large-scale demonstration project. It achieved a 10 MW_e net capacity using SPTs with water-steam as the HTF and an oil-rock thermocline TES, which presented several problems in terms of storage and continuous turbine operation. Important outcomes proved that SPT could work efficiently to produce utility-scale power from sunlight, and the storage system was inadequate to operate the turbine at peak efficiency (PALACIOS et al., 2020).

Solar One ceased operation in 1988 and was rebuilt and restarted in 1996 as Solar Two. The primary modification was replacing the TES with a I2T storage system with a capacity of three hours, using molten salt both as HTF and HSM. A one-time operation illustrated the new design's success for 154 continuous hours (DUFFIE; BECKMAN, 2013). This installation was operated until 1999, demonstrating that solar thermal energy could be efficiently and cost-effectively stored, opening the way to a later TES deployment (PALACIOS et al., 2020).

Another important initiative was the SEGS project started in 1984, consisting of nine synthetic oil-based PTC plants in Southern California, totaling 354 MW_e. These plants are based on PTC to provide steam to Rankine power cycles (PALACIOS et al.,

2020). Duffie and Beckman (2013) provides further details about those facilities.

Most CSP facilities today replicate the design of those Californian plants, most of which are still operating for more than 30 years and have established the technology as commercially proven. Over the mid-1980s and mid-1990s (LOVEGROVE; STEIN, 2020). This market kept expanding until 2000, when a slump in fossil fuel prices diverted the attention from renewables, leading policymakers to temporarily dismantle pro-CSP incentives. Consequently, no further commercial deployment happened until 2005, although in that period took place considerable research, development, and demonstration (PALACIOS et al., 2020).

Strongly related to this theme, the term "greenhouse effect" concerning the atmosphere was first used in 1901 by Nils Ekholm (1848-1923). Nevertheless, its central concept was firstly proposed by Joseph Fourier (1768-1830) in 1824. This argument was further strengthened by Claude Pouillet (1790-1868) in 1838. Eunice Foote (1819-1888) and John Tyndall (1820-1893), in 1856 and 1859 respectively, were the first to measure the infrared absorption and emission of various gases and vapors, noticing the Earth's surface average temperature (about 15 ℃) is maintained due to the absorption of infrared by atmospheric components. As a result, the heat emitted from Earth's surface gets trapped as they prevent it from being lost in space. They observed that this effect is occurs mainly due to water vapor and hydrocarbons, and carbon dioxide had a significant effect. Svante Arrhenius (1859-1927) more fully quantified this effect in 1896, being the first to predict that doubling the atmospheric concentration of carbon dioxide would lead to a temperature rise of five degrees Celsius (BEHERA, 2020).

Despite that, just more than hundred of year later, concern over human-induced climate change has emerged to dominate the political agenda around energy supply. As a consequence, the CSP market re-emerged, especially in the USA and Spain. It was driven partly by the recognition of this technology which enables quick and significant cuts in greenhouse gases (GHGs) emission (PALACIOS et al., 2020).

The COP21, held in France, negotiated the Paris Agreement, a global agreement on climate change mitigation. The 196 attending countries agreed to reduce GHG emissions, aiming to limit the rise in the global average temperature to two degrees Celsius above pre-industrial levels. As part of this agreement, many countries pledged to reach net-zero in the next few decades. For example, China has promised to invest 360 billion USD in renewable energy by 2020 and by 2030 increase its solar power production up to 10% of its electricity mix. Moreover, other countries such as India, Chile, South Africa, UAE, and Morocco are promoting important CSP investments, supported by many organizations, such as the World Bank, the Desertec Foundation, and the German Federal Enterprise for International Cooperation (GIZ). These countries hold roughly 98.6% of the world's current CSP installed capacity (ACHKARI; FADAR, 2020), as illustrated in Figure 2.7.

The year 2010 marked a turning point for CSP, the global installed capacity reached 1 GW_e, with the technology spread all over the globe: Spain, China, India, USA, and Morocco, among many others, commissioned new plants. Spain constructed 2.3 GW_e in capacity between 2009 and 2014, via a FIT regime. Almost half the country's new capacity has been equipped with TES, most of them using a I2T molten salt-based configuration. The rules of this scheme limit plant size to 50 MW_e each. While these rules artificially held plant size back, they did encourage the uptake of TES, which is now recognized as CSP 's greatest strength (PALACIOS et al., 2020).

Since then, the CSP installation has soared, with new solar field configurations, such as DSG and DMS, increasing the global capacity to more than 5 GW_e in 2016, with increasingly more integrated storage capacity (PALACIOS et al., 2020). Figure 2.6 summarizes the most important milestones in CSP development from the 1980s to expected achievements for the upcoming years.

Figure 2.7 – Evolution of the CSP capacity between 2010 and 2020

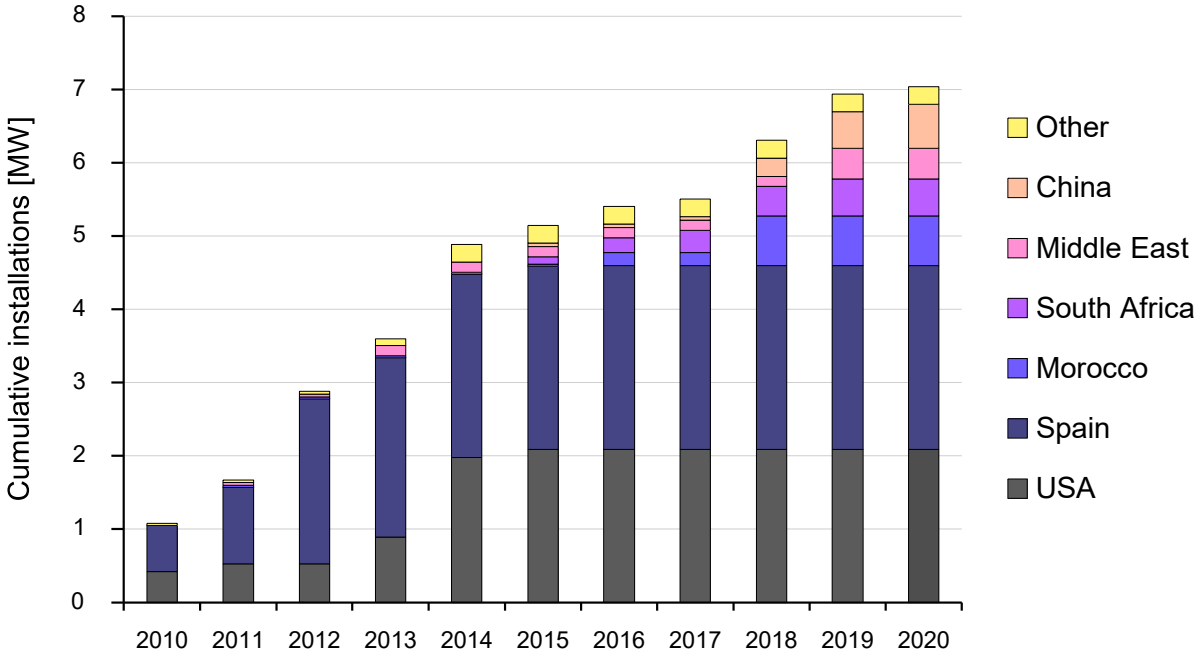

Source: Adapted from Feldman et al. (2021).

In 2020 TES for CSP reached 21.1 GWh, growing ten times in the preceding decade REN21 (2021). In that year, 10 GW_e were expected to be operational. However, recent data indicate this goal has not been achieved, in early 2021 reaching 7.0 GW_e accordingly to Feldman et al. (2021) and 6.4 GW_e according to the SolarPACES database (SOLARPACES, 2021) (see 2.7). The SolarPACES program, hosted by the NREL, is the umbrella under which the CSP community has worked together and shared information for many years. According to the SolarPACES database, there are currently 112 opera-

tional CSP projects around the world and 61 more under construction and development stages. Figures 2.8 and 2.9 summarizes the CSP projects worldwide distribution and the status. It should be mentioned that, historically, only a third of those announced enterprises have achieved operation.

Figure 2.8 – Status of CSP projects in the world in 2020

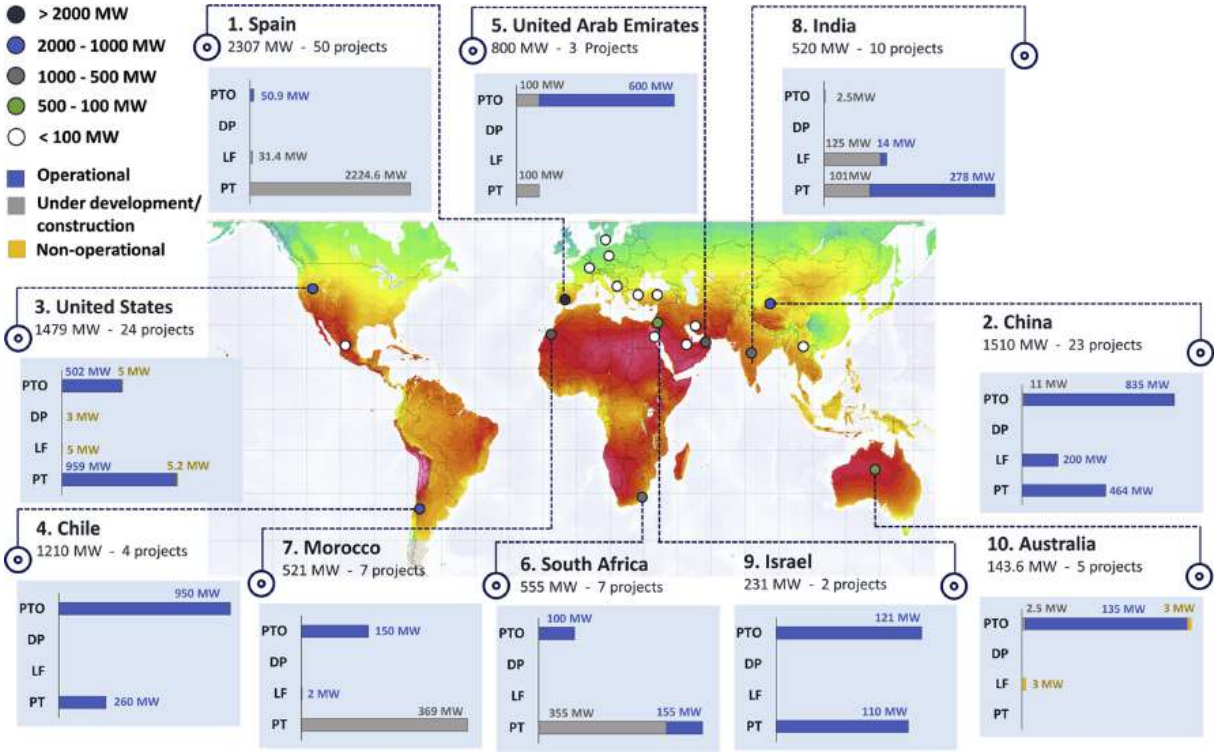

Source: Adapted from Palacios et al. (2020).
Note: The background map shows the direct normal irradiation over the globe (see Figure 2.12).

The current CSP capacity roughly represents 1% the wind (743 GW) and solar PV (501 GW) capacity of REN21 (2021). However, this is about the same level as PV in 2006 (REN21, 2018).

Currently, CSP operates with an average CF of 45.2% produces electricity with a LCOE with an average of 10.8 ¢USD kWh^{-1}, 68% lower than in the preceding decade IRENA (2017). In annual energy production terms, CSP's relative position is robust due to those higher CFs achieved with the addition of storage. The use of proven and low-cost TES now marks CSP as a technology of high potential as the world continues to move towards a renewable-driven future.

As future trends, new storage concepts and hybridized configurations present significant potential. In addition, due to supercritical fluids and new materials, higher operating temperatures are expected by 2030 (PALACIOS et al., 2020). A continuing challenge for CSP is its dependence on the economies of scale afforded by large steam

Figure 2.9 – Concentrated solar power projects by region and technology

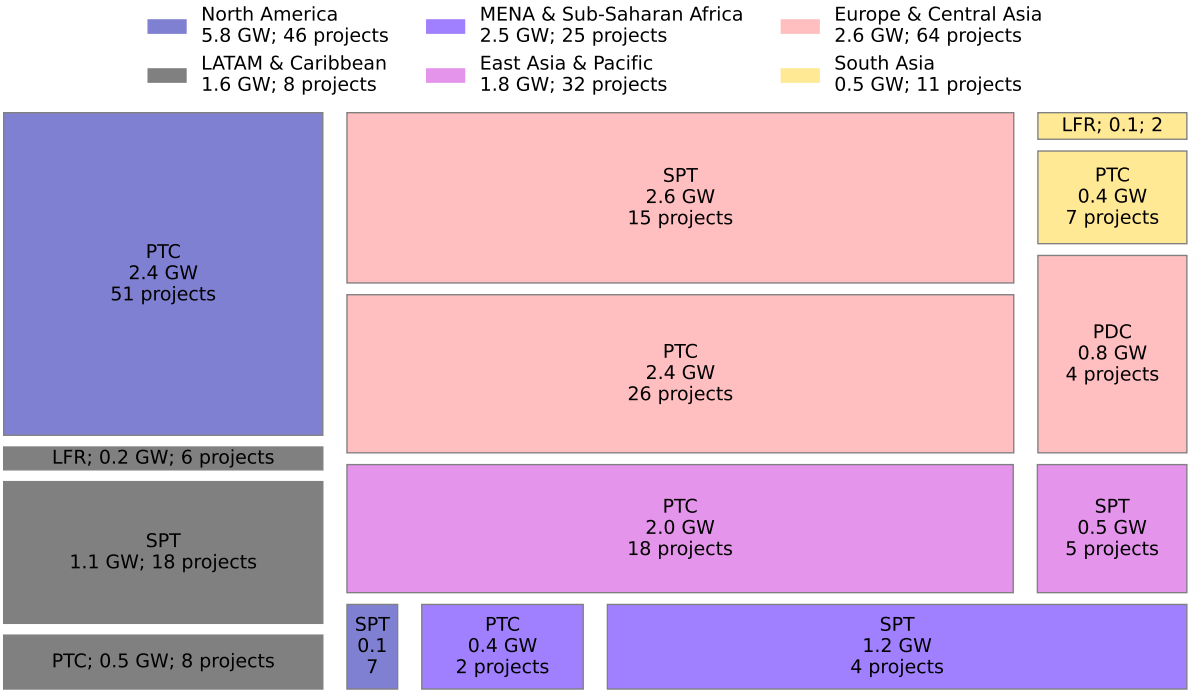

Source: Elaborated using Matplotlib (HUNTER, 2007) with data from SolarPACES (2021).
Note: The locations were categorized according to World Bank (2020). The rectangles are proportional to the plants capacity. The sum of the presented data may not correspond with the totals, once small-scale plants were not considered. Decommissioned, operational, under operation and construction projects are considered.

turbines, leading to significant capital risk. However, now that the size of new renewable projects has grown, there is more support for such investments. Table 2.1 summarizes the up-to-date CSP situation and expectations for the next decades.

2.2 INTRODUCTION TO CONCENTRATED SOLAR POWER

As previously mentioned, CSP technologies capture the radiation emitted by the Sun to drive a thermoelectric power cycle. The solar energy is focused onto a receiver, where a HTF is heated and used to drive a heat engine – i.e., a steam or gas turbine connected to an electrical power generator (as is shown in the schemes of Figures 2.10 and 2.11). Different from flat-plate collectors and PV modules, capable of absorbing both the direct and diffuse components of solar radiation, concentrating modules require well-oriented sunrays (i.e., the direct component). For that, they demand highly reflective and clean mirrors, sun-tracking mechanisms, and more complex support structures than for PV and flat plate collectors (HELLER, 2017).

In addition, fossil and renewable fuels such as oil, natural gas, coal, and biomass can be used for backup energy in these plants. The flexibility of heat storage combined with backup fuel operation enables the plants to provide both baseload power and peak

Table 2.1 – Overview of the current and expected characteristics of solar thermal plants

Characteristic	**Current state**	**Future trends**
Purpose of plant	– 69% commercial – 18% R&D – 13% demonstration	– Increased share of commercial – No plant specifically for R&D
Technology	– SPT and PTC are the most used – PDC is hardly used	– Prevalency of SPT – Increased proportion of PDC
Average plant capacity	– 33 M_e	– Increased to 126 MW_e
Hybridization	– Significant presence (77%)	– Reduced presence
Storage system	– Used in 47% of plants	– Increased beyond 70%
Average storage capacity	– 3 h (built before 2010) – 7 h (built after 2010)	– Increased to 7.65 h
Storage technology	– Vast majority of STES	– Vast majority of sensible storage

Source: Pelay et al. (2017).

power, which can be designed to mitigate the effects of the duck curve [(6)] on the grid or cover HVAC loads, usually occurring around midday (JONES-ALBERTUS, 2017).

These characteristics hold a distinguished potential for hybridization and, most importantly, for energy storage integration. For example, the use of TES systems allows CSP to operate during cloudy weather and nighttime. For this purpose, concrete, molten salts, ceramics, or PCMs can be used, being it currently much cheaper than storing electricity in chemical batteries, in contrast to most modern renewables, that generally present difficulties in scalability and rely on high environmental cost materials and processes (KALOGIROU, 2004; AKINYELE; RAYUDU, 2014; IRENA, 2017).

According to Turchi (2010) and Heller (2017), this kind of facility can be divided into four major blocks: SF, TES, BUS, PB (see Figures 2.10 and 2.11), being mainly composed of:

- *Solar field*. It includes a support structure, mirrors, receivers, control, and HTF pumping systems, valves, and freeze protection;
- *Thermal energy storage*. Its primary equipment includes an insulated tank(s) or alternative storage devices, HSM, heat exchangers, pumps, valves, and piping;
- *Backup system*. It is comprised of components usually found in conventional thermoelectric facilities, such as boilers and heat exchangers. It can be used

(6) The duck curve – named after it resembles a duck – is a snapshot of the grid energy demand over a typical spring day in California, when this effect is most extreme. It shows the difference in electricity demand and the amount of available solar energy throughout the day. When the Sun is shining, solar energy is abundant and floods the market. Then, in the evening, it quickly drops off as electricity demand peaks.

for plant startup, anti-freeze purposes, combined cycles, or hybridization with biomass or fossil fuels. It may reduce the overall LCOE, as deeply explored by Starke (2019);

- *Power block*. Heat exchangers (traditional shell and tube) steam turbine, feedwater pump, and preheaters, deaerator, economizer, evaporator, superheater, condenser, cooling tower, and BOP [7]. It is coupled to the electric circuit, composed of the generator, transformers, circuit breakers, switches, and transmission lines.

Figure 2.10 – Scheme of a conventional concentrated solar power system

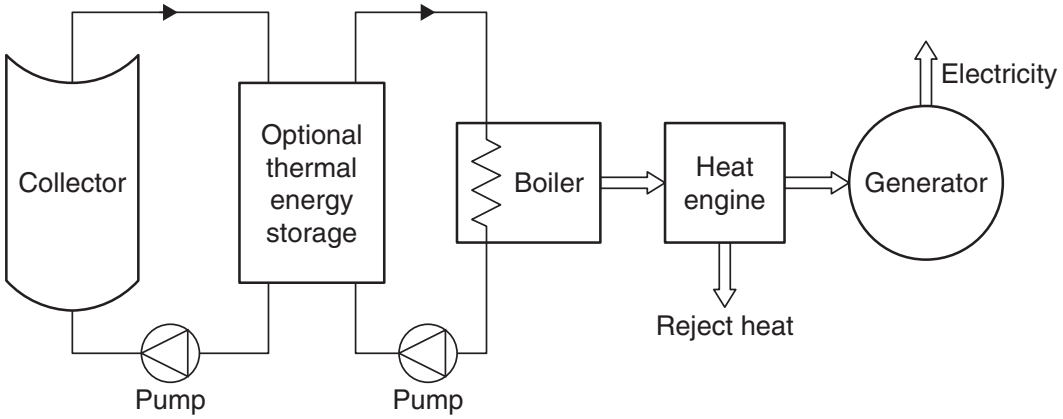

Source: Kalogirou (2014).
Note: A BUS system can also incorporate the plant, being integrated similarly to the TES. Both BUS and TES are optional.

Ideally, all components need to be as efficient as possible and simultaneously of high durability and low cost. According to Heller (2017), the performance of a CSP plant depends mainly on: solar tracking precision; mirrors' reflectance and geometrical precision; receivers' absorptance and emittance; heat storage efficiency; heat transfer to the power cycle efficiency; power cycle efficiency; components durability; and low maintenance efforts.

Because of the large area required by CSP, mainly by the reflective surfaces at the solar field, these plants are usually allocated on non-fertile lands, such as deserts, which for the most part also have abundant solar radiation. For example, according to Geyer and Quaschning (2000), if less than 1% of the Sahara Desert (an area of about 65,000 km^2) were covered by CSP plants, its electricity output would be equivalent to world consumption in 2000. Moreover, according to (Wolff et al., 2008), 20% of this area could attend to the European Union's current electricity demand. Similar studies

[7] Systems supporting the main thermal processes are called the balance of plant. They include, but are not limited to: auxiliary cooling, auxiliary steam, blowdown, drains and fuel, compressed air and water circuit, storage, treatment, and reposition.

Figure 2.11 – Basic energy flow diagram for concentrated solar power system

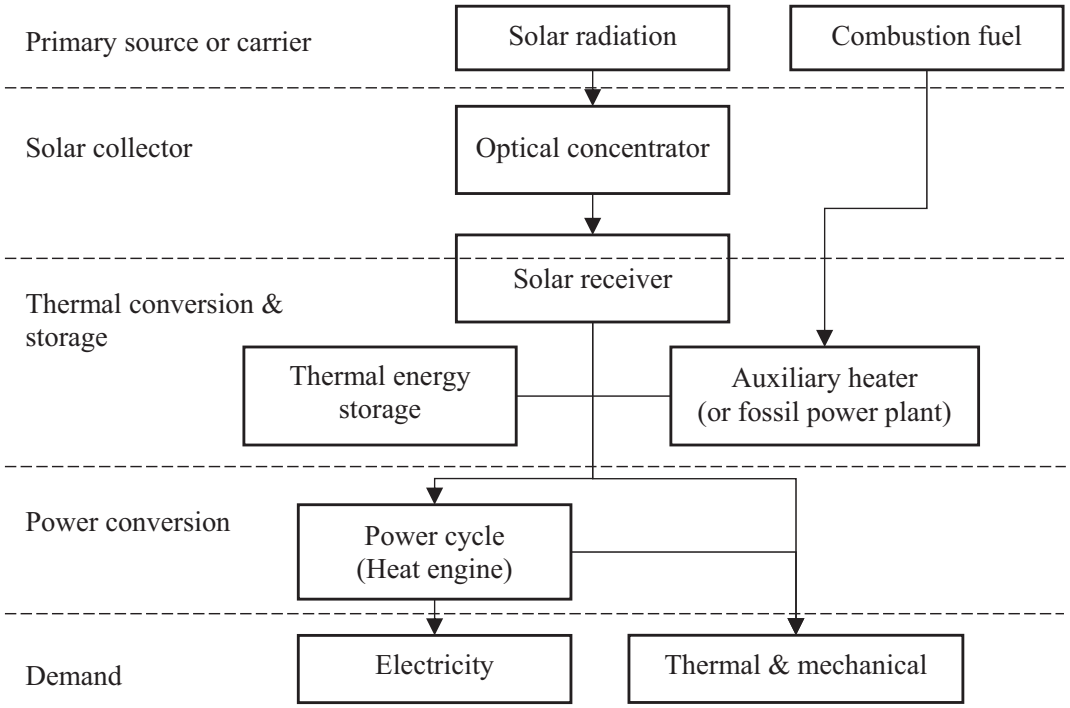

Source: Gauché et al. (2017).

predict the solar resource in Southwestern USA could produce about 7 TW (7000 GW) with CSP, which is roughly seven times its current generation capacity.

Figure 2.12 shows the DNI distribution around the world. Notably, the most favorable areas for this technology are in Australia, Chile, Mexico, Peru, Southwestern USA, Southern Africa, MENA, Western China, and Northwestern India. Other areas that may be suitable include central Asia, Northern Argentina, Northeastern Brazil, and Southern Europe. Additionally, Table 2.2 shows the direct normal irradiation threshold for economic viability assessed for multiple locations.

2.2.1 Concentrated solar power technologies

Six system architectures have been developed for CSP: PTCs, LFRs, SPTs, and PDCs, solar ponds and the SUTs. Among those, the first four enable higher temperature obtainment and consequently are the most studied and deployed for this kind of application. They are commonly classified accordingly to their concentration and receiver types (see Table 2.3). The overall plant efficiency grows when point focus, mobile receivers, or both are employed.

Regarding their concentration type, PTC and LFR perform linear focus. They concentrate sunlight on a linear receiver, and because of that, have a relatively lower concentration ratio, between 25 and 100 suns [(8)]. In contrast, SPT and PDC undertake

[(8)] It is the unit used to express the concentration ratio of solar collectors (i.e., a collector with ten suns achieves ten times the power density of natural sunlight).

Figure 2.12 – World daily direct normal irradiation distribution

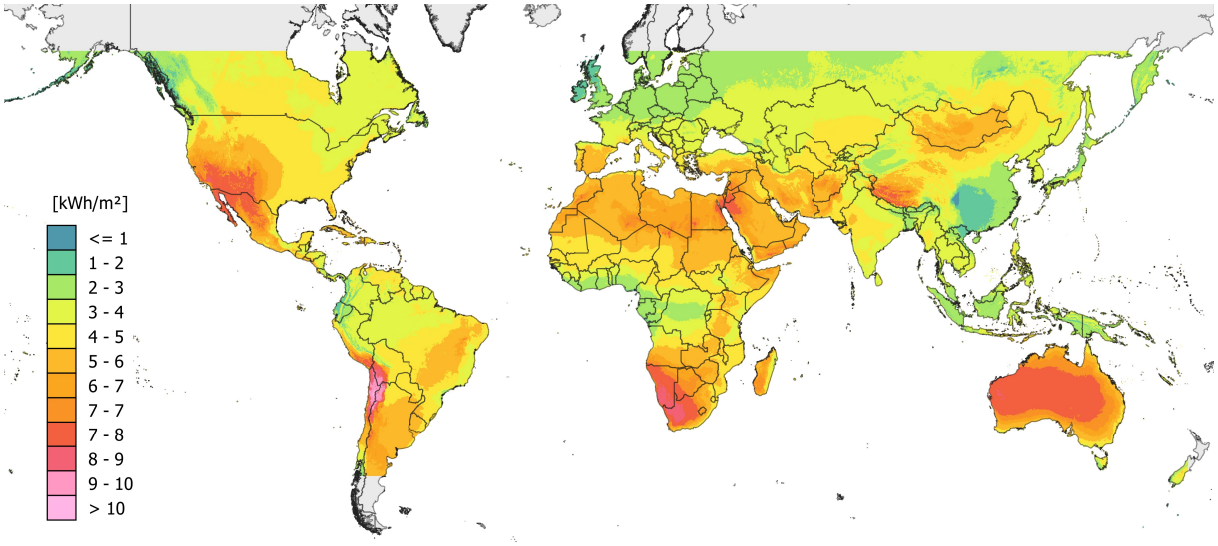

Source: Elaborated using QGIS (QGIS DEVELOPMENT TEAM, 2009) with data from Solargis (2019).
Note: 5.48 kWh m^{-2} day^{-1} corresponds to 2000 kWh m^{-2} yr^{-1}. The gray areas are not included at the Solargis database. Yet, they correspond to high latitude locations, with far less potential for solar energy harnessing.

Table 2.2 – Desired direct normal irradiation threshold for key locations

Country	**Annual irradiation$^{\oplus}$ [kWh m^{-2}]**	**Reference**
Australia	2,564	Hinkley et al. (2013)
Egypt	2,496	Blanco et al. (2013)
Jordan	2,400	Al-Soud and Hrayshat (2009)
Qatar	2,200	Weber (2013)
Chile	2,190	Corral et al. (2012)
India	2,100	Jain et al. (2013)
South Africa	2,100	Fluri (2009)
Any$^{\ominus}$	2,000	IRENA (2012)
Cyprus	2,000	Poullikkas (2009)
Algeria	1,800	Boukelia and Mecibah (2013)
Turkey	1,800	Kaygusuz (2011)
Serbia	1,400	Pavlovic et al. (2012)

Source: Krarti (2018).
Note: $^{\oplus}$Annual direct normal irradiation; $^{\ominus}$A general value for achieving attractive LCOEs.

punctual focus, achieving far higher concentration ratios, in the range of 300 to 3000 suns (see Table 2.4 and Figure 2.13). Additionally, LFR and SPT present a fixed receiver, while PTC and PDC have mobile ones, contributing to better sun tracking and optical losses reduction. The two and single-axis solar position tracking strategies are presented in Figure 2.15.

Based on SolarPACES (2021), from the 113 plants currently operational (see Figure 2.14), PTC represents the greatest share, 84, whereas SPT accounts for 22, and LFR for seven. Concerning the PDC, it is not applied in presently functional in-

Table 2.3 – Main CSP technologies arranged by their concentration and receiver type

Receiver type	**Linear focus** Single axis sun tracking	**Point focus** Dual axis sun tracking
Fixed receiver Stationary receivers, that facilitate the HTF transport	*LFR* 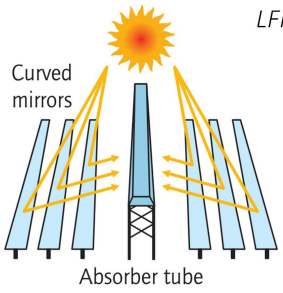 	*SPT* 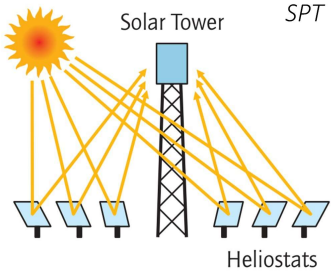
Mobile receiver The concentrators and receivers move as a group, what increases the optic efficiency	*PTC* 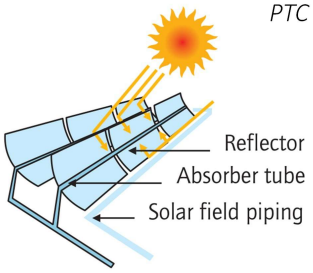 	*PDC* 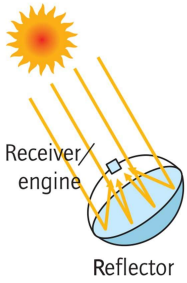

Source: Adapted from IEA (2014) and Starke (2019).

Figure 2.13 – Absorber efficiency due to concentration and absorber temperature

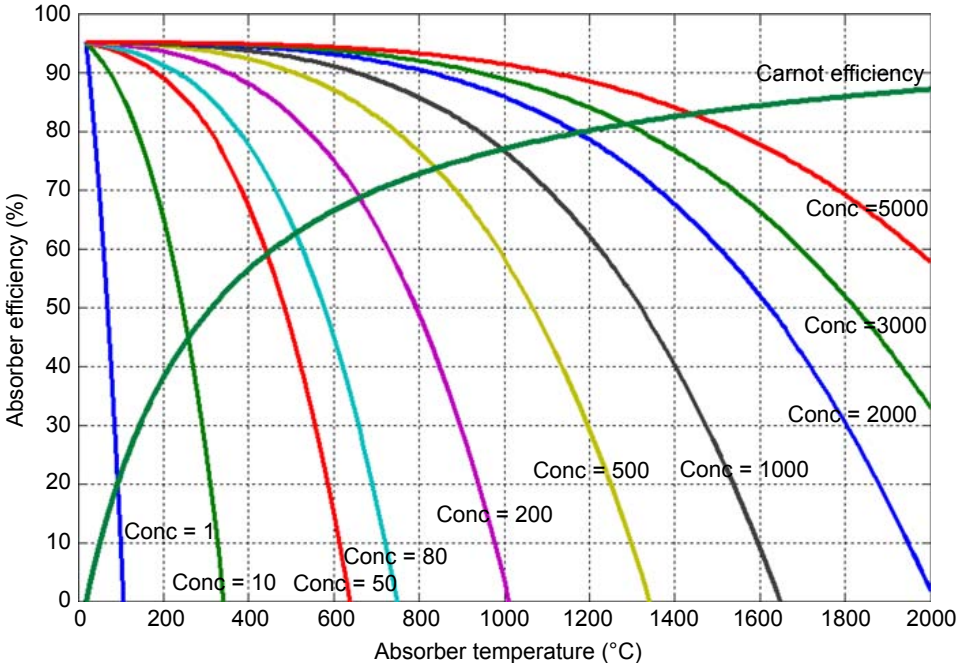

Source: Blanco and Santigosa (2017).
Note: Concentration ratio given in suns. Based on a ambient temperature of 20 ℃, a DNI of 770 W m^{-2}, and absorptance and emittance of 0.95.

stallations. Due to the Stirling cycle, it is recommended for lower generation capacity, between 0.01 and 0.4 MW; because of that, it has received little attention in the last few years. Moreover, from the 55 plants under construction and development, 22 have

Table 2.4 – Features of the main concentrating collector technologies

Parameter	**PTC**	**SPT**	**LFR**	**PDC**	**Unit**
Maturity	High	Medium	Medium	Low	–
TRL$^{\oplus}$	9	7-8	7-8	6	–
Operating temperature	290-395	290-565	250-395	550-750	℃
Concentration ratio	70-80	300-1000	25-100	1000-3000	suns
Capacity range	10-200	10-200	10-200	0.01-0.4	MW
Capacity factor	20-25$^{\ominus}$ 40-53$^{\otimes}$	40-53$^{\ominus}$ 65-80$^{\otimes}$	22-24$^{\ominus}$	25$^{\ominus}$	%
Power cycle efficiency	37.7	41.6	–	–	%
Cooling method	Wet	Wet, dry	Dry	Dry	–
Suitable for air cooling	Low to good	Good	Good	Best	–
Land use	0.025	0.036	0.008	0.011	km^2 MW^{-1}
Water requirement	3 (wet)	1.8-3 (wet)	3-3.8 (wet)	0.05-0.1	m^3 MWh^{-1}
Capital cost	3900-4100$^{\ominus}$ 6300-8300$^{\otimes}$	5700-6400$^{\ominus}$ 8100-9000$^{\otimes}$	–	–	USD kW^{-1}
O&M cost	0.012-0.02	0.034	–	0.21	USD kWh^{-1}
LCOE	0.26-0.37$^{\ominus}$ 0.22-0.34$^{\otimes}$	0.2-0.29$^{\ominus}$ 0.17-0.24$^{\otimes}$	0.19-0.38$^{\ominus}$ 0.17-0.37$^{\otimes}$	–	USD kWh^{-1}

Source: Data from Chaanaoui et al. (2016), Liu et al. (2016) and Achkari and Fadar (2020).
Note: $^{\oplus}$The TRL is a measure of estimating technology maturity, more details are given by Straub (2015); $^{\ominus}$No storage for PTC, LFR and PDC. 6-7.5 h TES for SPT; $^{\otimes}$6 h TES for PTC and LFR. 12-15 h TES for SPT.

been chosen as PTC, 24 as SPT, six as LFR, and three as PDC (see Figure 2.14).

The recent growth in SPT is mainly driven by its higher optical efficiency and ability to achieve higher temperatures than linear concentration technologies, reducing the specific investments involved in larger fields and TESs. In contradiction, SPTs required significant spacing between heliostats, which grows as the solar field capacity. Because of that, SPT has a lower energy density than the PTC. As the plant capacity increases, more spacing is necessary between heliostats requiring approximately five times the reflective surface area, or 0.036 km^2 MW^{-1}, 44%, 350% and 227% superior to PTC, LFR, and PDC, respectively (see Table 2.4). Consequently, linear concentration is advantageous for large plant capacities of hundreds of megawatts.

Among those enterprises, the world's largest CSP facility, the Mohammed bin Rashid Al Maktoum Solar Park, with 950 MW (600 MW PTC, 100 MW SPT, and 200 MW PV), is currently under construction in the UAE, and will be operational in 2021 (SOLARPACES, 2021). That title is currently given to the Noor Ouarzazate Solar Complex in Morroco, with a 580 MW capacity – NOOR-I (160 MW PTC), NOOR-II (200 MW PTC), NOOR-III (150 MW SPT) and NOOR-III (70 MW PV) – fully operational since 2018 (PALACIOS et al., 2020). Another highlight is the Cerro Dominador project in María Elena, Chile. The plant was inaugurated in 2021 with a nominal capacity of 210 MW (110 CSP and 100 PV) and is the first of its kind in Latin America.

Figure 2.14 – Overview of CSP projects by technology and status

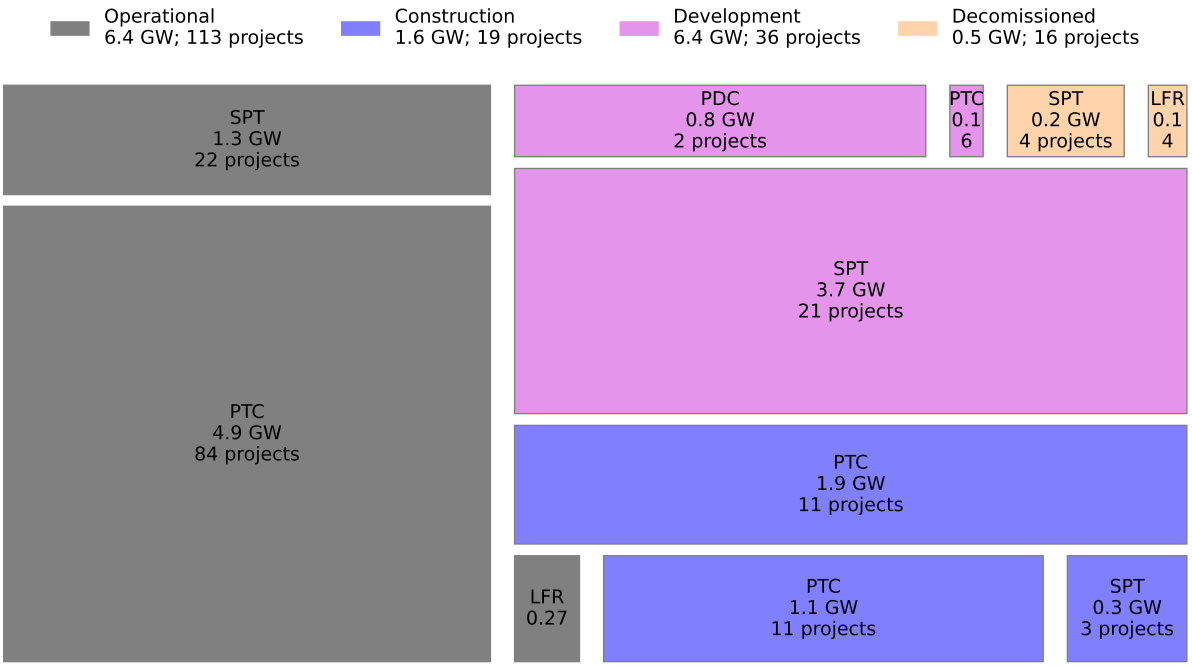

Source: Elaborated using Matplotlib (HUNTER, 2007) with data from SolarPACES (2021).
Note: The rectangles are proportional to the plants total capacity. The sum of the presented data may not correspond with the totals, once small plants were not considered. Considering decommissioned, operational, under operation and construction projects , the four technologies account for 184 projects and 14.8 GW.

2.2.1.1 Parabolic trough collectors

Currently, PTC is the most proven CSP technology, mainly due to the expertise obtained after more than two decades of operation in California. Indeed, this technology currently has the most significant commercial operating experience worldwide. Consequently, it has the highest maturity and the lowest technical and financial risks.

PTCs consists of a solar field technology that uses parabolic-shaped reflective troughs to concentrate solar irradiation onto a receiver tube positioned at their focal line, aiming to warm up an HTF. The PTC was the first solar thermal technology to achieve commercial operation in the 1980s.

At the conventional CSP-PTC design, synthetic oil is conducted through the receptor tubes, in which they achieve up to 395 ℃. High-temperature and high-pressure steam is generated via heat exchange systems and used to drive the steam turbine, and alternatively taken advantage of by medium-temperature industrial processes. Specific problems with the PTC are the relatively low concentration (around 70-80 suns, asymmetrical absorber tube heating, and restrained system efficiency (WANG, 2019).

This technology uses a single-axis tracking system revolving around the concentrator tube axis to follow the Sun's movement. The cross-section of the reflective surface corresponds to a parabola shape, specially designed to converge the parallel sun rays. Thus, DNI is constantly concentrated on the surface of the receiver tubes enabling

Figure 2.15 – Solar tracking strategies

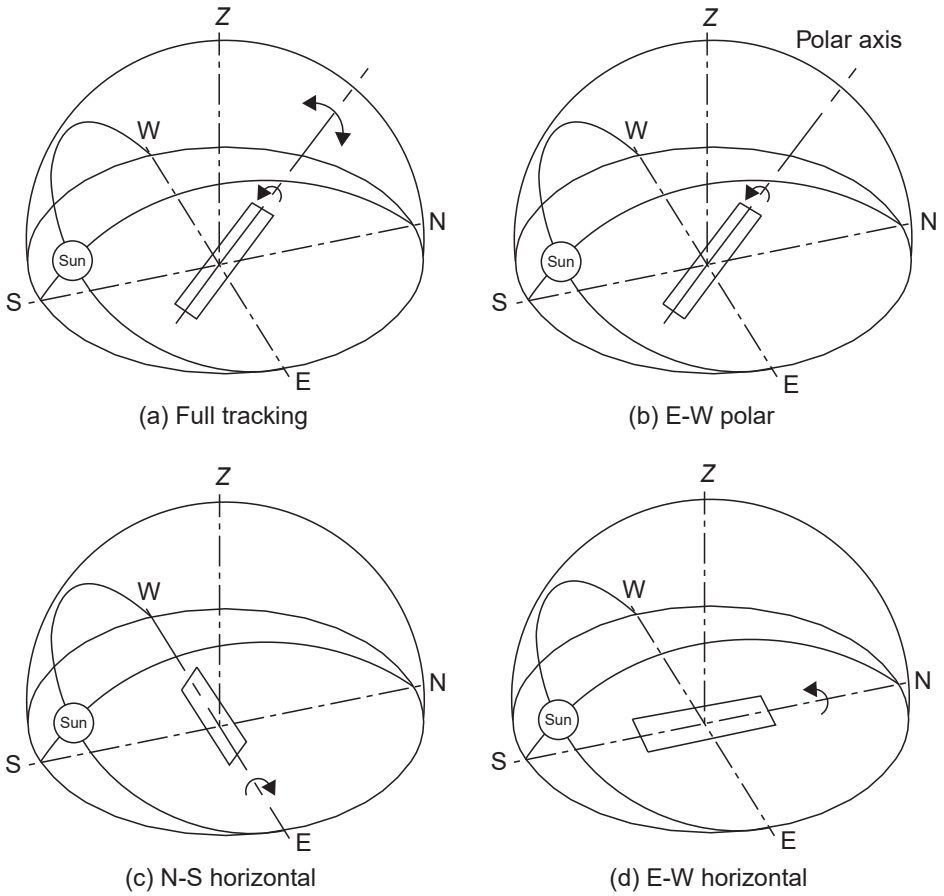

Source: Kalogirou (2014).
Note: The solar position tracking can be performed in two axes – (a) full tracking – or in only one axis – parallel to: (b) the polar axis; (c) east-west axis; (d) north-south axis.

HTF heating. The EuroTrough collectors are among the most popular PTC designs. In that structure, the parabola at the cross-section is only formed by two distinct mirror shapes (i.e., one for the inner and one for the outer parabola. As such, four mirror facets compose the whole parabola due to symmetry. According to Geyer (2002), systems equipped with the EuroTrough ET150 can provide power stations up to 200 MW_e.

For the performance assessment of SCAs, reflectance and shape precision are the main parameters of concern. Therefore, it is crucial to analyze mirrors both in ideal and in loco conditions (HELLER, 2017).

A PTCs solar field mainly consists of the following components: base, bracket, mirror, power machine, transmission, and control systems. A typical solar field comprises multiple units, called SCA, connected in series along the absorber tube axis and equipped with power, transmission, and control systems. Generally, for lower DNIs, hydraulic or mechanical transmission can be applied, whereas only hydraulic transmissions can be applied for one with intense radiation areas.

A bracket is connected to the mirror through fixtures to support and ensure the

stability of the parabola shape. There are three types of structure: torque tube, torque box, and space truss types. The materials used are usually steel, or aluminum alloys, assembled mainly by welding and punching (WANG, 2019).

Recently, a new PTC model has been developed, called Ultimate Trough. Its first commercial application is in an Integrated Solar Combined Cycle (ISCC) power plant in Dubai, Saudi Arabia. It is estimated that an equivalent-sized Ultimate Trough solar field could be 20-25% cheaper than a EuroTrough (Schweitzer et al. 2014). Comparing NREL's installed cost to a published estimate by the developer, there is a good similarity between the two estimates. For example, NREL estimated that for an SF of 68 loops, the installed cost (excluding licensing costs) was approximately 178 USD m^{-2} (TURCHI et al., 2019).

Figure 2.16 – EuroTrough ET150 solar collector assembly

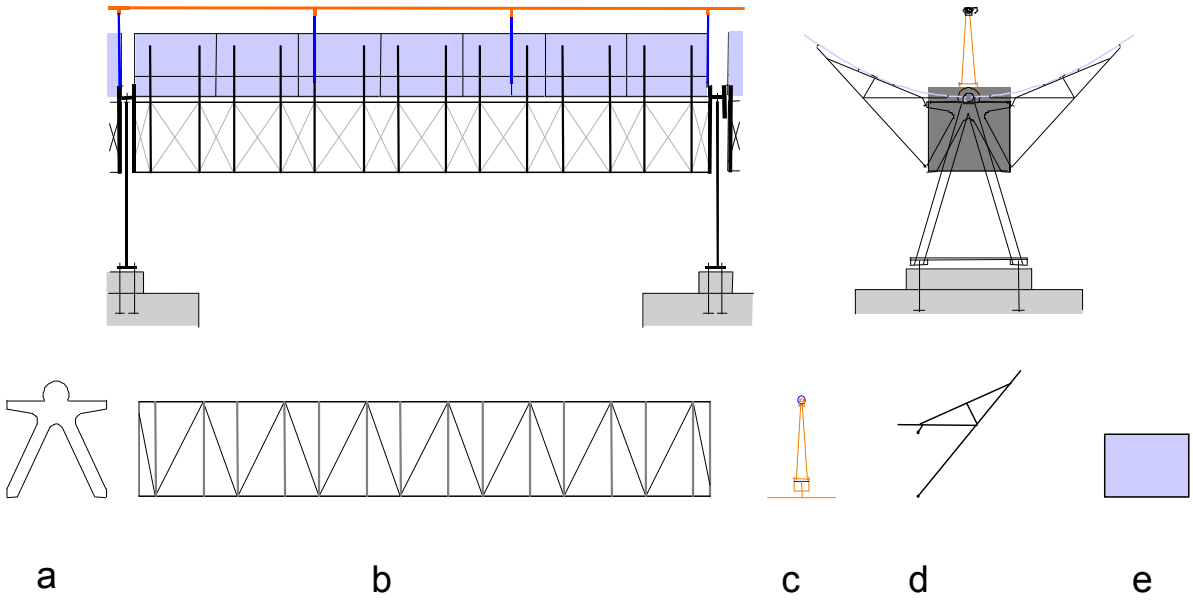

Source: Geyer et al. (2011).
Note: It consists out of: a) 2 endplates; b) 4 simple steel frames screwed to a torque box; c) 3 absorber tube supports; d) 28 cantilever arms; e) 28 mirror facets.

As shown in Figure 2.16, the receiver tube is a core component of the PTCs. It is typically four meters long, and the interior tube is a commercial-type metal receiver tube with an external diameter of around 70 mm. In contrast, the outer tube is a glazed shield tube with an external diameter in the range of 115 to 125 mm. Due to the receiver tube and glazed shield tube having different expansion coefficients and thermal intensities during operation, high-temperature-resistant glass and metal sealing pieces are required as transition pieces to ensure an airtight connection. In addition, a corrugated

Table 2.5 – Solar collector assemblies characteristics

Parameter	ET150	UT	Unit
Geometry			
Absorber diameter	0.070	0.089	m
Aperture width	5.76	7.51	m
Collector Length	148.5	243.3	m
Aperture area	828	1716	m^2
Assembly			
Number of modules per assembly	12	10	–
Number of glass facets	336	–	–
Number of absorber tubes	36	–	–
Steel structure weight	18.5	–	kg m^{-2}
Optical properties			
Focal Length	1.71	1.71	m
Mirror reflectance	94	95	%
Peak efficiency	75.0	82.7	%
IAM coeficient a_0	0	–	–
IAM coeficient a_1	1.0596×10^{-4}	–	$^{\circ-1}$
IAM coeficient a_2	-1.7091×10^{-4}	–	$^{\circ-2}$
Thermal properties			
Heat loss coeficient a_0	4.05	–	W m^{-1}
Heat loss coeficient a_1	0.247	–	W m^{-1} K^{-1}
Heat loss coeficient a_2	0	–	W m^{-1} K^{-2}
Heat loss coeficient a_3	0	–	W m^{-1} K^{-3}
Heat loss coeficient a_4	0	–	W m^{-1} K^{-4}
Heat loss coeficient b_0	0	–	W m^{-1}
Heat loss coeficient b_1	0	–	W m^{-1} K^{-1}
Heat loss coeficient b_2	0	–	W m^{-1} K^{-2}
Heat loss coeficient b_3	0	–	W m^{-1} K^{-3}
Heat loss coeficient b_4	0	–	W m^{-1} K^{-4}
Heat loss coeficient c_1	0	–	W m^{-1} $℃^{-1}$
Heat loss coeficient c_2	-1.46×10^{-3}	–	W m^{-1} $℃^{-2}$
Heat loss coeficient c_3	5.65×10^{-6}	–	W m^{-3} $℃^{-1}$
Heat loss coeficient d_1	0	–	W m^{-1} $℃^{-1}$
Heat loss coeficient d_2	7.62×10^{-8}	–	W m^{-2} $℃^{-1}$

Source: Data from Riffelmann et al. (2014) and STEAG (2020).

metal pipe is used as the thermal stress buffer section to relieve the longitudinal thermal expansion difference between the metal receiver tube and the glazed shield tube (see Figure 2.17). Finally, a getter must be mounted between the metal glass tubes to ensure the degree of vacuum in the intern layers of the receiver tube (WANG, 2019).

Furthermore, the vacuum seal undertakes great thermal stress that may quickly invalidate the sealing of glass and metal. Therefore, thin-walled materials with good reflection performance are required as a solar shade to block radiation while reflecting it to the metal receiver tube. The thermal properties and life of the PTC receiver tube are determined by the vacuum degree of the intern vacuum layer. If it is damaged, the heat losses may rapidly increase. In addition, the receiver's selective coating may deteriorate

Figure 2.17 – Receiver tube scheme

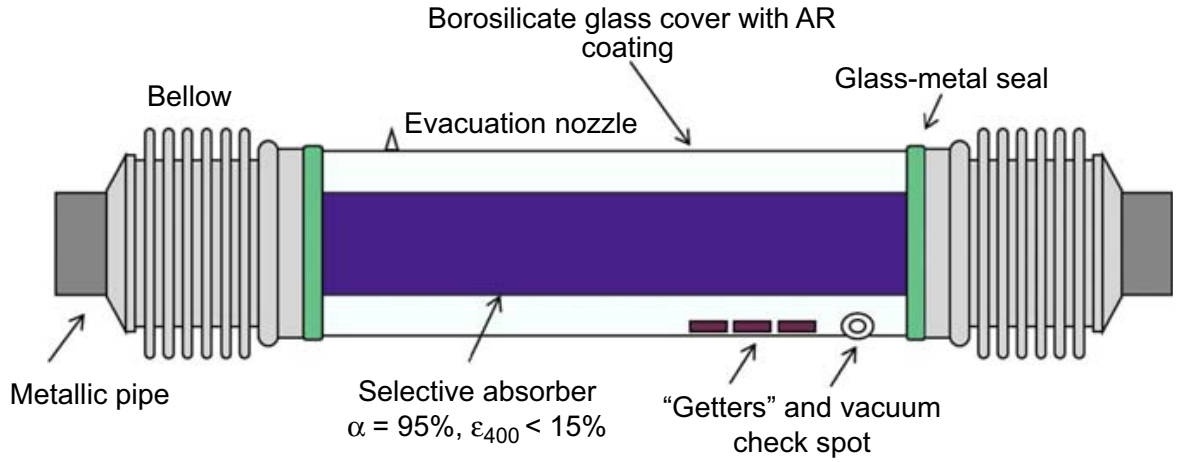

Source: Blanco and Santigosa (2017)

due to oxidation, resulting in a severe reduction of the receiver tube's optical efficiency. Therefore, according to Wang (2019), under the particular working conditions of high temperature and intense radiation, CSP performance and vacuum life are only ensured when the materials and properties of these components satisfy specific requirements:

- *Glazed shield tube*. Alternating thermal stress may be generated at the tube's seal. Thus it requires high hardness, thermal stability, and corrosion resistance. Materials widely applied presently include borosilicate glasses featuring high hardness, good optical properties, and corrosion resistance;
- *Metal receiver tube*. Under solar irradiance concentration, the temperature of the metal receiver tube will be much higher than 400 ℃. Thus, it must be equipped with high temperature and corrosion resistance. The expansion coefficient shall be as small as possible to eliminate the influences of axial expansion on the collector bracket. Due to thermal and gravitational influences, downward deflection may occur, so there must be a sufficient distance between the exterior wall and the interior wall of the glass tube. Currently, 316L stainless steel is typically used with an external diameter of 70 mm, a wall thickness in the range of 3-5.5 mm, a standard length of 4060 mm, and a mean roughness of less than 0.5 mm;
- *Glass-metal sealing*. A particular sealing alloy is applied to solve the inconsistency of the expansion coefficients of the interior metal tube and outer glass tube. Therefore, both expansion coefficients shall be as close to each other in value as possible to satisfy matched sealing and easier welding to the corrugated pipe;
- *Thermal stress buffer*. A buffer is required to compensate for the expansions of the metal receiver tube and the glazed shield tube. Thus, it must have good flexibility, excellent tension fatigue strength and life, high-temperature resistance,

and corrosion resistance. The respective length shall be as short as possible to increase the effective concentration length of the receiver tube;

- *Getter*. After the tube sealing, a getter is used to absorb the gases released by the HTF under high-temperature and residual gases in the vacuum interlayer. It is performed mainly by relying on physical and chemical absorption;
- *Selective absorption film*. Depending to its working mechanism, it can be categorized as optical interference, intrinsic absorption, metal ceramic, or multilayered gradient film. The most widely applied selective absorption film is a composite material made of multilayered gradient metal ceramic film and double-layered absorption film. As a general requirement for temperatures below 400 ℃, its absorptance shall be superior than 0.95 and its reflectance shall be less than 0.14. The most widely applied selective coating is a composite of metal-ceramic film and double-layered absorption film.

2.3 HEAT TRANSFER FLUIDS

Historically, the most used HTF in PTC is synthetic oil, composed of a eutectic mixture of biphenyl ($C_{12}H_{10}$) and diphenyl oxide ($C_{12}H_{10}O$). It is present in 71% of the plants currently in operation or planning and development phases (see Figure 2.19). Eastman Chemical Company sells it under the label of Therminol VP-1 (EASTMAN, 2019) and Dow Chemical Company as the brand name Dowtherm A (DOW, 2021).

Its advantages are its low freezing point (12 ℃), low corrosion potential, high specific heat, and good thermal conductivity. However, it also has several disadvantages: it limits the solar field's maximum operating temperature to 400 ℃ due to thermal degradation. Furthermore, this oil is not indicated to be used as a HSM, because it exhibits a high vapor pressure at elevated temperatures (approximately 10 bar at 390 ℃). So an indirect TES, using a secondary fluid, is more suitable (RAADE; PADOWITZ, 2011). A schematic of such a plant is shown in Figure 2.18.

Figure 2.19 presents the HTF usage by each of the main CSP technologies. In contrast to PTC it can also be observed that most SPT and LFR plants use molten salt and water-steam as HTF.

The current synthetic oils have two clear limitations, their degradation at temperatures at 400 ℃, which impose a severe barrier to increasing power block efficiency, and the environmental and fire hazards – spontaneously combustion can occur over 621 ℃ – due to possible leakages. Consequently, they must comply with strict environmental and safety requirements (Solutia Inc. 2012).

On this account, alternative fluids are being evaluated as a replacement, such as water-steam (DSG), molten salts (DMS), and pressurized gases. However, all three have advantages and disadvantages compared to thermal oil, as listed in Table 2.6.

Figure 2.18 – Scheme of a conventional concentrated solar power plant

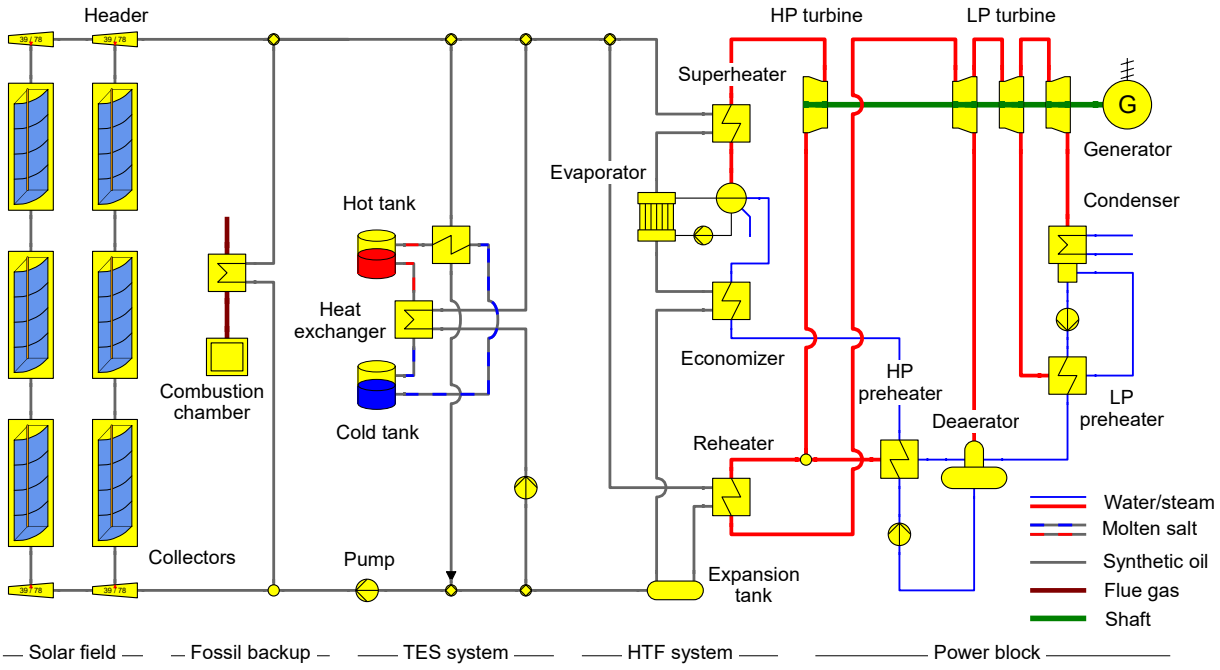

Source: Elaborated by the author using EBSILON Professional (STEAG, 2020).
Note: It uses synthetic oil used as HTF at a PTC solar field, and molten salt used in a I2T TES.

Figure 2.19 – Heat transfer fluid used in concentrated solar power projects

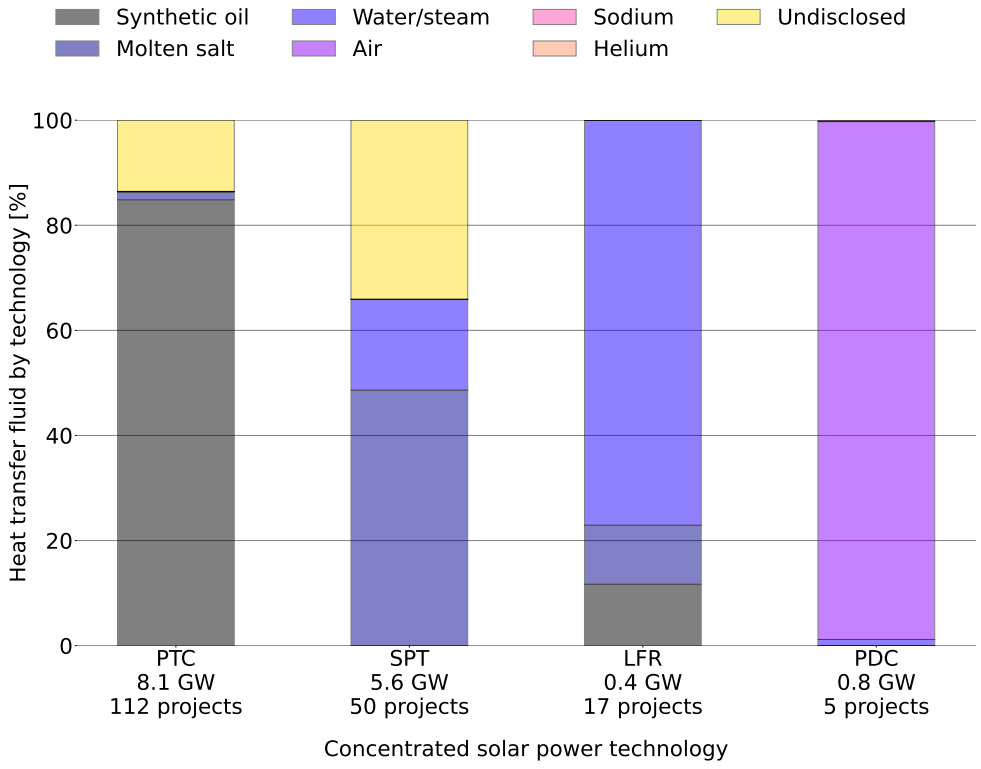

Source: Elaborated using Matplotlib (HUNTER, 2007) with data from SolarPACES (2021).
Note: Despite their use in experimental projects, Sodium and Helium do not represent significant installed capacities.

Table 2.6 – Alternative working fluids compared to synthetic oil

Fluid	**Advantages**	**Disadvantages**
Water-steam (Direct steam generation)	– Simpler plant configuration; – Higher steam temperature; – No fire hazard; – No pollutant.	– Lack of cost-effective TES; – Complexity of solar field control; – Higher pressure in piping.
Molten salts (Direct molten salt)	– Higher steam temperature; – Cheaper thermal storage; – No fire hazard; – Not pollutant.	– Freezing hazard; – Complex solar field design; – Higher electricity self-consumption.
He, CO_2, N_2 and air (Pressurized gases)	– Higher steam temperature; – Cheaper thermal storage; – No fire hazard; – Not pollutant.	– Lower heat transfer coefficient; – Complexity of solar field control; – Higher pressure in piping; – Higher pumping power.

Source: Data from Blanco and Santigosa (2017).

2.3.1 Direct steam generation

The use of water steam can avoid the problems associated with thermal oil. This application is best known as for DSG, and its main advantage is the layout simplification because the steam demanded by the power cycle is straightforwardly produced in the absorber tubes, not demanding heat exchangers. Also, the absence of a HTF degradation temperature enables the reach of far higher temperatures and consequently higher power cycle efficiencies. Nevertheless, since the solar field thermal losses also increase with the temperature, higher temperatures do not increase the overall plant efficiency at the same pace as the power block efficiency.

As for disadvantages, the two-phase flow (i.e., liquid water and steam) in the evaporating section of the solar field introduces some technical constraints, demanding complex control to keep the solar field's temperature, pressure, and flow regime stable during solar radiation transients. Another significant barrier for this technology is the lack of a commercial proven TES with a large storage capacity. Conventional STES are unsuitable for DSG, once the steam must be condensed to more efficiently release its thermal energy. Since condensation occurs at a constant temperature, a LTES is recommended. Such systems must use a HSM that shifts between physical states (e.g., melt or evaporation) while charging by steam condensation, broadly called PCMs. Although LTESs are already underway, much R&D is still needed before commercial units become available.

As example, the studies by Ferreira (2018) and Marugán-Cruz et al. (2019) focus on modeling and analysis in CSP-LFR-DSG plants with sensible-latent TES.

According to Solargis (2019), there are one PTC-DSG and four LFR-DSG plants currently in operation, and another four LFC-DSG are under development and construction. Among those, six feature STES, implementing Ruth's tanks (steam accumulators)

or concrete storages. An example is Puerto Errado 2, an LFC DSG commercial plant in Spain. It has a net capacity of 30 MW and a steam accumulator of 0.5 hours, providing an average of 49 GWh yearly. Some studies propose combining the advantages of STES and LTES (see Figure 2.20), aiming the system capital costs reduction. For example, in the ITES project, a three-part TES prototype is validated for DSG. PCM is employed for LTES in the evaporation and condensation as LTES, and concrete is used in the preheating superheating for STES, resulting in 1 MWh of storage.

Figure 2.20 – Scheme of a direct steam generation concentrated solar power plant

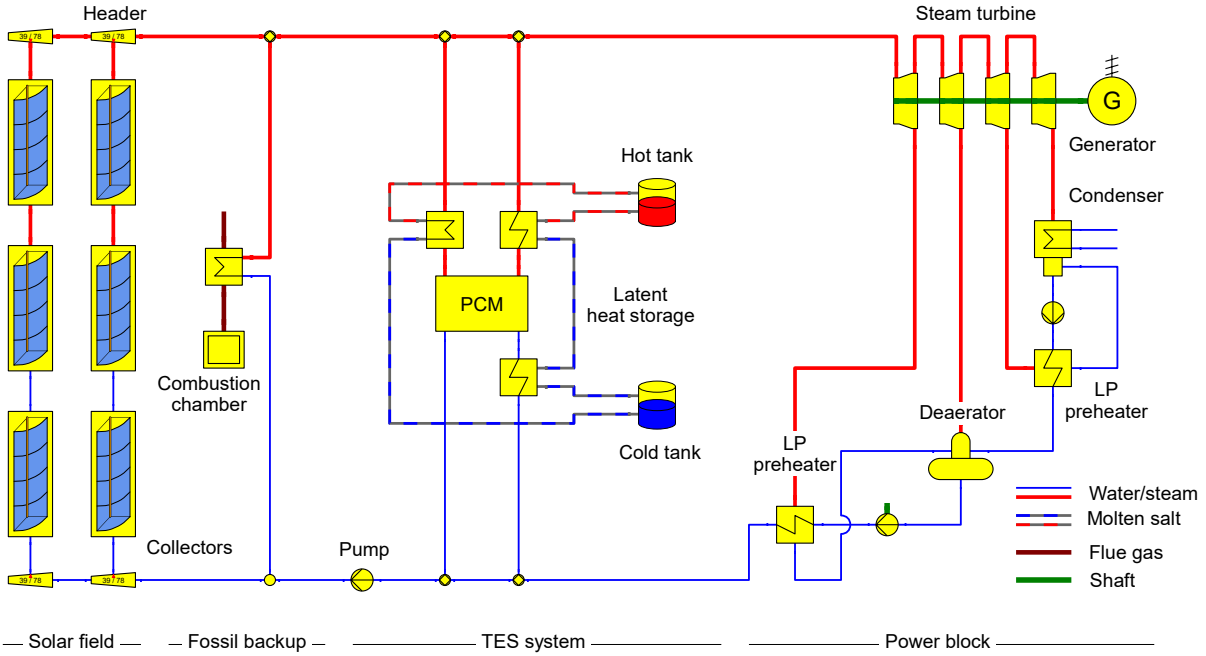

Source: Elaborated using EBSILON Professional (STEAG, 2020) based in Ferreira (2018).
Note: It uses a LFR solar field and a sensible-latent TES. The sensible heat is stored by two molten salt tanks, while the latent heat storage is performed by a PCM. More information about this kind of layout is provided by Seitz et al. (2014).

2.3.2 Direct molten salt

A more promising HTF seems to be nitrate and nitrite salt mixtures. Using the same molten salt in the solar field and the thermal storage system has clear benefits. This configuration, known as DMS, is widely used in SPT facilities (e.g., Gemasolar, in Sevilla, Spain), while it is in the early stages for LFR and PTC. It is used in one operational LFR power plant – the Dacheng Dunhuang 50 MW_e Molten Salt Fresnel project –, and in four PTC projects – two operational, Archimede (5 MW) and the ASE Demo plant (0.315 MW), both in Italy and in two plants in China, Gansu Akesai 50MW Molten Salt Trough project and the Chamber 64 MW Molten Salt Parabolic Trough

project, currently under construction and development, respectively (SOLARPACES, 2021).

There are several advantages to using molten salt instead of organic compounds as HTF in PTC solar power plants. First, the thermal stability of molten salts allows higher temperatures in the solar field – up to 600 ℃, even at atmospheric pressure. Second, it results in higher temperatures in the power cycle, improving thermodynamic efficiency.

When those salt mixtures are heated beyond their melting point, their cations and anions are dissociated. As a result, molten salts have thermal and chemical stability in a broader temperature range, relatively high density, heat capacity, good thermal and electric conductivity, low corrosion rates in common piping materials, low viscosity, and vapor pressure, even at elevated temperatures (WAGNER, P. H., 2012). Besides that, nitrate salts generally exhibit good heat transfer properties and are relatively inexpensive. Because of that, they are favorable for use as HTF and HSM and could bring significant improvement to plant efficiency and decrease in overall cost (TEMLETT, 2018).

Because of their low price and suitable properties, molten salts are also widely used as a HSM. Unlike Therminol VP-1, they are compatible with direct storage and present shallow vapor pressure, allowing storage under atmospheric pressure and eliminating costs associated with reservoirs walls tickness. In addition, by implementing them in direct storage, fewer components are required; oil-salt heat exchangers and expansion vessels are no longer needed, and the size of the salt storage tanks can decrease (see Figure 2.21). Moreover, nitrate and nitrite salts are not toxic and have a high autoignition temperature. Thus, leakage and fire hazards are negligible (Benmarraze 2010).

Salt varieties are available from diverse suppliers. Table 2.7 compares the properties of Therminol VP-1 with three commercial salt mixtures sold by Solutia Inc.: Solar Salt, Hitec, and Hitec XL. Solar salt is a non-eutectic binary mixture of potassium nitrate and sodium nitrate. Hitec and Hitec XL are both eutectic ternary mixtures of sodium and potassium nitrates, and sodium nitrite or calcium nitrate ($Ca(NO_3)_2$). In addition, liquid sodium and new molten salts with a lower freezing temperature are currently under development.

Solar salt is the cheapest and more stable salt in terms of thermal composition, usable at temperatures of up to 600 ℃ under atmospheric conditions, the temperature at which thermal decomposition starts.

Its viscosity is about 12 times higher than Therminol VP-1. As a consequence, pumping elements usually require more power per mass unit. Nevertheless, the mass flow in the solar field is considerably lower with molten salt, which leads to a lower pressure loss in the piping. Both effects combined (low mass flow and pressure loss) lead to lower parasitic power needed than oil-based solar fields (KEARNEY et al.,

Figure 2.21 – Scheme of a direct molten salt concentrated solar power plant

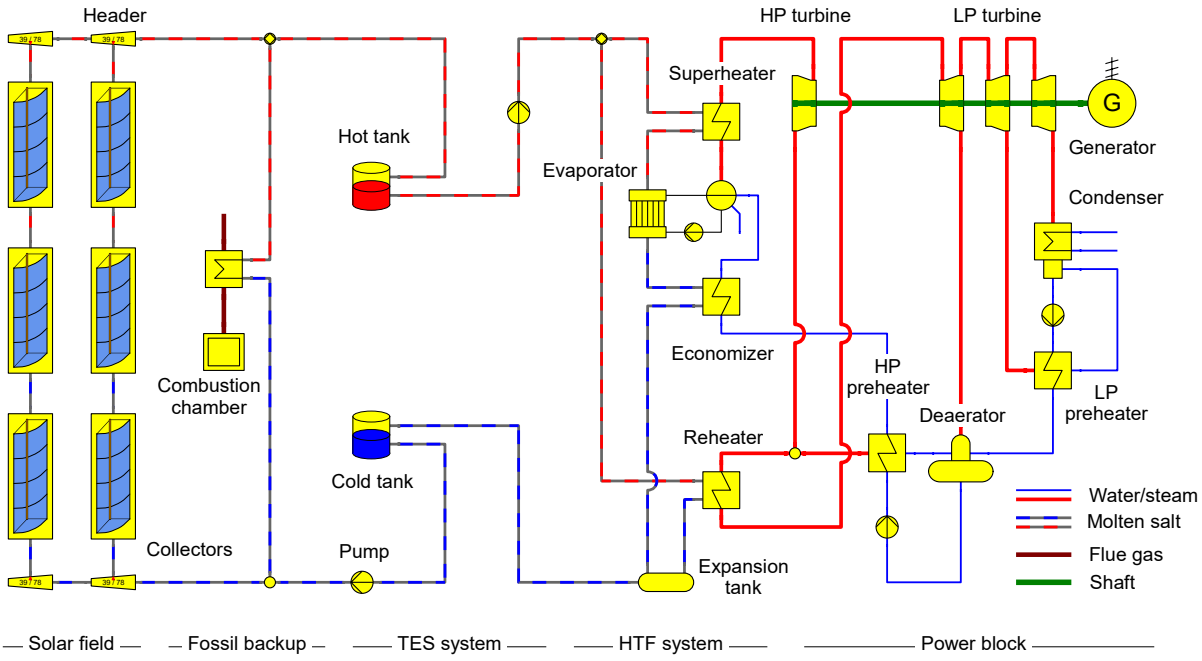

Source: Elaborated by the author using EBSILON Professional (STEAG, 2020).
Note: It uses molten salt both in a parabolic trough collectors solar field and in a D2T TES.

Table 2.7 – Properties of Therminol VP-1, solar salt, Hitec and Hitec XL

Property	Therminol VP-1	Solar salt	Hitec	Hitec XL	Unit
Composition					
Diphenyl – $C_{12}H_{10}$	26.5	–	–	–	wt%
Diphenyl oxide – $C_{12}H_{10}O$	73.5	–	–	–	wt%
Sodium nitrite – $NaNO_2$	–	–	40	–	wt%
Sodium nitrate – $NaNO_3$	–	60	7	7	wt%
Potassium nitrate – KNO_3	–	40	53	45	wt%
Calcium nitrate – $Ca(NO_3)_2$	–	–	–	48	wt%
Thermophysical					
Freezing temperature	13	220	142	120	℃
Upper temperature	400	600	535	500	℃
Specific weight	694	1834	1790	1903	kg m^{-3}
Specific heat	2.63	1.51	1.56	1.41	kJ kg^{-1} K^{-1}
Volumetric heat capacity	1825	2769	2792	2683	kJ m^{-3} K^{-1}
Thermal conductivity	0.076	0.517	0.331	0.519	W m^{-1} K^{-1}
Viscosity	0.143	1.910	2.167	2.267	mPa s
Economic					
Specific cost	2.20	0.49	0.93	1.19	USD kg^{-1}

Source: Data from Patrick Hubert Wagner (2012) and STEAG (2020).
Note: Thermophysical properties at 400 ℃ and 1 bar. The upper temperature varies in the literature.

2004).

Because the volumetric heat capacity of the molten salt is higher than that

of Therminol VP-1, the velocity is lower. This factor is more significant than the lower viscosity. As a result, low storage system investment costs make a high storage capacity economically viable, and a molten salt-based CSP installation can produce electricity even at night. In addition, power plant efficiency is also increased during the night because the ambient temperature is reduced.

Regrettably, molten salts also have disadvantages. Solar salt has a very high freezing temperature, at 220 ℃, necessitating energy-intensive freeze protection to avoid the blockage of pipes and valves. In addition, it involves installing additional hardware (e.g., electric heating elements, heat tracing, or insulation), which in turn entails high investment and operation costs (KEARNEY et al., 2004). Higher process temperatures also raise the average temperature of the solar field, leading to pipe, valve, and pump corrosion and causing higher heat losses per radiation and hindering its efficiency and cost reduction benefits.

In the case of indirect two-tank TES systems integrated into parabolic trough plants, the freezing point issue becomes more relevant. First, because of the freezing point of the molten salts and the properties of the oils used, the power cycle in these systems is restricted to operate between 250 ℃ and 395 ℃, which negatively impacts the system's efficiency. Secondly, additional heat exchangers are needed, which can further increase the required investment for the TES system.

2.3.3 Compressed gas

The use of pressurized gases is another option to replace the current HTFs used in CSP. They are safe from an environmental perspective since they do not pose fire hazards and environmental constraints associated with thermal oils. Similar to molten salts, higher HTF working temperatures are achieved, enhancing the power cycle efficiency (BLANCO; SANTIGOSA, 2017). Furthermore, higher temperature differences between the solar field outlet and inlet can enhance STES systems efficiency, increasing storage density and thus reducing the required amount of HSM.

The requirements in selecting the proper gas involve thermal, hydraulic, and economic characteristics, bearing in mind the feasibility of a commercial plant. This principle leads to gases extensively used in the industry for similar working conditions. Thus, the state-of-the-art gases are helium, carbon dioxide, nitrogen, and air [(9)], which properties are shown in Table 2.8.

Helium seems to be a good option considering its thermal conductivity and specific heat. However, high costs and leakages due to its tiny molecules represent a severe barrier to its application. On the other hand, carbon dioxide shows a higher density in similar conditions, reducing pumping consumption and increasing the overall installation efficiency. Therefore, carbon dioxide is nowadays considered the best candi-

[(9)] Due to its composition (75.5 wt% N_2), air presents similar properties to nitrogen.

Table 2.8 – Properties of gases of interest

Property	**Carbon dioxide – CO_2**	**Helium – He**	**Nitrogen – N_2**	**Unit**
Density	78.83	7.024	47.96	kg m^{-3}
Thermal conductivity	49.68	278.40	50.74	kW m^{-1} $℃^{-1}$
Viscosity	31.48×10^{-6}	35.07×10^{-6}	32.58×10^{-6}	Pa s
Specific heat	1.171	5.186	1.114	kJ kg^{-1} $℃^{-1}$
Prandtl number	0.74	0.65	0.71	–

Source: Data from Blanco and Santigosa (2017).

Note: Thermal properties at 100 bar and 400 ℃. The Prandtl number (*Pr*) is the ratio between momentum and thermal diffusivities; small values ($Pr \ll 1$) mean the thermal diffusivity dominates heat transfer, whereas large values ($Pr \gg 1$) indicate the predominance of momentum diffusivity.

date for gaseous HTF applications, especially when working at supercritical conditions (T >31 ℃ and T >7.4 MPa).

An evaluation of the technical and economic feasibility of pressurized gases was performed at PSA. The experiment addressed the use of HTF in the gas-cooled solar collectors' project.It included analyzing several gases as HTF (helium, carbon dioxide, nitrogen, and air). The solar collectors could be connected in series or parallel, depending on the intended outlet temperature (525 ℃, or 400 ℃, respectively). The nominal inlet temperature was 225 ℃ in both cases. In addition, the solar field was connected to a I2T molten salt TES to evaluate the performance of the solar collectors with pressurized gas and the system's overall performance composed of the solar field and the TES. This facility delivered very interesting and valuable results related to the feasibility of pressurized gases for PTCs.

Nonetheless, pressurized gasses also have some disadvantages when compared to thermal oils. Their lower density reduces heat transfer coefficients in the receivers and increases the required pumping power. One way to reduce those negative impacts is increasing the working pressure, as the required pumping power of gases to compensate for circuit pressure drop is inversely proportional to the square of the pressure. However, that requires more robust components to withstand the higher loads.

In the case of carbon dioxide, the water presence can trigger carbonic acid (H_2CO_3) formation, which is corrosive to carbon steel, widely used in solar plants. Thus, carbon dioxide would imply a rigid humidity control to avoid humidity condensation inside the pipes and vessels. Another major problem found at PSA when working with supercritical carbon dioxide (sCO_2) was its incompatibility with the graphite sealing used at the end of the receiver tubes to allow thermal expansion and rotation. The graphite sealings were damaged very soon at working temperatures higher than 400 ℃. However, no problem was found for lower temperatures. Thus, although air does not have the drying requirements of carbon dioxide, it would still require preventive

measures to limit the water content in the circuit.

On the contrary, nitrogen presents fewer corrosion issues than carbon dioxide or air and can be obtained in loco simply from compressed air through a nitrogen generator. Therefore, nitrogen could be the most feasible HTF among the proposed gases. Furthermore, the cost of synthetic oil and the related equipment (such as pumps, expansion vessels, and conditioning systems) will be replaced by a lower cost of nitrogen. However, the overall costs of a large solar field with nitrogen will be higher than that of an oil-based field due to the increasing cost of blowers and heat exchangers.

2.3.4 Liquid metals

Liquid metals are chemically stable over their entire temperature range. It means they have a more extensive operating temperature range and an upper-temperature limit of around 1000 ℃, which would significantly increase power plants' efficiency. The first metal investigated is sodium in various compositions like NaK, liquid at room temperature. The other is LBE, which has a higher boiling point.

Liquid metals have higher heat transfer coefficients and operating temperatures, improving receiver efficiency and higher receiver fluid outlet temperature. With the use of liquid metals. For solar salts, the optimum heat transfer in the optical receiver can be increased up to five time the ones obtained for molten salts, which would result in significant investment cost reductions. However, due to the relatively low heat capacity of metals, they cannot be used as a storage medium, thus making a direct TES system using liquid metals economically unattractive. Since molten salts cannot accommodate the higher temperature of the liquid metals, a different thermal storage system would have to be used, such as solid HSM. Another issue with liquid metals is that sodium reacts violently with water, and LBE has health risks (TEMLETT, 2018).

2.4 ENERGY STORAGE

The oldest form of energy storage probably involves the harvest and stocking ice for tasks that mechanical refrigeration satisfies today, including preserving food, cooling beverages, and air-conditioning.

Significant technological developments happened throughout the nineteenth century when chemical batteries became a common way to power electrical devices, such as street and traffic lights and telegraphs. At that time, electricity was majorly transmitted as direct current, so incorporating batteries was relatively simple.

In 1896, Homer Yaryan (1842-1928) installed a storage tank at a water heating facility in the USA, capturing excess heat when electric demand was high. Additionally, in the same period, other forms of storage were also used, including compressed air and high-temperature water, converted into steam to drive heat engines.

Today, storage is a crucial aspect for many energy technologies. The massive amounts of petroleum stored worldwide are necessary for the reliable, economic availability of fuels and petrochemicals. Some hydropower utilities also store energy using pumped storage; large electric motors pump water uphill to elevated reservoirs during low electric demand. Then, during periods of peak demand, the water is allowed to flow back downhill to redeliver the energy through hydroelectric generation.

Energy storage also includes technologies for storing heat. In thermodynamic terms, such systems hold transferred heat before it is put to practical purposes. A conventional example is hot water storage in residences and industries. Such heat storage smoothes out the delivery of hot water or steam, but it is not usually considered for periods more extended than one day. Advanced new storage devices are often an integral part of other new technologies, and these sometimes can be made more feasible by innovations in storage. Advances in storage significantly benefit wind and solar energy technologies, as unlike nuclear and fossil-fired generation, they highly depend on the weather, thus presenting an intrinsic inconstant behavior.

Beyond those, a large variety of storage techniques are under development. Accounting for the energy form accumulated, they can be grouped into mechanical, thermal, chemical, biological, and magnetic, as shown in Figure 2.22.

Figure 2.22 – Classification of energy storage methods

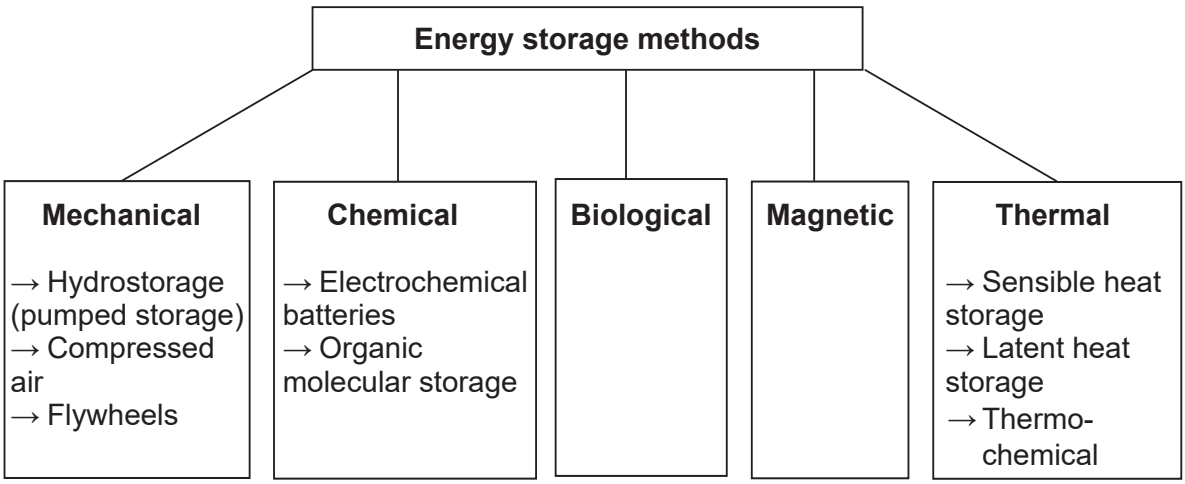

Source: Adapted from Hahn et al. (2017).

The availability and success of these storage technologies will significantly affect the success of the energy transition. To date, pumped hydro storage still by far dominates the global storage mix. According to IRENA (2017), it accounts for 96% of the total installed electric storage power capacity worldwide, followed by thermal storage ($\sim$2%), electrochemical storage ($\sim$1%), and other mechanical storage ($\sim$1%).

In the future, the share of electrochemical storage is expected to grow due to efficiency improvements and decreasing costs (IEA, 2020).

Despite this great variety, the basic principle is similar in every one of those techniques; what mainly varies is the kind of energy withhold and its timescale. For all of them, a complete storage cycle involves at least three steps: charging, storing, and discharging. Charging can be performed via multiple processes, e.g., by modifying a material's thermal, chemical, electrical, or mechanical energy. After that, the primary purpose is to keep the storage medium (i.e., the "battery") unchanged, so the stored energy can be subsequently recovered by the reverse process.

Of all the storage technologies, direct electricity storage is the most desirable. However, the use of batteries and capacitors is limited to restricted applications and over a short time. Mechanical energy storage using flywheels can also provide a small to medium amount of energy capacity. Storing energy on a large scale for supply over many hours is more feasible using TES, pumped hydro, or compressed air energy storage. Because of the need for elevated water reservoirs, pumped hydroelectric energy storage is only available in limited locations. Large-scale compressed air storages require a considerable volume, which is only realistic if large-volume underground space is available.

Additionally, using a combination of electrolysis and hydrogen fuel cells, electrical energy storage technology is considered a long-term energy storage technology. However, it requires hydrogen storage, and this technology still needs more research and development. Therefore, TES turns to be the most viable technology readily available with fewer limitations on location or quantity of energy storage for a short time. Moreover, thermal energy represents a significant share of energy consumption (see Figure 2.23). Thus, TES systems can also increase the reliability of thermal energy equipment and aid a large-scale transition from fossil fuels to renewables.

CSP presents a high capacity of integration with TES systems, which grants it greater dispatchability and reliability, and represents one of its most essential advantages from other renewables (BRAND et al., 2012). As can be observed in Figures 2.10, the storage unit is integrated into CSP plants between the solar field and the power block. Moreover, storage potentially makes solar-only baseload power possible. CSP plants with large TES capacities may produce baseload solar electricity day and night, making it technically possible for low-carbon plants to compete with fossil-fired plants. Despite that, the TES system enables many operation methods which, besides extending plant operation after sunset, can be elaborated to smooth generation transients occasioned by cloud cover, increase the annual installation output, or even its revenue.

In such an application, the TES primary operation strategy is quite simple: during charge, part of the heat absorbed at the solar field is directed to the storage unit, where it increases the HSM temperature, making it change between physical states or even both.

Figure 2.23 – World energy use by activity in 2016

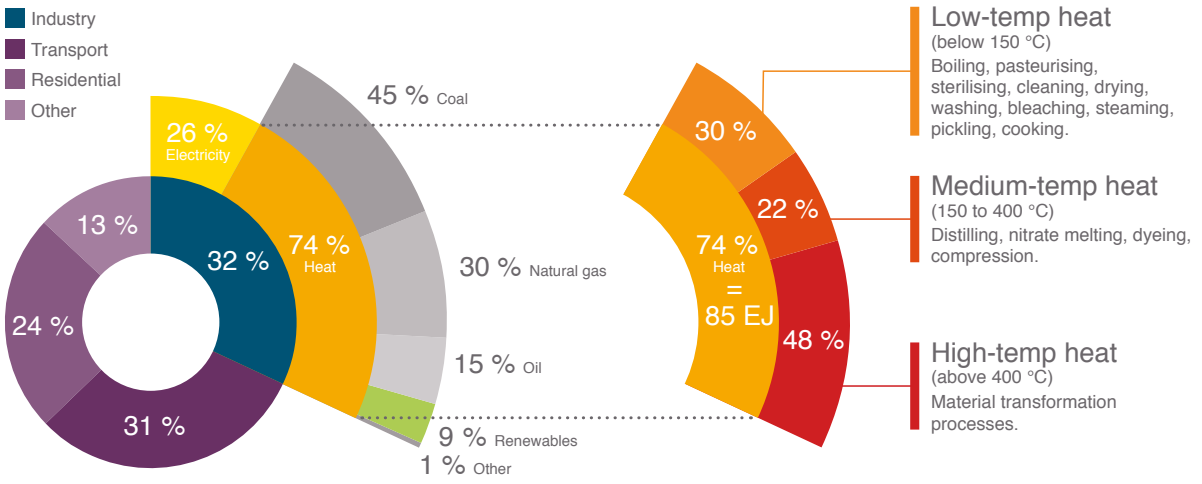

Source: Hahn et al. (2017).

At discharge, the Rankine cycle is powered by the energy stored in the TES (CABEZA, 2015). As a result, power demands are rarely constant over time. On this account, the excess generation available during low-demand periods can be used to charge a TES to increase the generation capacity during high-demand periods. Moreover, it also results in higher CFs and avoids the need for additional units. Another advantage is the shift of energy dispatch periods. It allows energy producers subject to time-of-day tariffs to shift power injection into the grid from low to high-cost periods.

The use of TES demands a more extensive solar field concerning the required solely by the power cycle. It happens because more heat is absorbed than the turbines need to operate at the rated power resulting in a more frequent energy surplus that can be stored, allowing extended and steady operation. In contrast, in the absence of such a system, plant operation would need to waste some valuable energy during the sunniest hours. However, this happens at the expense of a higher CAPEX; thus, storage cannot be expanded indefinitely.

Selecting appropriate technologies and designing highly efficient TES systems are becoming the primary focus of current research. In a recent review, Tian and Zhao (2013) summarized the main criteria for designing a solar TES system regarding technical, economic, and environmental aspects. Among those factors, the essential requirements of a TES system are a high energy density to reduce the required amount of HSM, reliable mechanical and chemical stability, and enhanced heat transfer. In addition, a current trend focuses on temperature increase, aiming to improve plant efficiency and reduce storage costs.

Besides that, the costs of the TES system (including storage materials, reservoirs, and heat exchangers) are also fundamental criteria that directly determine the cost of the energy produced and the investment payback period, so ideally, it must

be as low as possible. Moreover, storage materials should be environmentally friendly, low corrosive, non- or low-flammable, and allow recurring charge and discharge cycles, being fully reversible.

The TES alternatives can be classified in many forms. For example, according to the storage principle, TES technologies available or under development for CSP applications are divided into sensible, latent, and thermochemical. Alternatively, they can be grouped based on the motion state of HSM into active and passive concepts (LI; CHAN, 2017).

2.4.1 Classification by storage principle

Analyzing the technologies according to their storage principle, one can see that STES is currently the most common method, with many low-cost materials available. However, its poor energy density results in considerably large systems. In contrast, LTES has a higher energy density but a poor heat transfer due to the very low thermal conductivity of the applied materials.

While STES and LTES are already well established, TCES is still in the early stages of development. However, it seems to be the most promising technology for the future, as it presents the highest storage density. Nevertheless, problems such as the complex design of reactors, low chemical stability, degraded performance over the cyclic operation, reduced heat and mass transfers hinder its actual application in current CSP plants.

Table 2.9 summarizes the main characteristics of different TES technologies and main features.

2.4.1.1 Sensible thermal energy storage

In STES, thermal energy is stored or released by varying the HSM temperature. It is a purely physical process without any phase change. Therefore, the heat stored depends on the HSM's mass, specific heat, and temperature change. As a substance's temperature grows, the energy content also increases. The thermal energy required (Q) to heat a given mass of HSM ($m_{HSM} = \rho_{HSM}\ V_{HSM}$) from T_1 to T_2 temperature is given by

$$Q = \int_{T_1}^{T_2} \rho_{HSM}\ V_{HSM}\ c_{HSM}\ dT \tag{2.5}$$

where ρ_{HSM} is the specific mass, V_{HSM} is the c_{HSM} is the specific heat.

Other HSM properties are also crucial for STES performance and feasibility: the operating temperature, thermal conductivity and diffusivity, chemical and thermochemical stability, and costs. Moreover, the STES should be designed appropriately for heat

Table 2.9 – Summary of the different thermal energy storage technologies by principle

Characteristic	**STES**	**LTES**	**TCES**
Heat storage media cost	Low	Medium	Low
Energy density	Low	Medium	High
Temperature requirement	High	High	Low (ambient)
Technology feedback	Multiple experiments; majority of TES	More R&D needed	No feedback
Charge-discharge switch	Short time	Short time	Medium time
Heat transfer	Good	Slow; low thermal conductivity	
Advantages	Large commercial feedback; easy implementation	Constant operation temperature; medium energy density	Long-term storage; high energy density
Disadvantages	Heat losses during storage; low energy density; high freezing and variable discharge temperatures	Low thermal conductivity; solid deposits in the heat exchanger	Incomplete irreversibility; storage of gaseous byproducts; poor heat and mass transfer

Source: Data from Pelay et al. (2017).

discharge at relatively constant temperatures. The major drawback of this technology is its limited energy density.

Liquid materials for STES are currently the most studied and are at an advanced stage of development. Molten salts are considered one of the best materials for such applications due to their features, including excellent thermal stability at high temperatures, low vapor pressure, low viscosity, and high thermal conductivity, non-flammability, and non-toxicity. The two leading molten salts are Solar Salt – 60% NaNO3 and 40% KNO3 – and HitecXL – 48% Na(NO3)2, 7% NaNO3 and 45% KNO3. Solar Salt is used, e.g., in Archimede, Italia and "MSEE/CatB", USA. Additionally, HitecXL was tested in the PSA, Spain, and Themis, France. It was developed as a second option for Hitec – 40% $NaNO_2$, 7% $NaNO_3$ and 53% KNO_3.

A new series of ternary salts mixtures was proposed with ultra-low melting temperatures around 80 ℃, preventing the HSM solidification and making the TES system much easier to manage. For example, mixtures of salts consisting of KNO_3, $LiNO_3$, and $Ca(NO_3)_2$ shows viscosities five times lower than commercial synthetic oils and molten salts, as reported by Wang (2019).

Other liquid materials are also used as HSM in CSP plants and experiments, for example synthetic oils and liquid sodium. However, additional safety measures are necessary by the latter due to its unstable nature caused by high vapor pressure, which may cause serious safety issues (PELAY et al., 2020).

Solid HSMs generally withstand wide ranges of temperatures, with high thermal

conductivity and relatively low cost. Additionally, concrete and ceramics are intensively studied, with good characteristics as solid HSMs.In order to improve the stability of concrete at high temperatures, a new mixture with polypropylene fibers was specially developed.A comprehensive list of HSM for CSP applications and their main characteristics are provided by Gil et al. (2010).

Practical solutions to increase the energy density of solid and liquid STESs include adding encapsulated PCMs or nanoparticles. Encapsulation means coating PCM particles with a protecting shell to improve the chemical stability and prevent individual particles from coalescing during cyclic operation. Adding encapsulated PCMs in suitable materials can be considered a new coupled technology. Likewise, properly adding nanoparticles to HSM can increase its specific heat. For example, Andreu-Cabedo et al. (2014) showed that the specific heat of a Solar Salt could be increased by 25% by adding 1 wt% of silica – SiO2.

Lastly, gaseous materials, such as compressed air or steam, have been used in operating CSP plants (e.g., "Exresol-1," "Planta Solar 20," and "Planta Solar 10" in Spain). The advantages of using gaseous materials are their availability, low cost, non-toxicity, and wide range of operating temperatures. On the other hand, the drawbacks of using gaseous materials are low thermal conductivity and low energy density. Furthermore, even if these gases are stored compressed, the large reservoir's volume makes this option very challenging for large-scale CSP plants.

2.4.1.2 Latent heat storage

In LTES, thermal energy is stored or released by a material changing its physical state [(10)]. It is also a purely physical process, without any chemical reaction during charge or discharge. Consequently, the heat stored is dependent mainly on the latent heat of phase change (L).

$$Q = \rho_{HSM} V_{HSM} L_{HSM} \tag{2.6}$$

Because of that, PCMs for LTES have the advantage of higher energy densities, charging and discharging in narrow temperature ranges, close to their phase change temperature. PCMs are either packaged in specialized containers such as tubes, shallow panels or encapsulated as self-contained elements.

It is relatively straightforward to determine the sensible heat of phase change value for solids and liquids, but it is more intricate for gases. For example, suppose a gas restricted to a specific volume is heated, both the temperature and the pressure increase. The specific heat observed in this case is called the specific heat at constant

[(10)] it occurs at a constant temperature for pure substances, while for eutectic and azeotropic mixtures, it happens at solid-liquid and liquid-vapor transition, respectively.

volume (c_V). Instead, if the volume can vary at a fixed pressure, the specific heat at constant pressure (c_p) is obtained.

The main disadvantage of PCMs is their low thermal conductivity, resulting in prolonged charge and discharge processes. Several approaches may be considered to enhance heat transfer, including adding thermal conductivity promoters (e.g., graphite, metal of foam matrixes, fins, high conductivity particles, micro-encapsulation of the PCMs, heat pipes),and using high conductivity PCMs made of metal alloys. PCMs made of metallic alloys (i.e., Mg-Zn-Al) have the advantages such as high thermal conductivity (around two orders of magnitude higher than molten salts) and good thermochemical stability. However, their high price (between 2 and 3 USD kg^{-1}) is an obstacle for implementing large-scale LTES. Recent advances on the geometrical configurations of LTES are reviewed by Mao (2016).

Inorganic and organic substances with potential use as thermal storage material at high temperature and their physical properties are listed by Gil et al. (2010) and Sharma et al. (2015). The melting temperature of these PCMs generally varies between 100 and 900 ℃, yet materials with lower transition temperatures (between 100 and 300 ℃) are more suitable for LTES in linear concentration CSP. On the other hand, materials with higher phase change temperatures (higher than 400 ℃) can be used in punctual concentration CSP.

2.4.1.3 Thermochemical heat storage

Unlike sensible or latent heat storage, TCES is based on reversible chemical reactions, characterized by a change in the molecular configuration of the reagents. First, solar energy is used to drive an endothermic chemical reaction; then, it is stored as chemical potential. Finally, the reversed exothermic reaction enables the recovery of the stored heat at discharge, sometimes by adding a catalyst. The advantages of TCES rely on its superior energy density (up to 10 times greater than LTES)and the possibility to preserve the stored energy for more extended periods. As a result, it is a desirable option and fairly economically competitive

Reactions involving metallic hydrides, carbonates, hydroxides, redox, ammonia, and organic reagents can be used for TCES units in medium or high temperatures (300–1000 ℃). The review by Pelay et al. (2017) groups these reactions with their main characteristics, advantages, disadvantages, and experimental feedback.

Meanwhile, common technical problems of the materials used for TCES are low thermal conductivity (which slows the heat transfer) and low permeability (which reduces the mass transfer), which remain to be solved. Additionally, some reactions suffer from incomplete reversibility, a crucial drawback for TCES because their storage capability gradually decreases over multiple cycles.

Hence, many studies are devoted to the material properties and reactor designs

to enhance the mass transfer during combination and the heat transfer during decomposition. Recent advancements and proposed methods are reviewed by Aydin et al. (2015).

2.4.2 Classification by the motion of heat storage medium

Based on the motion state of storage materials during charge or discharge, the TES concepts can be broadly classified into two concepts: active and passive. The HSM itself flows to absorb (charge) or release (discharge) heat by forced convection in active systems. In contrast, the HSM does not flow through heat exchangers; it is heated or cooled just by HTF circulation.

Additionally, Figure 2.24 shows possible integration concepts of STES in a CSP facility.

Figure 2.24 – Sensible thermal energy storage systems

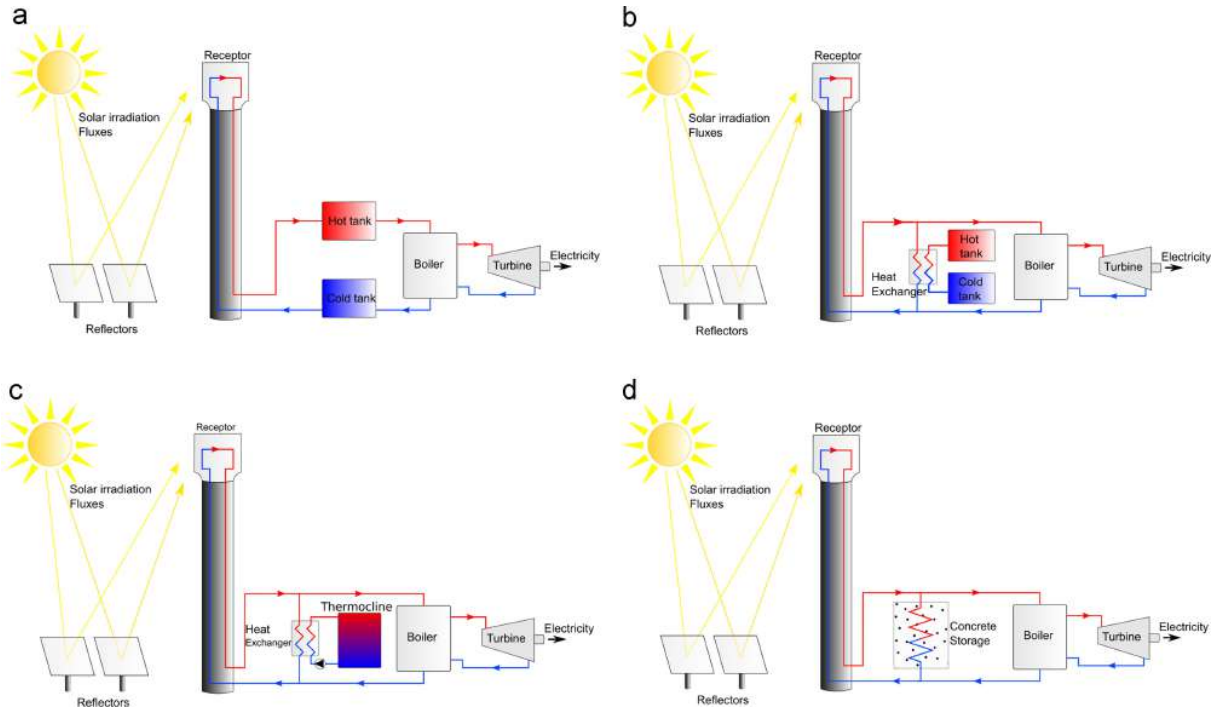

Source: Adapted from Pelay et al. (2017).
Note: (a) Two-tank direct; (b) two-tank indirect; (c) thermocline indirect; (d) passive.

2.4.2.1 Active storage

Active systems can be subdivided into direct and indirect regarding the TES integration on the facility.

In active direct systems, the HSM also serves as the HTF in the solar field. Thus, no heat exchanger between HTF and the HSM is required.

At TES charging, the HTF is stored in a hot tank, positioned at the exit of the solar field. Similarly, at discharge, the HTF in the hot tank is pumped through the power cycle and then stored in the cold tank [(11)] at the entrance of the solar field.

Using the same material eliminates the cost of having extra heat exchangers, potentially allowing the power block to be operated at higher temperatures, which positively impacts the system's thermodynamic efficiency. To date, the most commonly deployed concept relates to the direct molten-salt two-tank system, similar to the one shown in Figure 2.24. Another concept under this classification is the single-tank molten salt system, where hot and cold fluids are stored in the same tank (usually separated through a mechanical barrier). However, the latter has not been fully deployed. Despite potentially reducing costs, the tank and the barrier would be constantly exposed to severe thermal stresses under cycling operation, affecting its expected lifetime .

Contrary to active direct TES, in active indirect systems, an intermediate, different to the HSM is used as HTF, so they flow in independent circuits, implying that an additional heat exchange process is required. Active indirect TES systems in the form of the two-tank indirect molten salt system are the most deployed concept in CSP plants today.

At active indirect systems, the HTF and the HSM are different. Typical active indirect concepts are shown in Figure 2.24, with two separate tanks (Figure 2.24b) and one thermocline tank (Figure 2.24c) for storage. In the first, for TES charging, the HSM in the cold tank is pumped to the hot tank, passing through a heat exchanger. Then, during the discharge phase, the flow direction of the storage material is reversed to release the heat to the HTF. In this manner, hot and cold materials are separately stored.

An alternative to the two tanks concept is using a single tank, which combines the hot and cold tank into one storage volume and reduces capital costs. The hot HSM is stored on the top and the cold HSM on the bottom of the tank. They are separated due to temperature stratification, and the zone between the hot and cold fluids is called the thermocline. Usually, a filler material (e.g., quartzite rock, sand, concrete) is added to the tank to enhance the thermocline effect and reduce the needed amount of HSM. Therefore, it is about 35% cheaper than two tanks systems.

It works by pumping the hot fluid into the top of the tank, which gradually displaces the cold fluid at the bottom of the tank during charging mode. Thus, buoyancy effects preserve the thermal gradient that is created inside the tank. However, in practice, it is challenging to separate the hot and cold fluid. Therefore, the configuration of filler materials in the tank is undoubtedly a crucial aspect to be considered.

[(11)] Although it is called a cold tank, its temperature commonly far exceeds the ambient temperature

2.4.2.2 Passive storage

In passive systems, the TES media itself does not circulate. Instead, the storage contains a tubular heat exchanger integrated into the solid HSM, usually a solid (e.g., concrete, PCMs), forming a compact heat exchanging and storage unit (see Figure 2.24d). The HTF circulates to heat (charge) or cool down (discharge) the material kept inside the storage system.

The significant advantage is that this HSM is often inexpensive material, such as rocks, sand, or concrete (TEMLETT, 2018).

The high thermal conductivity and the excellent contact between the HSM and the tubes are crucial to enable high heat transfer rates. Nevertheless, the HTF temperature decreases during the discharging process as the TES cool down. This issue may be overcomed by using PCMs and thermochemical reactions, yet at the expense of lower heat transfer coefficients. Another potential disadvantage is concerning the thermal fatigue of the HSM, which can affect its lifetime (GUÉDEZ, 2016).

2.5 ENERGY DISPATCH STRATEGIES

When equipped with a TES system, the operation of a CSP plant can be performed in multiple ways, according to the enterprise objectives and techno-economic restrictions. IEA (2010) highlights four major operation strategies, aiming to attend: intermediate loads, delayed intermediate loads, baseloads, and peak load, as presented in Figure 2.25. Additionally, the integration of TES also enables additional revenue streams (i.e., ancillary services).

Figure 2.25 – Example of grid daily power demand

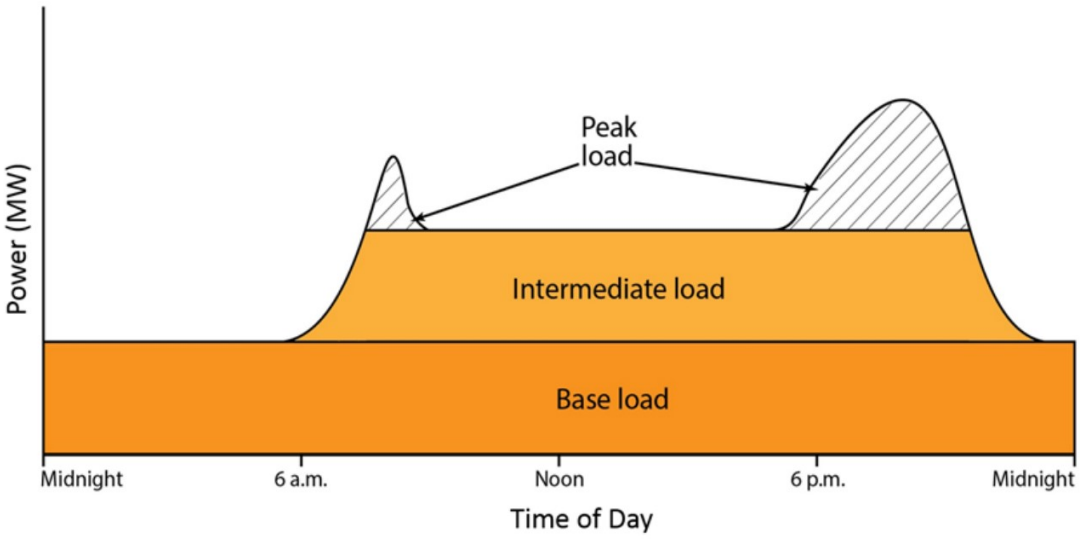

Source: Guédez (2016).

At the intermediate load plan (see Figure 2.26), the facility is designed to dispatch electricity when the sunshine coincides with peak and shoulder, represented by the intermediate load in Figure 2.25). Its optimal configurations only require a small amount of storage, mainly to smooth electricity production. Thus, it provides the most inexpensive investment costs electricity output.

Figure 2.26 – Intermediate load configuration

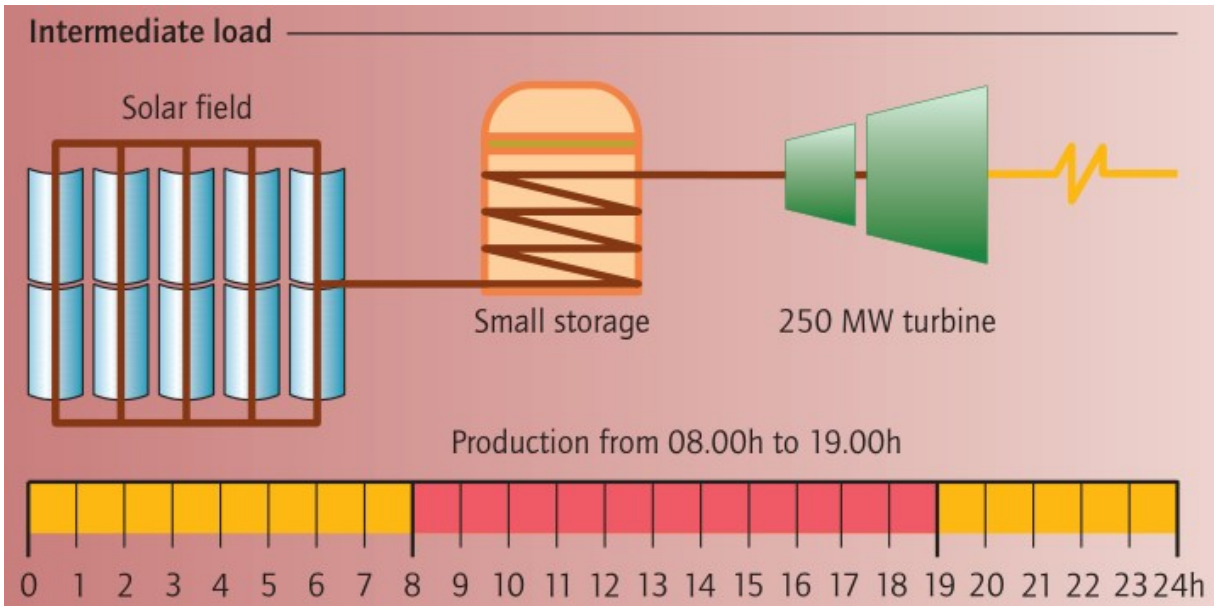

Source: IEA (2010).

The delayed intermediate load configuration (see Figure 2.27) provides a higher offset between heat absorption and electricity dispatch. At this configuration, the plant collects solar energy all day but dispatches electricity from noon until after sunset, attending to peak and shoulder loads. Because of that, it requires an enormous amount of storage.

The baseload configuration (see Figure 2.28) runs the plants continuously for most of the year, at the expense of enormous storage capacities. When relying on cheap storage capacity, electricity from the baseload plant is slightly cheaper than the delayed intermediate load plant. In addition, higher HSM temperatures allow for less expensive storage but require more sophisticated and costly materials.

Lastly, the peak load plan (see Figure 2.29) is designed to provide electricity solely to meet peak loads. Therefore, it requires a large amount of storage and power block capacity. As a result, it produces the lowest CF and the most expensive energy of all four designs. Although, it dispatches it when the highest revenue prices occur.

Another alternative is to optimize the plant's dispatch, aiming to maximize parameters such as generation, revenue, or the plant's CF. A study of this kind is performed

Figure 2.27 – Delayed intermediate load configuration

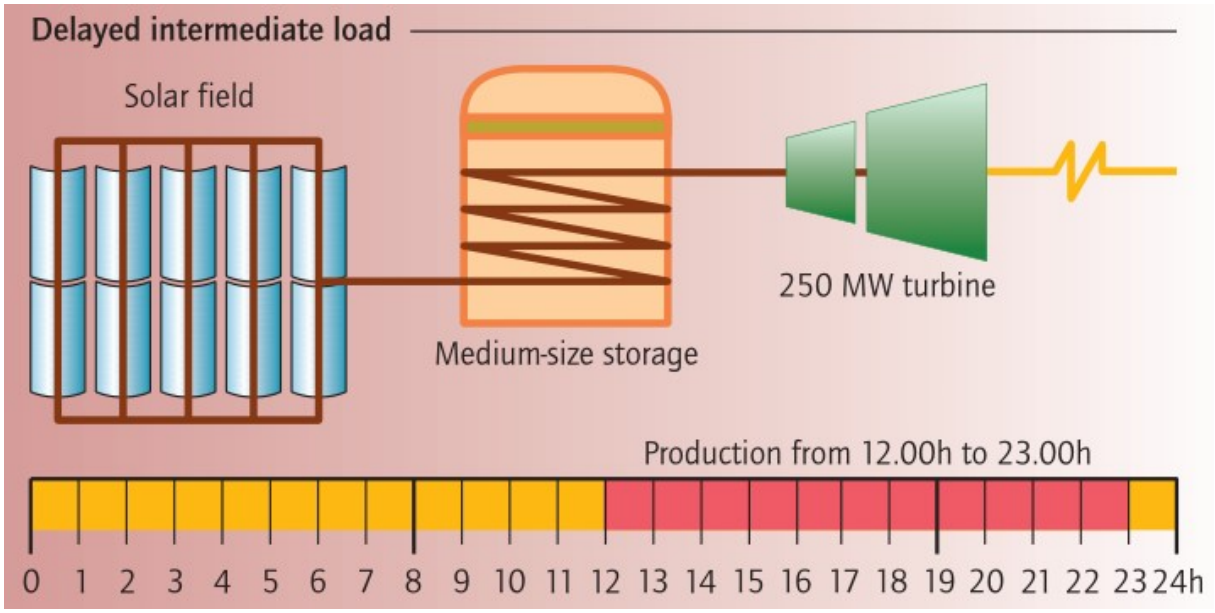

Source: IEA (2010)

Figure 2.28 – Base load configuration

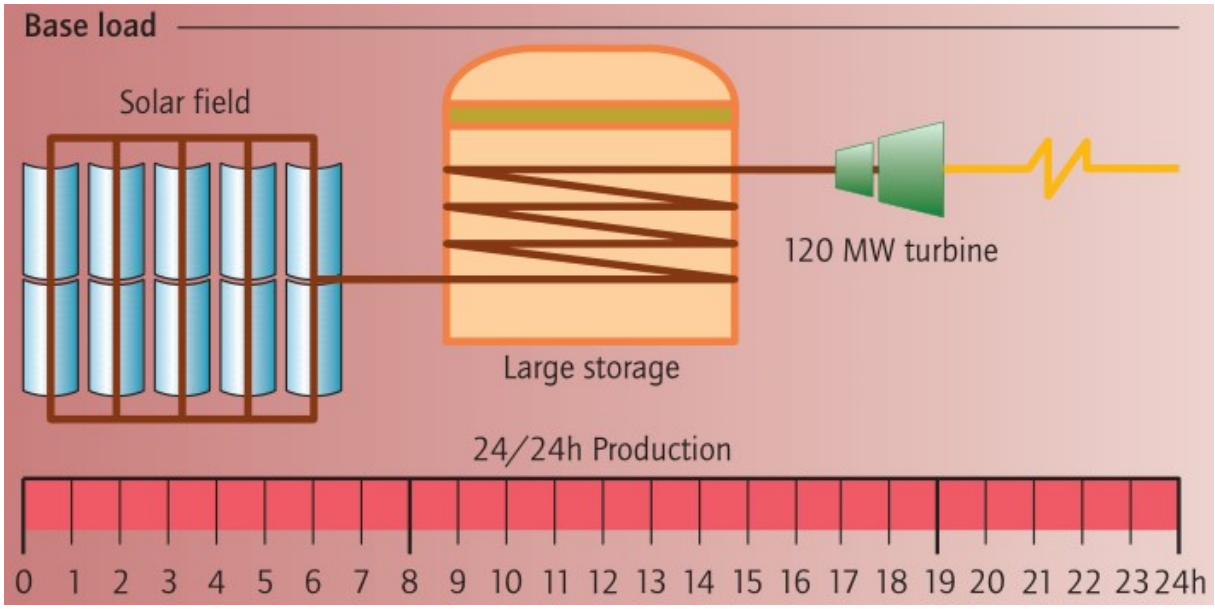

Source: IEA (2010)

by Petrollese et al. (2017).

2.6 POWER CYCLE

The Rankine cycle is the basic building block of vapor power plants. The components of four alternative vapor power plant configurations are shown schematically in Figure 2.30. It divides the plant into four subsystems identified from (A) through (D).

The function of subsystem (A) is to supply the energy to heat the power block

Figure 2.29 – Peak load configuration

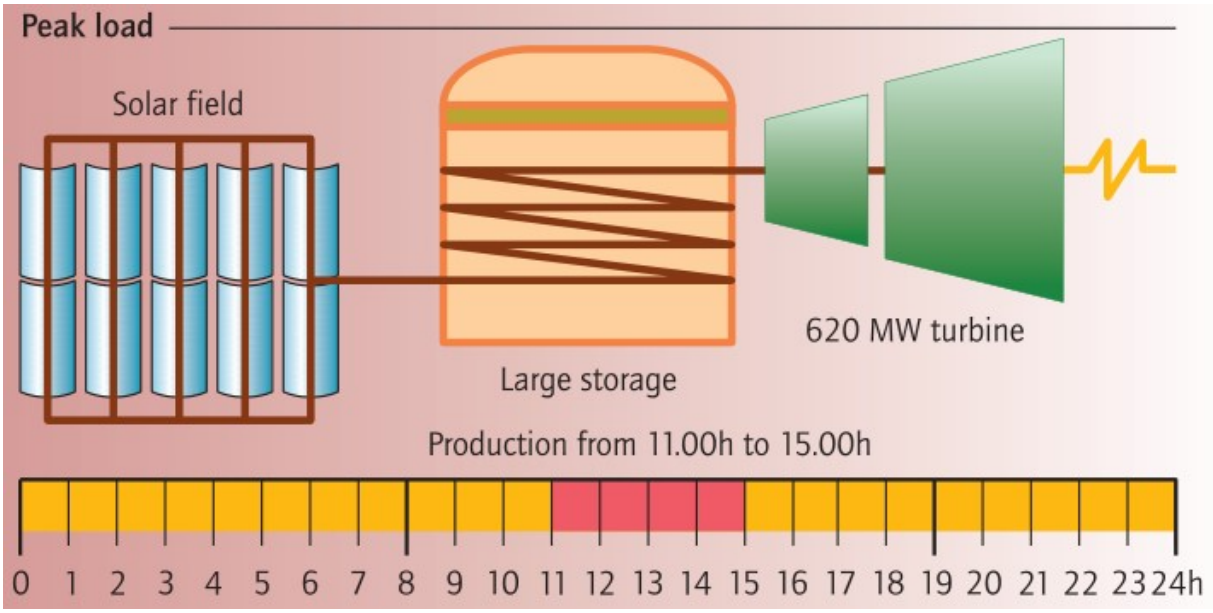

Source: IEA (2010)

working fluid into the vapor required by the turbine of subsystem (B). In that subsystem is where the energy conversion from heat to work occurs. Each particle of the working fluid periodically undergoes a thermodynamic cycle as it circulates through the series of interconnected components. That is the Rankine cycle (MORAN; SHAPIRO, 2014).

In those systems, regardless of the energy source, the vapor produced passes through the turbine, expanding to lower pressure, developing power. Next, the turbine power shaft is connected to an electric generator – subsystem (C). Finally, the turbine's vapor passes through the condenser, condensing outside tubes carrying cooling water – subsystem (D) (MORAN; SHAPIRO, 2014).

The primary distinction between that power plant configurations to a CSP facility is the method used in subsystem (A) to produce steam. In fossil-fueled plants, the working fluid vaporization is accomplished by heat transfer from fuels combustion to water. This method is present in facilities fueled by biomass, coal, biomass, and municipal waste (MORAN; SHAPIRO, 2014).

Distinctly, solar thermal power plants have receivers for collecting and concentrating solar radiation. In addition, the heated HTF provides the energy required to vaporize water flowing in the other stream of the heat exchanger, which is provided to the steam turbine. Therefore, the thermal analysis of solar power plants is similar to that of any other plant, and the same thermodynamic relations are applied (MORAN; SHAPIRO, 2014).

Moreover, concentrating collectors and conventional boilers are present in hybrid plants, running on solar radiation or fuels whenever needed.

Figure 2.31 shows the basic Rankine cycle, and its T-s diagram. Considering

Figure 2.30 – Sensible thermal energy storage systems

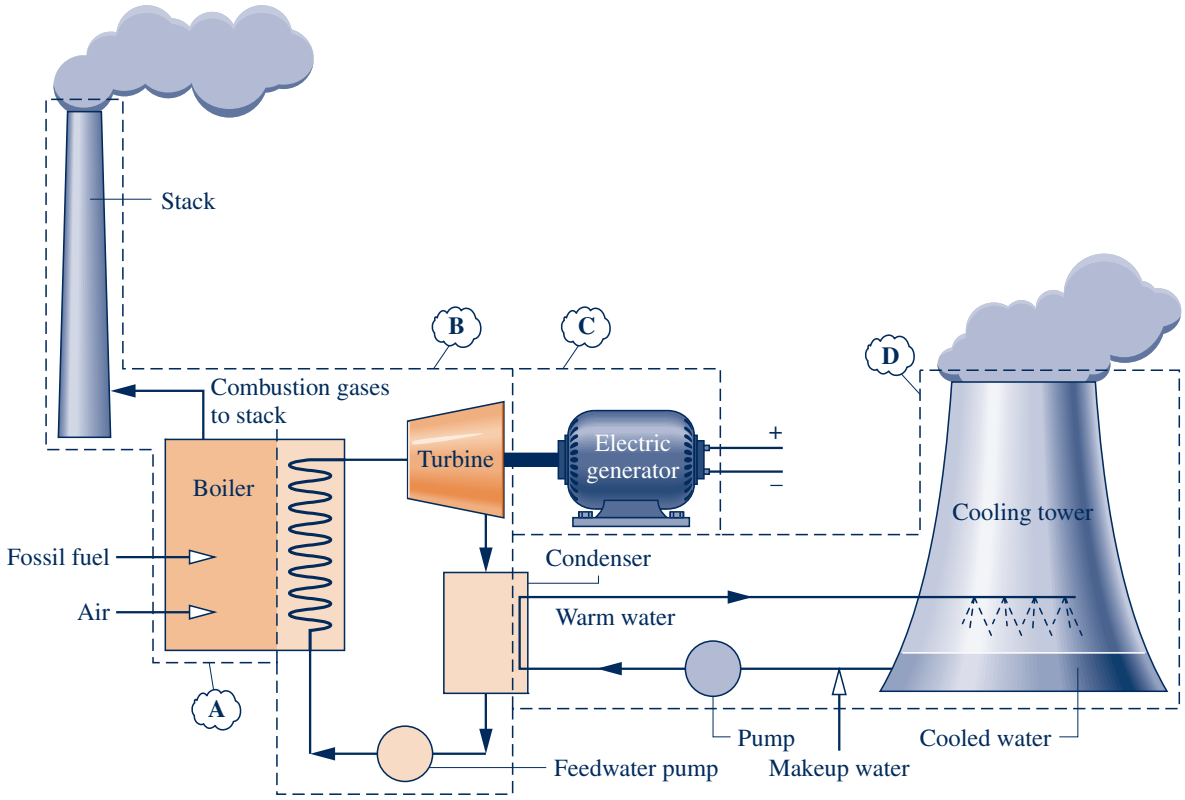

(*a*) Fossil-fueled vapor power plant.

Source: Moran and Shapiro (2014).

the system's inefficiencies, the actual pumping process is 1-2', and the actual turbine expansion process is 3-4'.

The cycle net work output (W), heat input (Q), pumping work ($W_{12'}$), and efficiency (η) are calculated as follows:

$$\frac{W}{m} = (h_3 - h_{4'}) - (h_{2'} - h_1) \tag{2.7}$$

$$\frac{Q}{m} = (h_3 - h_{4'}) \tag{2.8}$$

$$\frac{W_{12'}}{m} = (h_{2'} - h_1) = \frac{v(P_2 - P_1)}{\eta_{pb}} \tag{2.9}$$

$$\eta = \frac{W}{Q} = \frac{(h_3 - h_{4'}) - (h_{2'} - h_1)}{(h_3 - h_{2'})} \tag{2.10}$$

where h is specific enthalpy; v is specific volume; and P is pressure.

Figure 2.31 – Basic Rankine power plant cycle

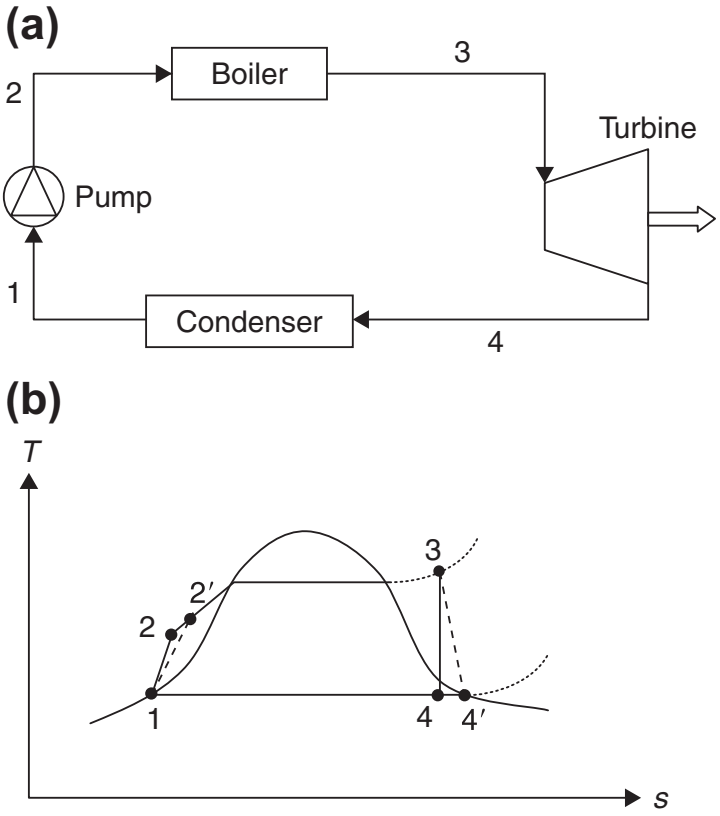

Source: Kalogirou (2004).
Note: (a) schematic; (b) T-s diagram.

2.6.1 Reheat cycle

Generally, the efficiency of a Rankine cycle can be improved by increasing the pressure in the boiler. So, in reheat cycles, the expansion takes place in two turbines (MORAN; SHAPIRO, 2014). This process is shown in Figure 2.32.

First, the steam expands in the high-pressure turbine to some intermediate pressure, then passes back to the boiler. Then, it is reheated at constant pressure to a temperature usually equal to the original superheater outlet temperature. Finally, the reheated steam is directed to the low-pressure turbine, expanding until the condenser pressure is reached (MORAN; SHAPIRO, 2014).

The reheat cycle efficiency is given by

$$\eta = \frac{(h_3 - h_{4'}) + (h_5 - h_{6'}) - (h_{2'} - h_1)}{(h_3 - h_{2'}) + (h_5 - h_{4'})} \tag{2.11}$$

2.6.2 Regenerative cycle

In a simple Rankine cycle, the efficiency is much less than the Carnot efficiency, as part of the heat supplied is lost due to irreversibility. However, if some means could be found to transfer this heat reversibly from the working fluid in another part of the cycle,

Figure 2.32 – Reheat Rankine power plant cycle

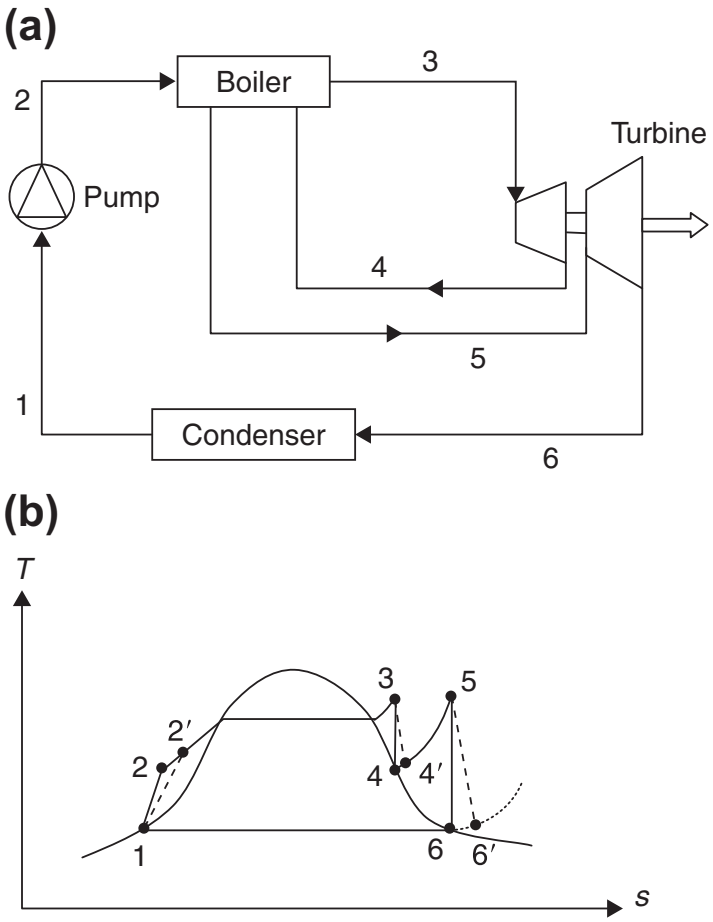

Source: Kalogirou (2004).
Note: (a) schematic; (b) T-s diagram.

all the heat supplied would be transferred at superior temperatures, and efficiencies closer to the Carnot efficiency could be reached (MORAN; SHAPIRO, 2014). The cycle where this technique is used is called a regenerative cycle, as presented in Figure 2.33.

In that cycle, steam is extracted at various points in the turbine. It is then directed to feedwater preheaters and mixed with the condensed water. In that regenerative process with just one extraction point the total steam flow rate is expanded to an intermediate point 6, where a fraction (*f*), is bled off and taken to a feedwater heater; the remaining (1-*f*) is expanded to the condenser pressure and leaves the turbine at point 7.

After condensation to state 1, the (1-*f*) water is compressed in the first feed pump to the extraction point 6. It is then mixed in the feedwater preheater with the extracted steam in state 6, and the total flow rate of the mixture leaves the heater in state three and is pumped to the boiler, 4. Thus, the regenerative cycle efficiency is given by

$$\eta = \frac{(h_5 - h_6) + (1-f)(h_6 - h_7) - (1-f)(h_2 - h_1) - (h_4 - h_3)}{(h_5 - h_4)} \tag{2.12}$$

where *f* is the fraction of steam in the turbine bled at state 6 to mix with the feedwater.

Figure 2.33 – Rankine power plant cycle with regeneration

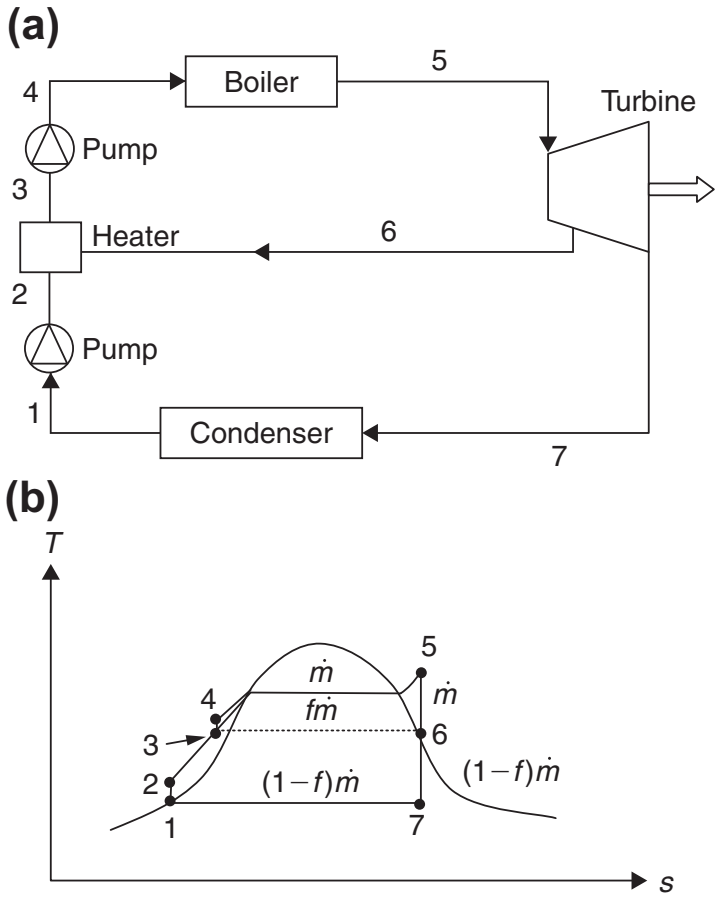

Source: Kalogirou (2004).
Note: (a) schematic; (b) T-s diagram.

Although one feedwater heater is shown in Figure 2.33, many of them can be used; the exact number depends on the steam conditions. However, because this is associated with additional cost, their number and the proper extraction pressures require careful calculations.

2.7 THERMAL POWER SYSTEMS SIMULATION

The first simulation program for thermal power plants dates back to the 1960s. In the following decade, a method was developed in which a water-steam circuit was solved numerically, constructed using individual components connected through streams. Then, it was systematized in code so computers could interpret the entire circuit. Since then, this workflow has been widely maintained.

Modern simulation programs combine a graphical user interface with detailed flow, thermodynamics, and heat transfer models. These calculations greatly facilitate the assessment of new plant design, process modifications, existing plant retrofitting, plant optimization, plant security and safety, operating behavior at base loads, off-design loads, start-up and shutdown procedures, and operating behavior during malfunctions.

The physical background of these programs is based on the conservation of mass, energy, and momentum. Therefore, the complexity of these equations and the required method for a numerical solution depend on whether the flow problem is steady-state, quasi-steady, or dynamic.

Steady-state simulation. The time derivatives are eliminated from the conservation equations. *Quasi-dynamic simulation*. The time derivative of specific components is not relevant. It can be neglected in the conservation equations, which in return simplifies the system of equations significantly. *Dynamic simulation*. The time derivatives must be taken into consideration.

Secondly, they also depend on the dimension of the flow model.

Dimensionless. The local discretization is not considered, so the modeling of thermal power plant components such as heat exchanger, pump, condenser, turbine results in equation systems with the inputs and output parameters of the components (pressure, enthalpy, mass flow rate, and concentration); *One-dimensional*. The plant components are discretized between their inlet and outlet, and the flow in finite objects, resulting in a numerical grid. Then, algebraic equations approximate the partial differential equations obtained. Finally, the state variables such as temperature, enthalpy, and pressure at each discrete coordinate can be determined; *Two or three-dimensional*. Spatial discretization is required for the different coordinates, resulting in detailed and computationally expensive calculations.

In many practical engineering applications, dimensionless modeling and the assessment of the steady-state operation of components is sufficient. Design calculations at different loads are also conducted with such steady-state simulation models.

In contrast, dynamic simulation allows investigation into the transient behavior of the entire power plant. Therefore, an adequate description of automation structures and control devices is essential to obtain an accurate response. Despite that, the programming effort and computational time are considerably higher than steady-state calculations.

2.7.1 Solar thermal power systems

Ideally, a CSP plant operates at a steady-state design load. However, it is also required to operate on off-design load conditions due to solar radiation fluctuations and energy supply and demand.

Their operating flexibility is an essential factor for reliable grid stability and eco-

nomic operation. So quasi-dynamic and dynamic simulations offer an effective tool for optimizing the power plant performance and control structures and assessing capabilities and limitations of the system about process, materials, emissions, or economics. Additionally, thermoeconomic optimizations at different base loads and off-design load conditions are often necessary, requiring both the model accuracy and efficiency of the numerical solver to design competitive facilities.

Dynamic simulation of CSP plants is conducted as the technology relies on DNI, which is naturally variable. Cloudiness, solar angles, daytime and season, and the plant's geographic location influence the amount of energy that can be collected. Dynamic simulations aim to study the performance of CSP plants under different solar irradiance conditions, also regarding procedures such as plant start-up and TES operation.

According to Alobaid et al. (2017), two types of studies can be distinguished, either performing simulations based on half to one-hour timesteps and treating most thermal components as quasi-dynamic, or based on shorter timesteps, which attempt to track short duration cloud and thermal transients using more fundamental approaches. Critical inputs for system performance forecasting include DNI time-series data, combined with the local ambient temperature, humidity, and wind speed. Commercial software for energy system modeling used in solar thermal applications includes SAM, Greenius, OpenModelica, EBSILON Professional, and TRNSYS. A detailed overview of codes applicable to CSP technologies is given in Ho (2008).

A free, closed-source package used for the pre-design of CSP plants is the SAM from the National Renewable Energy Laboratory (NREL), based on the TRNSYS simulation engine. It incorporates economic and energetic hourly simulations of renewable energy technologies. SAM is freely available and accounts for a user-friendly graphical interface and a detailed economic model as its principal advantage. Additionally, it presents a parametric analysis toolbox to perform simultaneously parametric studies about design parameters. Despite that, as one of its main disadvantages, it only accounts for limited CSP plant layouts, thus making it complex to use for evaluating new concepts and hybrid schemes. For example, the combined use of a PTC solar field with a D2T TES is not predicted for the software, yet it is investigated in the paper by Lopes et al. (2021).

Another free tool used for the analysis of CSP plants is the Green Energy System Analyses Tool (Greenius) developed by the German Aerospace Center (DLR) (DLR, 2018). It presents a similar workflow to SAM, only allowing rigid plant layouts. It offers a combination of fast technical and economic calculations and comes with an interface. The main disadvantages are similar to those of SAM, these being the impracticality to develop new models. Moreover, it allows lesser personalized simulations and does not incorporate optimization models. Furthermore, integrating new components is not

possible, and the solar field-related component technical and economic models are less detailed than in SAM.

SolarTherm is a simulation tool for evaluating and optimizing novel CSP system designs, offering an easy and highly flexible alternative to the conventional tools. It is built in the object-oriented Modelica language (Modelica Association, 2017), and it can be edited and run in a user-friendly graphical environment such as Dymola (Dassault Systèmes, 2019) or OMEdit (Open Source Modelica Consortium, 2019). It allows the modeling and simulation of complex physical systems with mechanical and control components. Modelica has been extensively used to model and simulate CSP components and systems, and all aspects of the model and solver are visible and can be modified. However, these advantages come at the expense of more intricate component settings and modeling. Examples of recent publications can be found in the study by Calle et al. (2020).

Many providers of design software for power plants have begun to include CSP plant components in their tools. For example, this is the case of EBSILON Professional which provides specialized component libraries for steady-state and time-dependent simulation jointly developed with the DLR. Such a program was used by Ferreira (2018), who studied a CSP-LFR-DSG plant with a sensible-latent storage system. Figures 3.2-3.5 shows examples of CSP plant topologies modeled in this program. STEAG (2021) presents details about the physical modeling of crucial components.

Several studies have been performed dealing with the optimization of TES integration and operation in existing CSP plants. In most of them, the main power plant blocks are modeled for a given CSP plant layout or to simultaneously represent multiple power plants technologies. Sensitive analysis of critical design parameters instead of optimization algorithms is used to identify best configurations from quantifying key specific performance indicators, such as the LCOE. The outcome from these studies has helped the research community to understand that there exists an interrelation between the desired operation and the optimum solar field, power block, and TES sizes, and despite increasing the investment, TES can lower the LCOE (GUÉDEZ, 2016; TEMLETT, 2018).

2.8 THERMOECONOMIC ANALYSYS

Thermoeconomics considers the interrelations among energy, economy, and ecology, bringing some fundamental inputs in process design, evaluation, and maintenance. Thermodynamic formulations imply using scarce resources and comparing energy and exergy conservation between different processes, which is fundamental for energy policy discussions. Thermal systems involve significant work and heat interactions with their surroundings and appear in almost every industrial plant. Such considerations may have a positive impact on sustainable development and environ-

mental protection (DEMIREL; GERBAUD, 2019).

One of the main goals of thermoeconomic analysis is understanding the system's cost structure of the system products and thus introducing criteria and indicators for system design improvement. The economic evaluation of power generation resources can be performed based on several key parameters, such as simple or discounted payback, investment IRR, NPV and the LCOE, being the latter the most widely used.

2.8.1 Levelized cost of energy

The LCOE is the principal tool for comparing plant unit costs of different technologies over their lifetimes. LCOE is closer to the costs of electricity production in regulated electricity markets with stable tariffs, for which it was developed than to the variable prices in deregulated markets. Thus, it is broadly considered in studies by organizations such as the International Renewable Energy Agency, the Brazilian Energy Research Office, the USA Energy Information Administration, among many others for conducting technical-comparative analysis.

By definition, a good way of looking at LCOE is considering the electricity tariff at which an investor would precisely break even after paying the costs incurred over the facility's lifetime. It is based on the assumptions that the discount rate and electricity tariff are stable during the project's lifetime, while in practice they are most likely to vary.

Another feature of LCOE is that it allows different technologies to be compared with different scales of operation, periods of investment and operating time, or even both. Thus, for example, it can be used to compare the cost of power generated by a renewable resource with a fossil-fueled generating unit or even to make comparisons between different renewable. As an example, one can cite the study by Astariz et al. (2015), which evaluated the different possibilities of harnessing energy in the marine environment, using LCOE to perform an economic analysis of offshore wind, tidal, and wave energy ventures. Another example is the study by Ouyang and Lin (2014), which estimated the LCOE for many renewable sources in China to define the government policies needed to increase their competitiveness against fossil fuels.

In addition, relative variations in the LCOE of one generation technology compared to another can be used as a measure of technological progress, as can be observed in Figure 1.8a, and usually reflect reductions in costs due to favorable financial policies, scale gains, reduction in manufacturing costs, and learning curve IRENA (2019).

There are multiple forms to perform its calculation, used in specific contexts. However, they all fundamentally regard the CAPEX and OPEX, leveled by the energy. Following it is presented the definition by BEIS, as described by Aldersey-Williams and Rubert (2019).

$$LCOE = \frac{\sum_{t=0}^{n}(CAPEX + OPEX_t)(1+r)^{-t}}{\sum_{t=1}^{n} E_t(1+r)^{-t}} \tag{2.13}$$

in which *CAPEX* is the annual capital costs; *OPEX* is aggregate of fuel, carbon, insurance, fixed and variable annual operational costs; E_t is the annual net electricity output; r the annual discount rate; and n the system lifetime, in years.

In the past, the technology with the lowest LCOE was also the best baseload investment choice, yet it is no longer valid; structural changes in demand and supply, in particular with the mass deployment of renewables with zero short-run marginal costs, challenge the notion of baseload production itself.

In fact, with the prospect of greater penetration of intermittent renewable sources, there is currently a concern in developing more appropriate metrics capable of weighing the benefits of each technology (EPE, 2018), such as the VALCOE and the LCOS, as presented in the reports by IEA (2020, 2021) and the studies by Pawel (2014), Jülch (2016) and Schmidt et al. (2019), respectively. As a result, a technology's actual economic cost will now depend on its overall share and technical characteristics and all other technologies' costs and technical characteristics in the grid rather than only on the discounted sum of its investment costs and variable costs at the plant level.

Nevertheless, despite those limitations, LCOE has maintained its appeal. It remains a straightforward, transparent, comparable, and well-understood metric, while to date, these other metrics still not largely adopted by technical and scientific studies. Thus, while there is an increasing need to complement it with the other metrics, it retains its fundamental usefulness as a widely used tool for modeling policymaking and public debate.

2.9 CHAPTER CONCLUSIONS

This chapter aims to present concepts that permeate CSP, such as solar collectors, thermal energy storage, and the Rankine cycle, to introduce the reader to the environment in which this study is inserted. Based on the information presented, it can be said that energy storage systems have played and will play an increasingly important role in society, especially in facilitating the decarbonization of energy generation and consumption processes.

Such systems are well integrated with CSP plants, especially in energy storage in the form of heat. Therefore this technology can play an essential role in the energy transition by enabling a more predictable and stable energy supply.

Among the current trends for this technology, there is greater use of CSP-PTC plants combined with sensible heat storage systems in I2T arrangement, with molten salt as HSM; because of this, this configuration was called conventional in this work.

For the future, a notable development of SPT technology is also anticipated, and the use of DSG and DMS solar field configurations. The latter, coupled with the conventional configuration, presents a high potential for CSP cost reduction, which has been addressed with great emphasis in this paper.

3 PLANTS MODELING AND SIMULATION

This chapter describes the main procedures implemented throughout this study to enable the modeling and simulation of CSP plants and their comparison on a thermodynamic and economic basis. The main procedures followed are summarized in Table 3.1 and are subsequently described.

Table 3.1 – Summary of the main procedures followed

Step	Title	Procedure	Output
1	Power block sizing	Estimate of the main parameters of the power block. For that it was used the design point method (WANG, 2019) as well as the SolarPACES (2021) database	Power block net and gross capacities and demanded thermal power, in design conditions
2	Thermal energy storage sizing	Estimate of the main parameters of the TES. It was used the design point method	Required HSM mass flow rate in heat exchangers an the total mass of fluid in the hot and cold tanks
3	Solar field sizing	Estimate of the main parameters of the solar field. For that it was used the design point method as well as the PTC's characteristic curve	Power block net and gross capacities and demanded thermal power, in design conditions
4	Plant modeling	EBSILON Professional was used for modeling plants in four distinct configurations, aiming to compare their performance under a typical year of operation. The ambient EBScript was used to handle the information flow of the facility in each of the timesteps of the simulations	Four topologies for representing the analysed plant configurations explored in this study, with a operation emulating real CSP-PTC facilities
5	Parametric analysis	Proceed a parametric analysis varying two of the most important facility's input metrics, the SM and the storage capacity	Assessment of these parameters' influence in the plant behavior
6	Best performing designs analysis	Identify the combinations of parameters in sensitive analysis which result the most economically competitive facilities	Performance of the most competitive configurations for each configuration

Source: Elaborated by the author.

- *Power block sizing*. The first step for modeling the power plants consists of defining the power block rated power. In this study, they were chosen to represent the scale of the most current CSP-PTC enterprises (under operation and development), based on the SolarPACES (2021) database;
- *Thermal energy storage sizing*. Afterward, the HSM mass in the TES can be obtained. At night or throughout overcast sky conditions, the TES provides the power block heat input. At this condition, the HSM mass flow out of the hot storage tank was estimated, providing the total mass of HSM to be held;
- *Solar field sizing*. The following step is to estimate the collector field area required to provide the heat for the power cycle. For that, this study follows the design point method, described by Wang (2019). According to it, the facility nameplate parameters are obtained considering steady-state conditions. Hence, the thermal power absorbed at the solar field matches the rated power required to run the steam turbine and store a predetermined surplus for later use. The meteorological conditions, mainly the instantaneous DNI and solar position, are provided by a representative date and time. Other inputs, like the ambient air temperature and the wind speed, are calculated based on the TMY;
- *Plant modeling*. Besides defining the plant mentioned above parameters, it is also crucial to ensure its operation strategy follows those in commercial stations. For this purpose, algorithms were elaborated to command off-design system operation, mainly to command the HTF temperature and the TES charge and discharge cycles;
- *Parametric analysis*. Once the design conditions and the operation strategy are defined, the topologies under the scope of this work were modeled and simulated using EBSILON Professional. A parametric analysis was performed, varying the solar field size (SM) and the storage capacity, aiming to obtain the design combinations with the lowest LCOE for each topology, so ensuring a fair comparison between them;
- *Best performing designs*. Lastly, a wide range of results was obtained from the parametric analyses for the various independent parameter combinations. The most competitive plants (i.e., with the lowest LCOE) were selected and further analyzed under technical and economic perspectives.

Four PTC concepts were examined, including different HTFs and the use or not of STES. Among the software available for this purpose, EBSILON Professional stands out due to the possibility to perform complex and customizable, and the presence of specific modules for solar thermal plants simulation, developed by the German Aerospace Center (DLR) in association with STEAG Energy Services GmbH.

The layout of the modeled plants was based on the Andasol-1 project in Guadix, Spain, since it is widely described in the literature, such as the study by NREL (2013). It was the first commercial CSP-PTC power plant in Europe, operating since March 2009. Table 3.2 presents its main characteristics. The 50 MW_e plant is composed of a PTC running on thermal oil and a I2T molten salt TES using molten salts. The Rankine cycle design (see Figure 3.1) presents one high-pressure and four low-pressure vapor extractions. Its main characteristics are presented in Table 3.2.

Figure 3.1 – Scheme of the Andasol-1 facility

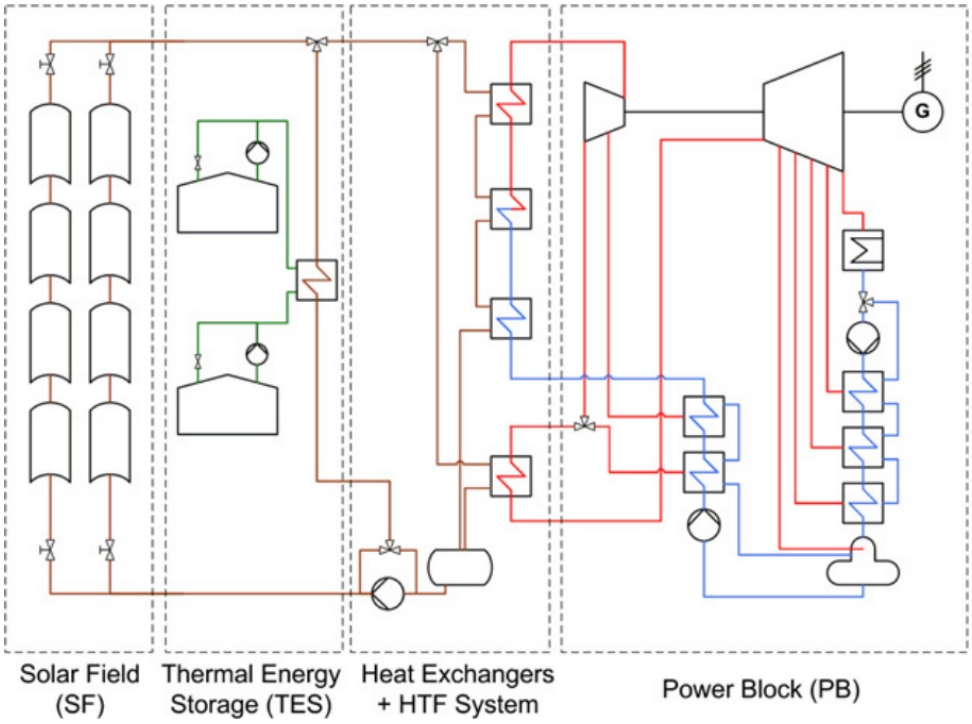

Source: Feldhoff et al. (2012).

It was decided to investigate two important solar field configurations compatible with different commercial forms of STES, I2T and D2T. They were also analyzed by running without storage capacity. Consequently, the modeling was separated into four plant topologies, as described below:

- *Topology (i)*. CSP-PTC synthetic oil-based solar field and a I2T molten salt TES;
- *Topology (ii)*. CSP-PTC synthetic oil-based solar field without TES;
- *Topology (iii)*. CSP-PTC in a DMS configuration and a I2T molten salt TES;
- *Topology (iv)*. CSP-PTC in a DMS configuration without TES.

Another important TES configuration is the ITC. Although the EBSILON component 145, called stratified storage, approximates its behavior, the direct modeling in

Table 3.2 – Nameplate characteristics of the Andasol-1 project

Parameter	Value	Unit
Solar field		
Field net aperture area	0.51	km^2
Direct normal irradiance at design	700	W m^{-2}
Heat transfer fluid	Dowtherm A	–
Design loop outlet temperature	393	℃
Number of solar collector assemblies per loop	4	–
Solar collector assembly model	EuroTrough ET150	–
Receiver	Solel UVAC 3	–
Storage		
Full load hours of TES	7.5	h
Tank height	14	m
Hot tank mass capacity	28.500	t
Cold tank mass capacity	28.500	t
Backup		
Fossil dispatch mode	Supplementary	–
Auxiliary heater outlet temperature	393	℃
Power block		
Design gross output	55	MW
Design net output	50	MW
Power cycle inlet pressure	100	bar
Annual power output	158	GWh
Number of vapor extractions*	6	–
Rated cycle conversion efficiency	38.1	%
Solar fraction	88	%
Year-to-year decline in output	0.5	%

Source: Data from NREL (2013) and STEAG (2020).

Note: *The vapor extractions are piped to: (1) a high pressure feed water at 40 bar; (2) a high pressure feed water preheater and the reheater at 17 bar; (3) the deaerator at 6 bar; (4) a low pressure feed water at 2.5 bar; (5) a low pressure feed water at 1.2 bar; (6) a low pressure feed water at 0.6 bar.

EBSILON Professional was not achieved. In the study by Klasing et al. (2018), such a system was modeled from EBSILON macros by describing the component physical behavior. However, for simplification, it was decided not to include it in the scope of this work.

Despite topologies (i) and (iii) present TES systems, additional considerations were performed to test them in special circumstances without TES capacity, (ii) and (iv) performed for comparison reasons. Nevertheless, because of their similarities, they will sometimes be treated together in this text: topologies (i) and (ii) referred to as synthetic oil-based solar fields; (iii) and (iv) as molten salt-based solar fields. The resultant model using EBSILON Professional components for each topology can be observed in Figures 3.2 to 3.5. The details of the design adopted for its dimensioning are treated in the following sections.

Figure 3.2 – Scheme of topology (i)

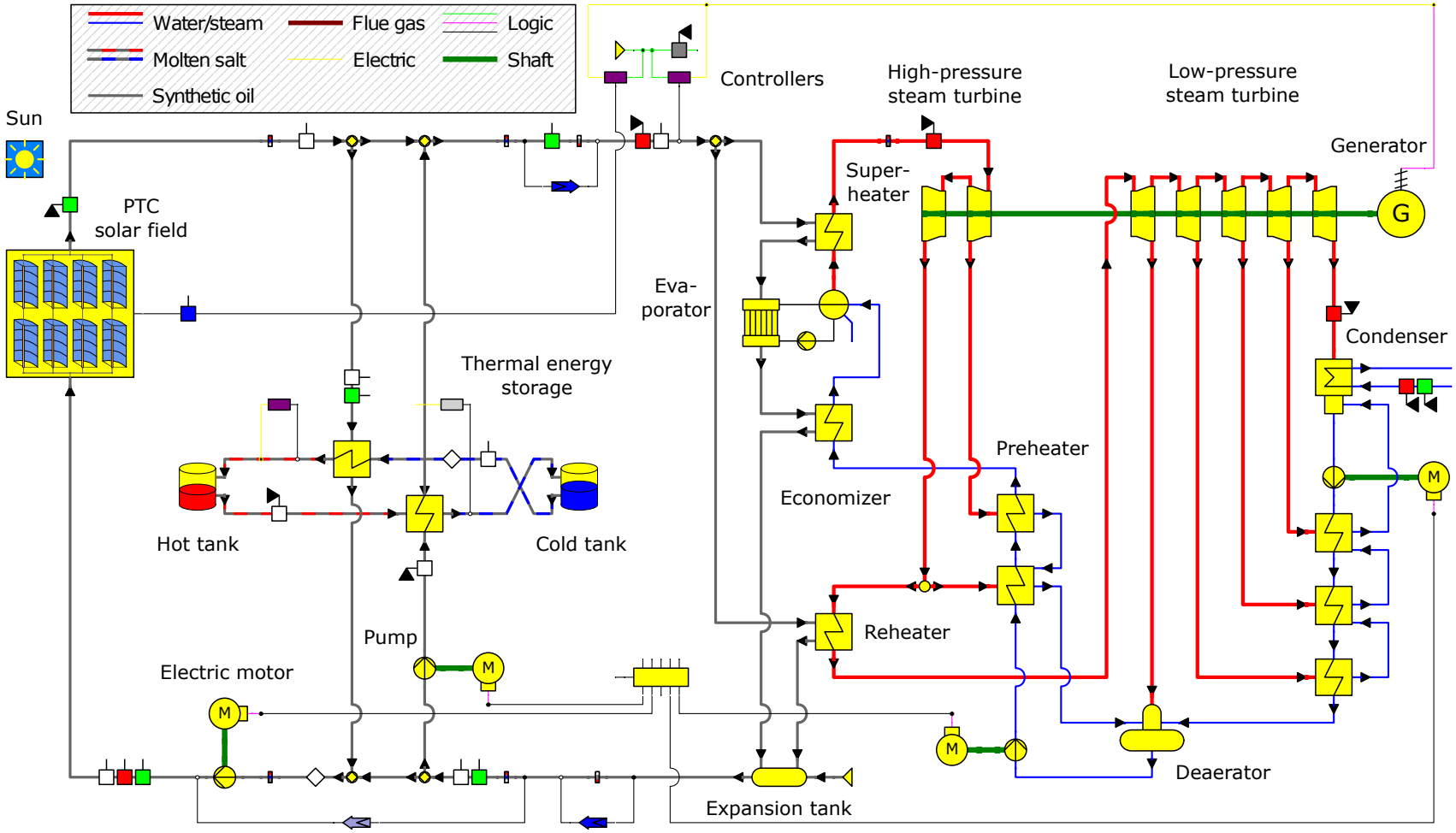

Source: Elaborated using EBSILON Professional (STEAG, 2020).
Note: This topology represents a CSP-PTC plant with thermal oil as HTF at the solar field, and a I2T molten salt TES.

Figure 3.3 – Scheme of topology (ii)

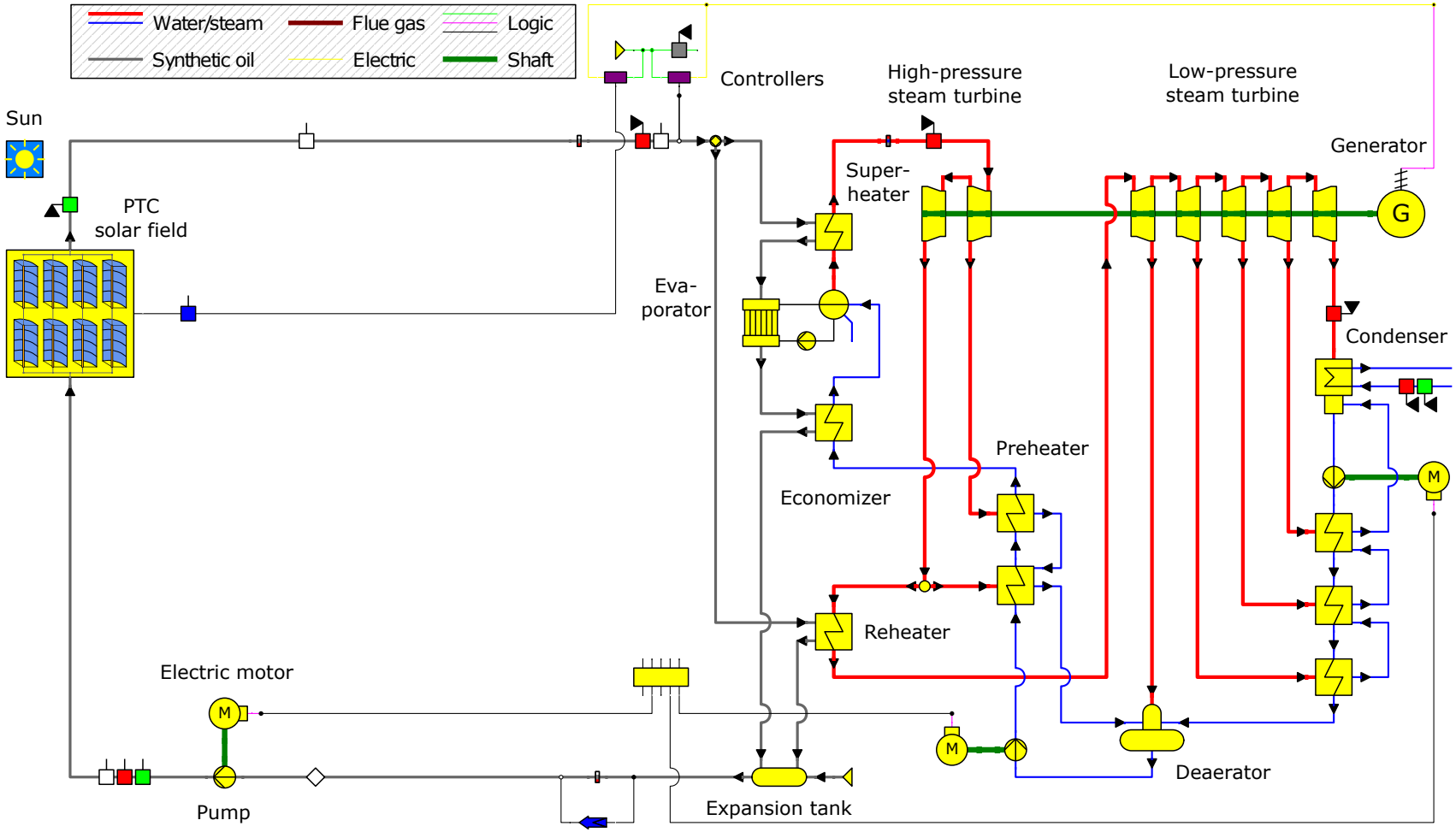

Source: Elaborated using EBSILON Professional (STEAG, 2020).
Note: This topology represents a CSP-PTC plant without storage and with thermal oil as HTF at the solar field.

Figure 3.4 – Scheme of Topology (iii)

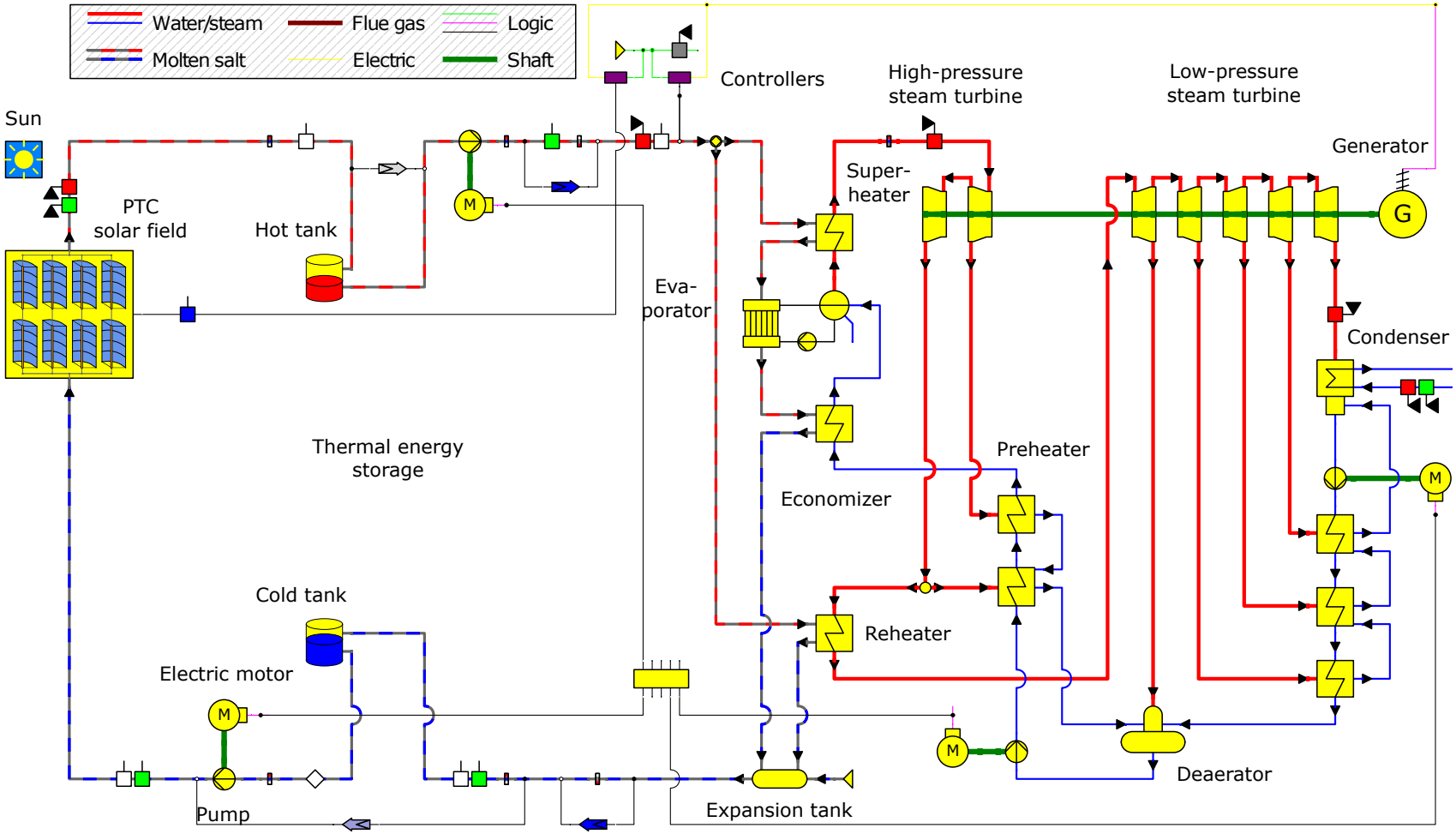

Source: Elaborated using EBSILON Professional (STEAG, 2020).
Note: This topology represents a CSP-PTC plant with molten salt both as HTF and HSM, with a I2T TES.

Figure 3.5 – Scheme of Topology (iv)

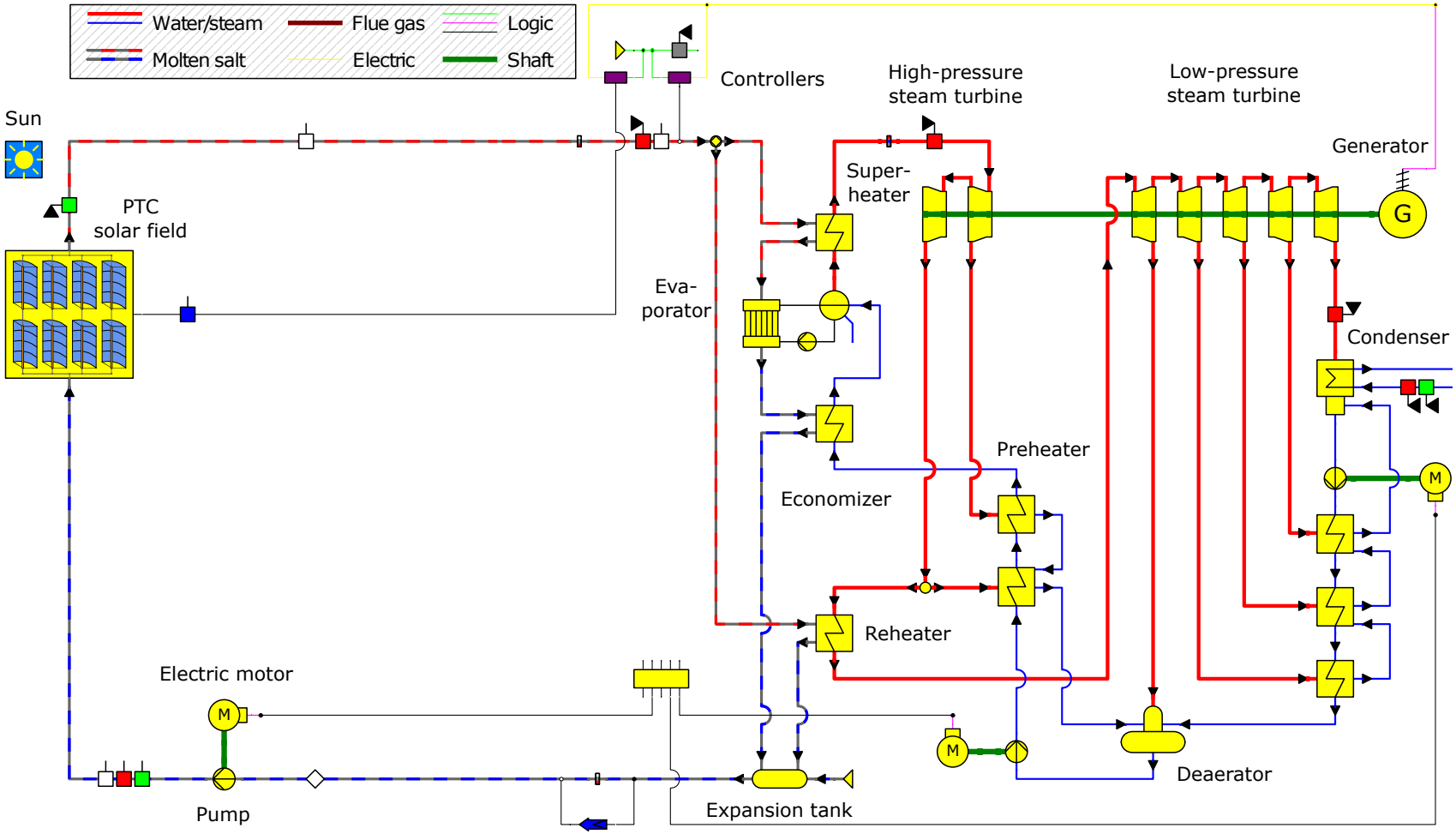

Source: Elaborated using EBSILON Professional (STEAG, 2020).
Note: This topology represents a CSP-PTC plant without storage and with molten salt as HTF at the solar field.

3.1 SIMPLIFICATION HYPOTHESIS

A series of assumptions were made to simplify these systems' modeling and simulation, which may or may not significantly influence the results obtained. They are summed up below:

- *Neglect of pressure drop and thermal losses in the piping*. When disregarding the losses along the pipes, the thermodynamic state at the outlet of one component is equivalent to the state at the inlet of the next one;
- *Neglect of thermal losses in the TES*. According to IEA (2014), the thermal losses in thermal storage cycles are much smaller than in existing electricity storage technologies, including pumped hydro and BES. Moreover, the study by Zaversky et al. (2013) performs an in-depth approach to the heat losses found in a molten salt thermal storage tank. It considers the absorbed solar irradiation at the tank's outer surface and wind speed, obtaining that when the storage is fully charged, the heat losses are about 270 kW and 210 kW for the hot and cold tanks, respectively. Despite that, they were neglected in the simulations performed in the present investigation;
- *Hourly time step*. Concentrating solar power plants have high transient effects because of the changing cloud and aerosol cover and the constantly changing incidence of solar radiation. Because of this, when it is desired to evaluate the instantaneous behavior of components of a CSP plant, it is interesting to use time resolutions of the order of minutes. However, the present study aims to analyze the annual behavior of these systems, for which calculations with the hourly resolution are sufficient and significantly reduce the computational cost involved;
- *Design point thermal efficiency of the power block*. For the sizing of the solar field and the plant storage system, the thermal efficiency of the power block under nominal conditions was used. Nevertheless, it is known that such efficiency is sensitive to several factors, among them the temperature of the HTF. For example, in topology (i), the HSM is heated to about 385 °C by synthetic oil at 395 °C. However, during discharge from the TES, the HTF is heated up to 375 °C by the HSM, thus reducing the efficiency;
- *Fixed conversion rate from gross to net*. Similar to the previous assumption, a gross to net generation conversion rate of 90% was assumed. However, it also varies according to the plant operation, especially during the TES loading and unloading processes, which require a higher mass flow rate of HTF, and consequently higher pumping power;

- *Optimal operating conditions*. In addition to the simplifications mentioned, plant operation was also assumed under optimal conditions, i.e., without broken mirrors, errors in tracking the Sun's trajectory, or dust over the SCAs. According to Turchi (2010), regular mirror washing has been proven to maintain mirror reflectance at installed conditions;
- *Adapted DMS costs*. The costs for conventional CSP-PTC plants are available from multiple sources. However, it was not possible to find detailed information about PTC plants with DMS technology. Because of this, specific costs for these configurations were adapted from SPT and LFR plants using molten salt as HTF, based on the report by (TURCHI et al., 2019);
- *Economies of scale neglected*. Usually, economies of scale decrease cost per unit as long as the enterprise-scale increases. Despite that, these effect details are often not disclosed and depend heavily on the negotiation process specific to each initiative. Consequently, they have not incorporated in this study these effects details are not most of the output enables an increase in scale.

3.2 METEOROLOGIC DATA

The site chosen for the simulations is Bom Jesus da Lapa (BA) because of its high availability of solar radiation. It locates in a semi-arid region in Northeastern Brazil. Among the locations in the country with high-quality meteorological data over long periods, it stands out for presenting the highest annual normal direct irradiation, 2198 kWh m^{-2} yr^{-1} (MALAGUETA et al., 2013). Furthermore, the region's climate presents two well-defined divisions: the dry season, which occurs from April to September, and the rainy season, lasting from October to March. Consequently, the higher cloudiness coincides with the most significant insolation. The global DNI distribution can be observed by Figure 2.8, while it is shown for Bahia in Figure 3.6.

As already mentioned, this study applied the design point method, which grants an interdependence between the sizing of the different subsystems of the plant (i.e., solar field, energy storage system, and power block). That methodology uses a reference state (the design point) to estimate the collectors' field cover required to attend the power cycle thermal demand and guarantee a surplus for TES charging.

There are numerous ways to determine the reference date and time; the most commonly used are reviewed and by Martins et al. (2021), in which they are compared for different locations around the world with CSP initiatives. In the comparison performed, the study concludes that methods based on a specific date, such as solstices and equinoxes, do not present adequate results for all sites, conferring other techniques more suitable to be used universally. However, for Bom Jesus da Lapa, this method provides satisfactory outcomes. On this account, the present study follows that method,

Figure 3.6 – Direct normal irradiation over the state of Bahia

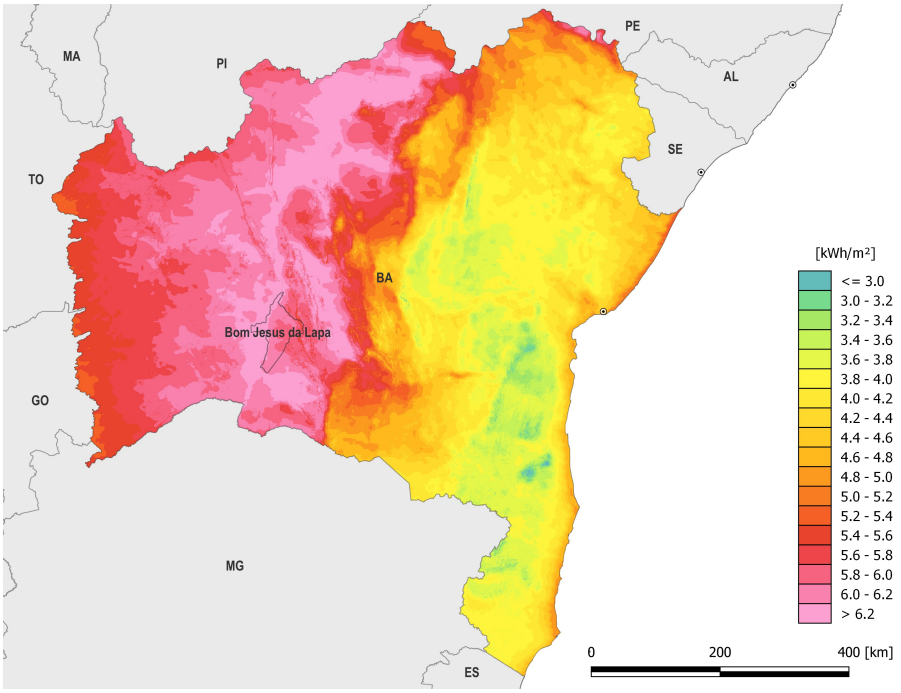

Source: Elaborated using QGIS (QGIS DEVELOPMENT TEAM, 2009) with data from Solargis (2019).
Note: 5.48 kWh m^{-2} day^{-1} corresponds to 2000 kWh m^{-2} yr^{-1}.

the most widely employed. It defines the design point as the solar noon on the summer solstice (between December 21-22 in the Southern Hemisphere and June 20-22 in the Northern Hemisphere (see Figure 3.7).

Figure 3.7 – Yearly variation of Sun-Earth position

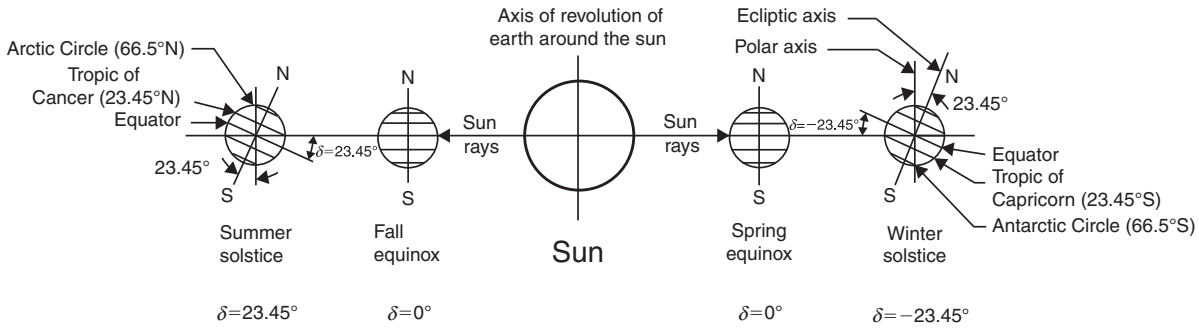

Source: Kalogirou (2014).
Note: The Northern Hemisphere is taken as reference.

This methodology is applied at the SAM Physical Trough Model (WAGNER; GILMAN, 2011) and also in several other studies (MONTES et al., 2009a, 2009b; HOU et al., 2011, 2015; BINOTTI et al., 2017; LEIVA-ILLANES et al., 2017; MARUGÁN-CRUZ et al., 2019).

Table 3.3 summarizes the facilities conditions at the specified design point.

Table 3.3 – Design point conditions

Parameter	Value	Unit
Site		
Location	Bom Jesus da Lapa	–
Latitude	-13.27	°
Longitude	-43.42	°
Elevation	458	m
Conditions at design		
Design point date	22 December	–
Design solar time	12:30	–
Design point direct normal irradiance	921	W m^{-2}
Weather		
Annual direct normal irradiation	2198	kWh m^{-2} yr^{-1}
Annual diffuse horizontal irradiation	671	kWh m^{-2} yr^{-1}
Average ambient temperature	26.1	℃
Average wind speed	1.6	m s^{-1}

Source: Elaborated by the author.

3.3 POWER BLOCK

The power block is where the thermal energy from the solar field or the TES converts into electricity through a typical Rankine cycle, similar to other thermoelectrical stations, such as those fired by fossil fuels. The following sections present the details about the Rankine cycle model implemented.

This system's sizing was performed to represent the most current CSP plants around the world. To this end, the SolarPACES database was consulted. It classifies the status of the projects into decommissioned, operating, under construction, or development. A summary of this survey is presented in Chapter 2. According to it, the 27 upcoming CSP-PTC projects have an average gross capacity of 144 MWe [(12)] and 4.6 hours of storage capacity (SOLARPACES, 2021). Therefore, based on that, a gross capacity of approximately 139 MW_e was adopted.

Since a share of the power generated in the plant is employed in auxiliary processes, a constant conversion ratio from gross to net power (ϕ_{PB}) of 90% was assumed, which means 10% of the gross electricity generation is self-consumed, and 90% is dispatched. Thus, it resulted in a net rated capacity of 125 MW_e. In off-design conditions, however, this ratio fluctuates depending on factors such as instant irradiance and TES operation.

$$\phi_{PB} = \frac{\dot{Q}_{PB,net}}{\dot{Q}_{PB,gross}} \tag{3.1}$$

[(12)] The gross capacity was considered because the net capacity was not disclosed for all facilities.

The total thermal demanded by the power block ($Q_{PB,th}$) is obtained regarding its thermal efficiency ($\eta_{PB,th}$). In design conditions, it is 38.9% for the oil-based and 42.2% for the salt-based topologies.

$$\eta_{PB,th} = \frac{\dot{Q}_{PB,th}}{\dot{Q}_{PB,gross}} \tag{3.2}$$

A Rankine cycle similar to Andasol-1 was modeled, with five vapor extractions in the turbine: one at high pressure (used to feedwater preheating) and four at low pressure (applied in vapor reheating and feed water preheater and deaerating). The extraction pressures used in Andasol-1, provided by STEAG (2020), resulted in liquid water formation at the preheating inlet, which can provoke equipment damage. Therefore, this study follows the procedure established by Weston (1992) to avoid it, which provides a regular interval between the saturation temperature at each extraction pressure, where each extraction temperature (T_i) is given by

$$\Delta T = \frac{T_{PB,sat,in} - T_{cond}}{n+1} \tag{3.3}$$

$$T_i = T_{cond} + i\Delta T \tag{3.4}$$

in which ΔT is the desired temperature difference; $T_{PB,sat,in}$ is the saturation temperature at the power block inlet pressure; T_{cond} is the temperature at the condenser inlet; n is the number of extractions; and i addresses the i-th extraction. The obtained pressures are shown in Tables 3.5 and 3.6.

Due to solar radiation inconstancy, solar power plants must operate efficiently both at full and partial load conditions and adjust the power output as the grid requirements. One technique used to achieve this is sliding pressure operation, under which the steam pressure is allowed to decrease as output falls, yet maintaining the steam temperature. This technique enables relatively high efficiencies in off-design circumstances, even though this may involve dropping from the water critical point (BREEZE, 2019). The main characteristics of the modeled power blocks for thermal oil-based plants – topologies (i) and (ii) – and for the salt-based plants – topologies (iii) and (iv) – are provided by Table 3.4.

The power blocks modeled in EBSILON Professional for the oil and salt-based plants are shown in Figures 3.8a and 3.9a, respectively. Both are constituted of the same components, differing only by the HTF used. In the first, synthetic oil (represented by gray lines) is used for liquid water heating and, subsequently, superheated steam

Table 3.4 – Power block characteristics

Parameter	Oil-based	Salt-based	Unit
Power cycle			
Design gross output	138.89	138.89	MW_e
Design net output	125.00	125.00	MW_e
Design thermal energy demand	357.04	329.12	MW_{th}
Solar fraction	100	100	%
Yearly output decline	0.5	0.5	%
Dispatch schedule	Uniform	Uniform	-
Heat transfer fluid			
Inlet pressure	35	5	bar
Outlet pressure	15	1.5	bar
Inlet temperature	395	565	℃
Outlet temperature	315	320	℃
Mass flow at superheater inlet	1606	732	kg s^{-1}
Mass flow at reheater inlet	198	150	kg s^{-1}
High-pressure turbine			
Inlet pressure	100	100	bar
Inlet temperature	373	543	℃
Inlet mass flow rate	163	123	kg s^{-1}
Extractions	1	1	-
Low-pressure turbine			
Outlet pressure	0.08	0.08	bar
Outlet temperature	41.5	41.5	℃
Outlet mass flow rate	102	82	kg s^{-1}
Extractions	4	4	-
Outlet quality	0.849	0.924	-
Efficiencies at design			
Cycle design efficiency	38.9	42.2	%
Gross-to-net efficiency	90.0	90.0	%
Turbine isentropic efficiency	88.0	88.0	%
Pump electric efficiency	85.0	85.0	%
Pump mechanical efficiency	99.8	99.8	%
Motor electric efficiency	85.0	85.0	%
Motor mechanical efficiency	99.8	99.8	%
Generator efficiency	96.0	96.0	%

Source: Elaborated by the author.

generation. Blue lines represent liquid water as red symbolizes vapor. In the second, such role is played by molten salt (dashed red lines for high temperature and blue lines for low temperature), as can be seen in the comparison of the two arrangements. The temperature-entropy (T-s) diagrams for the Rankine cycle are depicted in Figures 3.8b and 3.9b, as their properties are presented in Tables 3.5 and 3.6.

More information about the physical modeling of the power block's components are provided by STEAG (2021).

Figure 3.8 – Power cycle for the oil-based topologies

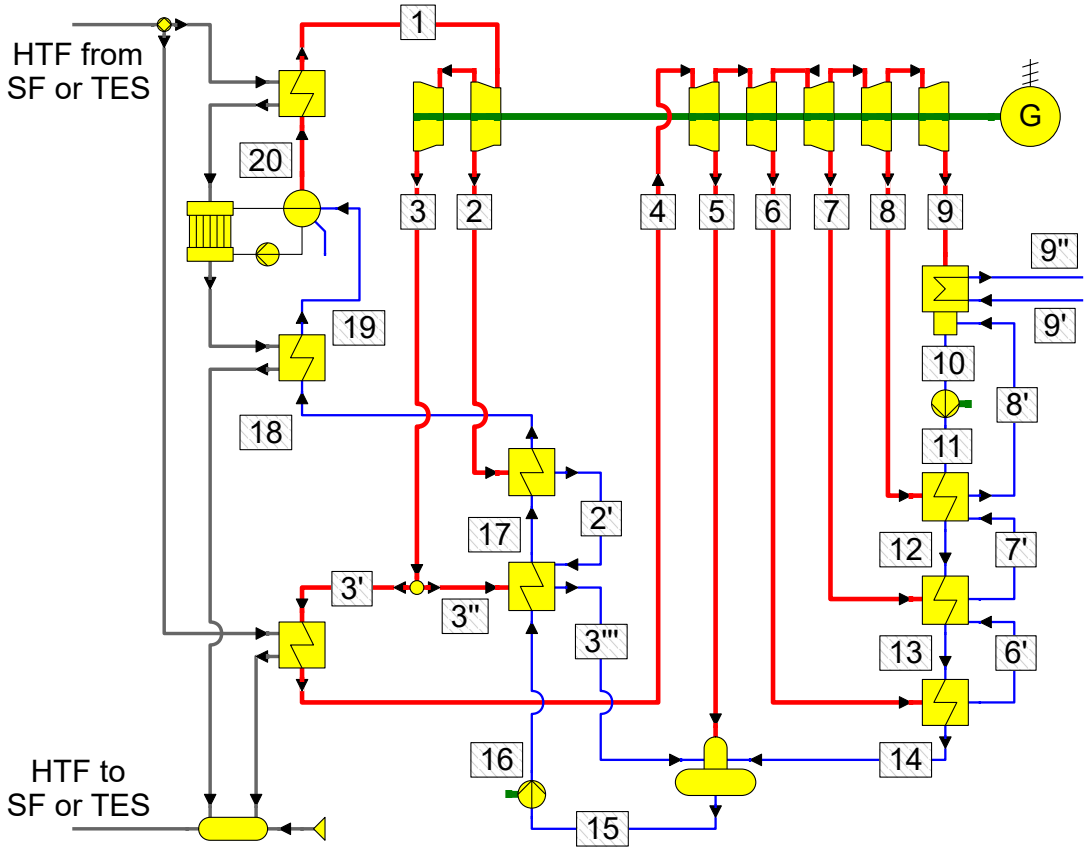

(a) Power block scheme

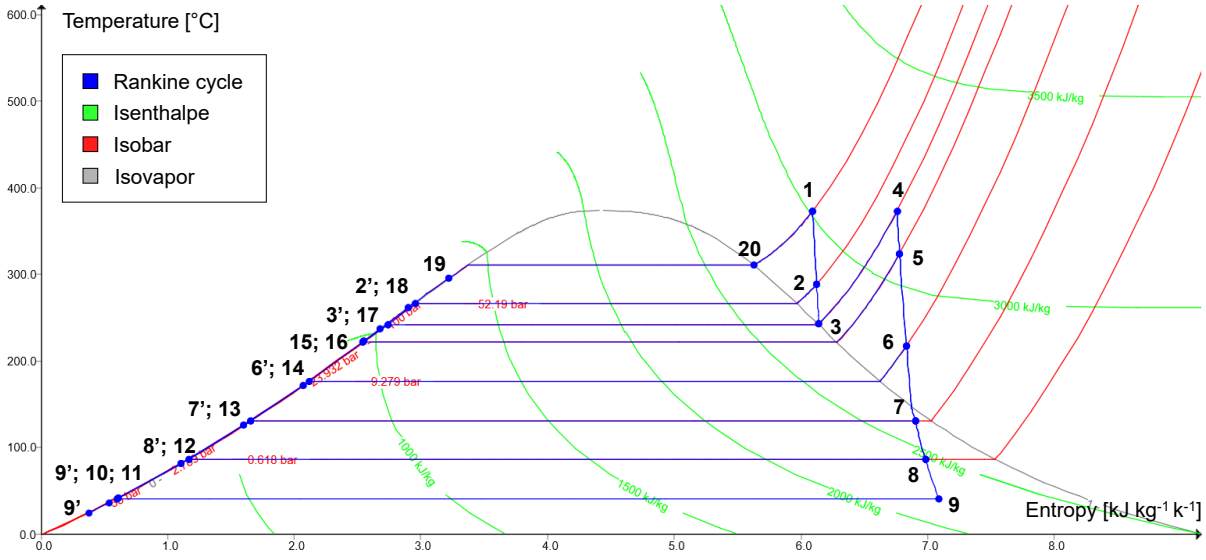

(b) Temperature-entropy (T-s) diagram

Source: Elaborated using EBSILON Professional (STEAG, 2020).

3.4 THERMAL ENERGY STORAGE

The next step in plant design is the TES sizing. As detailed in Chapter 2, this system decouples the temporal dependence between energy dispatch and radiation

Table 3.5 – State variables for the power cycle of the oil-based topologies

Point	Pressure [bar]	Temperature [°C]	Mass flow rate [kg s^{-1}]	Quality [-]	State*
1	100.0	373.0	163.4	–	ss
2	52.2	288.7	10.9	–	ss
2’	52.2	266.6	10.9	0.000	sat
3	35.5	243.6	152.5	–	ss
3’	35.5	243.6	147.2	–	ss
3”	35.5	243.6	5.3	–	ss
3”’	35.5	242.6	16.2	0.000	sat
4	35.0	373.0	147.2	–	ss
5	23.9	324.0	13.4	–	ss
6	9.3	217.7	12.4	–	ss
6’	9.3	176.7	16.3	0.000	sat
7	2.8	131.1	10.7	0.997	sat
7’	2.8	131.1	23.0	0.000	sat
8	0.6	86.7	8.6	0.914	sat
8’	0.6	86.7	31.6	0.000	sat
9	0.1	41.5	102.2	0.849	sat
9’	2.0	25.0	4458.3	–	cl
9”	1.0	36.5	4458.3	–	cl
10	0.1	41.5	138.8	0.000	sat
11	24.1	41.7	133.8	–	cl
12	24.0	81.7	133.8	–	cl
13	24.0	126.1	133.8	–	cl
14	23.9	171.7	133.8	–	cl
15	23.9	221.6	163.4	0.000	sat
16	100.2	223.7	163.4	–	cl
17	100.2	237.6	163.4	–	cl
18	100.1	261.6	163.4	–	cl
19	100.1	296.0	163.4	–	cl
20	100.1	311.0	163.4	–	ss

Source: Elaborated by the author.
Note: *The thermodynamic states abbreviation mean: cl – compressed liquid water; sat – saturated water-vapor; ss – superheated steam.

incidence.

In principle, a plant can be planned to operate continuously (24 hours a day) with the help of a massive TES. However, larger storages also require extensive solar fields, heavily impacting on the CAPEX and LCOE. Therefore, in practical applications, the storage capacity is often weighted considering a tradeoff between high energy output and low capital costs (BREEZE, 2019). Therefore a valuable parameter for such analysis is the LCOE, introduced in Equation 2.13.

The TES capacity and performance depend on multiple factors, such as the power block rated capacity, the solar field area, and daily insolation. The first stipulates the storage unloading power needed, as they are directly proportional. Assuming the TES input at a charge ($Q_{TES,cha}$) and output at discharge ($Q_{TES,dis}$) must be equivalent, the following expression is obtained:

Figure 3.9 – Power cycle for the salt-based topologies

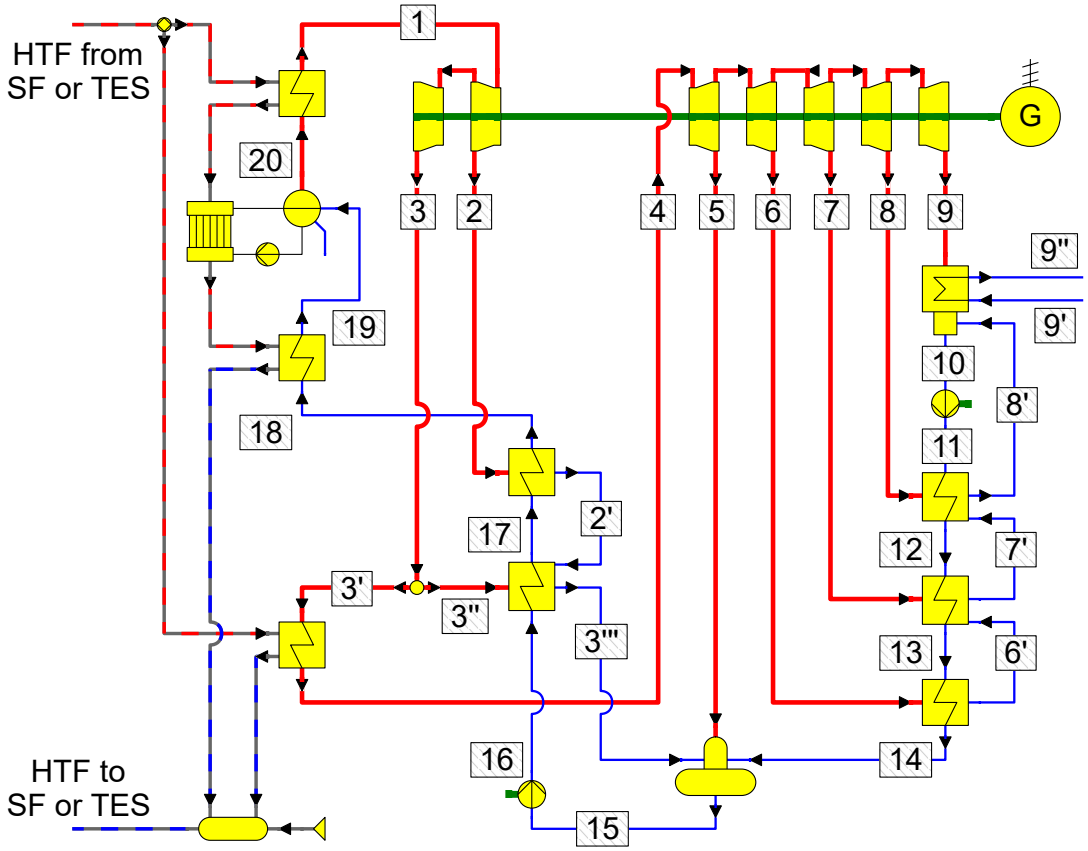

(a) Power block scheme

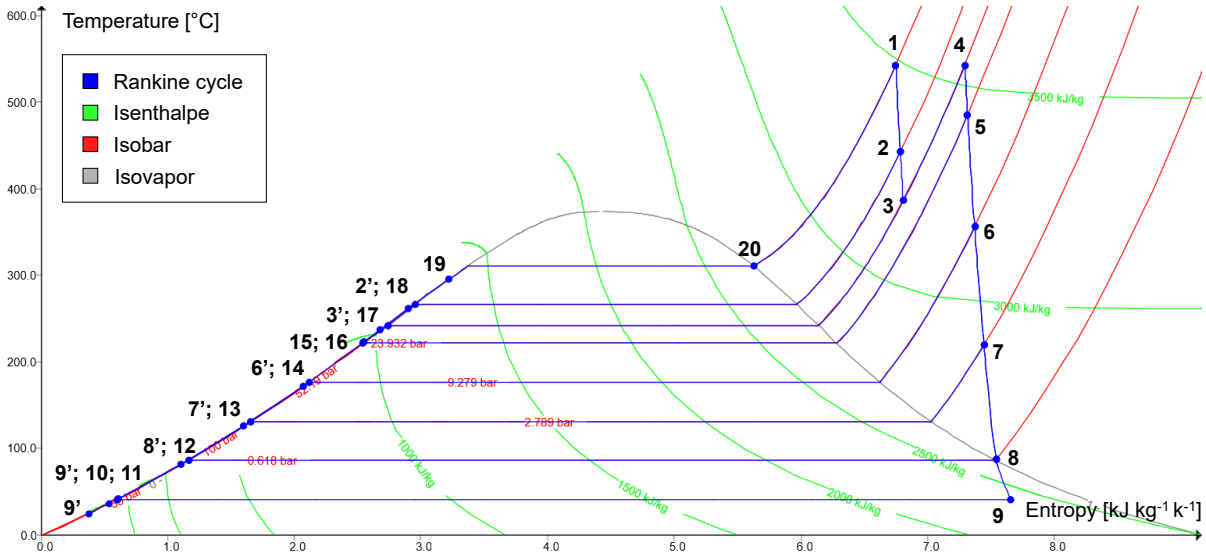

(b) Temperature-entropy (T-s) diagram

Source: Elaborated using EBSILON Professional (STEAG, 2020).

$$\left(\dot{Q}_{TES}\,\Delta t_{TES}\right)\Big|_{cha} = \left(\dot{Q}_{TES}\,\Delta t_{TES}\right)\Big|_{dis} \tag{3.5}$$

where $\dot{Q}_{TES,cha}$ and $\dot{Q}_{TES,dis}$ are the storage thermal power inlet and outlet, respec-

Table 3.6 – State variables for the power cycle of the salt-based topologies

Point	Pressure [bar]	Temperature [°C]	Mass flow rate [kg s^{-1}]	Quality [-]	State*
1	100.0	543.2	123.3	–	ss
2	52.2	442.8	6.6	–	ss
2'	52.2	266.6	6.6	0.000	sat
3	35.1	387.7	116.7	–	ss
3'	35.1	387.7	113.3	–	ss
3"	35.1	387.7	3,4	–	ss
3"'	35.1	242.6	10.0	0.000	sat
4	35.0	543.2	113.3	–	ss
5	23.9	485.3	9.0	–	ss
6	9.3	353.3	8.4	–	ss
6'	9.3	176.7	8.4	0.000	sat
7	2.8	220.4	7.6	0.000	sat
7'	2.8	131.1	16.0	–	ss
8	0.6	88.3	6.3	–	ss
8'	0.6	86.7	22.3	0.000	sat
9	0.1	41.5	82.0	0.924	sat
9'	2.0	25.0	3870.3	–	cl
9"	1.0	36.5	3870.3	–	cl
10	0.1	41.5	104.3	–	sat
11	24.1	41.7	104.3	–	cl
12	24.0	81.7	104.3	–	cl
13	24.0	126.1	104.3	–	cl
14	23.9	171.7	104.3	–	cl
15	23.9	221.6	123.3	0.000	sat
16	100.2	223.7	123.3	–	cl
17	100.2	237.6	123.3	–	cl
18	100.1	261.6	123.3	–	cl
19	100.1	296.0	123.3	–	cl
20	100.1	311.0	123.3	–	ss

Source: Elaborated by the author.
Note: *The thermodynamic states abbreviation are: cl – compressed liquid water; sat – saturated water-vapor; ss – superheated steam.

tively, while $\Delta t_{TES,cha}$ and $\Delta t_{TES,dis}$ are the storage charge and discharge duration. The storage charge span [13] depends on the design point DNI. Following the procedure described by Wang (2019), six hours were considered.

Assuming the power block demand can be fully powered by the stored heat ($\dot{Q}_{PB,th} = \dot{Q}_{TES,dis}$), the expression changes to:

$$\dot{Q}_{TES,cha} = \dot{Q}_{PB,th} \frac{\Delta t_{TES,dis}}{\Delta t_{TES,cha}} \tag{3.6}$$

The storage discharge power is alternatively given by a simple energy balance, as provided by the expression:

[13] The time required to completely fill the storage with the plant running on design conditions.

$$\dot{Q}_{TES,dis} = \dot{m}_{HSM} \left(h_{HT,out} - h_{CT,in} \right) \tag{3.7}$$

in which $\dot{m}_{HSM}$ represents the HSM mass flow rate, and $h_{HT,out}$ and $h_{CT,in}$ correspond to the hot tank inlet and the cold tank enthalpies, respectively. Thus, the HSM mass flow rate during discharge is easily obtained combining Equations 3.6 and 3.7.

Once the HSM mass flow rate is calculated, the storage mass capacity (m_{HSM}) is obtained by multiplying it by the expected TES autonomy. As will be discussed later, different storage capacities were evaluated. In these circumstances, it was assumed that by increasing the tank's volume, its height remains constant, growing only in diameter. Furthermore, according to Turchi et al. (2019), the tank volume should not be less than 14% of their maximum to ensure regular pumping operation; therefore, it was applied as the minimum tank level (TES_{heel}).

$$m_{HSM} = \frac{\dot{m}_{HSM} \, \Delta t_{TES,dis}}{1 - H_{heel}} \tag{3.8}$$

Following these procedures, at the design point, the TES demands 59.5 MW_{th} for topologies (i) and (ii) and 54.8 MW_{th} for topologies (iii) and (iv) from the solar field to be able to store an energy equivalent to one full-load hour of power cycle operation. The required HSM mass for one equivalent full-load operation hour is 16.0 kt (16.0×10^6 kg) for topology (i) and 3,7 kt (3.7×10^6 kg) for topology (iii).

Despite not being directly considered by the design point method for the storage sizing, the solar field dimension directly interferes with how fast the TES charge and discharge cycles can occur. Additionally, the more extensive the collectors' field opening area is compared to the required to supply the power block (i.e., the SM), the more heat can be stored without compromising the operation of the power block.

3.5 SOLAR FIELD

The solar field is the portion of the CSP installation that collects and concentrates solar radiation. It mainly comprises collector mirrors, receiver tubes, piping, steel structures, foundations, measurement, and control instruments.

According to STEAG (2020), the behavior of linear focusing solar field technologies can be described by the relations presented below. The solar absorbed power ($\dot{Q}_{solar}$) accounts for the DNI (G_n), the solar field net aperture area (A_{net}) and the solar field overall efficiency (η_{SF}).

$$\dot{Q}_{solar} = G_n \, A_{net} \, \eta_{SF} \tag{3.9}$$

3.5.1 Overall efficiency

The solar field efficiency accounts for effects of shading (η_{shad}), end losses (η_{end}), mirror cleanliness (η_{clean}), and mirror defocusing (f), as well as optical losses – given by the product of the optical peak efficiency, the IAM ($k_{\tau\alpha}$) and the spillage efficiency ($\eta_{spillage}$). The calculation of each one of those components is described in Section 3.5.

$$\eta_{SF} = \eta_{opt,0}\ k_{\tau\alpha}\ \eta_{shad}\ \eta_{end}\ \eta_{spillage}\ \eta_{clean}\ f \tag{3.10}$$

The collector's peak efficiency ($\eta_{opt,0}$) is either retrieved from the manufacturer (see Table 2.5) or estimated from its optical properties. It depends on the collector's reflectance (ρ_{col}), the receiver tubes absorptance (α_{abs}) and transmittance (τ_{abs}), the intercept factor (γ_θ), as well as on the ratio between bellows area and active aperture area η_{bel}.

$$\eta_{opt,0} = \rho_{col}\ \alpha_{abs}\ \tau_{abs}\ \gamma_\theta\ \eta_{bel} \tag{3.11}$$

The IAM accounts for increasing optical losses of solar radiation with increasing incident angle (θ), in degrees. It represents the increasing optical losses with an increasing incident angle, given in degrees. Thus, it helps describe collector test performance. The coefficients (b) used in its calculation are displayed in Table 2.5.

$$k_{\tau\alpha} = 1 + a_0 + a_1\theta + a_2\theta^2 \tag{3.12}$$

The shading factor (η_{shad}) takes into account the shading losses of the solar field. It is calculated based on a geometric relation dependent on the transversal tracking of the SCAs (ϕ_{trans}), their width (L_2), row distance (L_{row}), and tracking angle. It is calculated according to Equation 3.13. Shading occurs during sunrise and sundown when the Sun is close to the horizon.

$$\eta_{shd} = 1 - \min(1,\ \max(0,\ 1 - L_{row}\ \cos(\phi_{trans})/L_2)) \tag{3.13}$$

The endloss factor (η_{end}) accounts for PTC optical losses due to the solar irradiance not being reflected by the absorber at the row extremes. It considers the collector's length (L_{col}) and focal lengths (L_{foc}), as presented in Equation 3.14. End losses are only considered at the HTF inlet of the first PTC in the loop and the outlet of the last PTC. Therefore are not accounted for end losses and end gains between the PTCs.

$$\begin{aligned}\eta_{end} = 1 - k_1\ \ &\min(1, k_2\ L_{foc}/L_{col}\tan(\theta)) \\ &+ k_3\ \max(0, k_4\ \min(1, k_2\ L_{focal}/L_{col}\tan(\theta)) - L_{row}/L_{col})\end{aligned} \tag{3.14}$$

Under wind loads, the collector structure is deformed, reducing optical efficiency. The wind factor represents this effect. There is no model or standard formulation since data on this effect are sparse. Yet, EBSILON Professional models it accounting the factors $C_{spillage}$ and $E_{spillage}$.

$$\eta_{spillage} = 1 - C_{spillage} \ \min(1, \ E_{spillage}) \tag{3.15}$$

Dust on the PTC surface decreases its overall reflectance, necessitating periodic washing. The cleanliness factor is set between 0 – totally unclean; to 1 – totally clean. Similarly, the focus factor (f) accounts for the collector's defocus when the irradiance provides an energy surplus higher than the power block, and TES is available to use. It varies between 0 – entirely defocused; to 1 – entirely focused. As stated in Section 3.1, it was considered ideal plant operation, meaning spotless mirrors ($\eta_{clean} = 1$).

The availability factor (f) accounts for the collector's defocus when the irradiance provides a surplus, higher than the power block and TES are available to use. Thus, it varies between 0 – defocused; to 1 – focused. At design condition, fully focused collectors were considered ($f = 1$).

3.5.2 Net aperture area

Once the thermal energy demanded by the power block and the storage system is known, the solar field must be sized. Firstly, it is essential to estimate the nominal solar field area. In that condition, the $SM = 1$ and the SCAs supply the power block exclusively (once no TES is considered). Subsequently, it is calculated also accounting for the storage system, resulting in $SM \geq 1$. The CF represents the ratio between the system's nominal maximum electrical output [(14)] and the actual output throughout a year of operation.

$$CF = \frac{Q_{PB,net}}{8760 \ \dot{Q}_{PB,net}} \tag{3.16}$$

The solar field nominal required power ($\dot{Q}_{SF,th}$) is obtained considering it should meet the power block thermal demand ($Q_{PB,th}$).

$$Q_{SF,th} = Q_{PB,th} \tag{3.17}$$

[(14)] It is equivalent to the system output if it operated at its nameplate capacity throughout the entire year.

Moreover, by knowing the design point DNI and the solar field overall efficiency (η_{SF}), the effective area of the solar field (A_{net}) can finally be calculated, following Equation 3.9.

Using the collector's ratio of reflective to the gross area (ϕ_{SF}), the solar field gross area (A_{gross}) is obtained. It depends on the number of collectors (N_{col}), their dimensions (length – L_1, and width – W_2). Consequently, the number of collectors – or SCAs is obtained.

$$\phi_{SF} = \frac{A_{net}}{A_{gross}} \tag{3.18}$$

$$A_{gross} = n_{col}\ L_1\ L_2 \tag{3.19}$$

3.5.3 Solar power

Subsequently, other solar power metrics can be calculated. The available solar power ($\dot{Q}_{available}$) account for the absorbed solar power ($\dot{Q}_{solar}$) discounted the heat losses of absorbers ($\dot{Q}_{loss}$) and of the field piping ($\dot{Q}_{pipe}$).

$$\dot{Q}_{avail} = \dot{Q}_{solar} - \dot{Q}_{loss} - \dot{Q}_{pipe} \tag{3.20}$$

Similarly, the effectively available power ($\dot{Q}_{effective}$) accounts for the available solar power regarding the mirror defocus (what happens, e.g., at excessive solar irradiance, full storage, or maintenance routines). It is indeed the thermal power taken by the HTF, and is proportional to the mass flow rate at the solar field ($\dot{m}$) and the enthalpy difference of the fluid between the solar field outlet (h_{out}) and inlet (h_{in}).

$$\dot{Q}_{eff} = \dot{Q}_{solar}\ f - \dot{Q}_{loss} - \dot{Q}_{pipe} = \dot{m}(h_{out} - h_{in})\big|_{SF} \tag{3.21}$$

The heat losses at the receiver are given by the length-specific rate of heat loss (q'_{loss}), multiplied by the individual collector length (L_{col}) and the number of collectors (N_{col}).

$$\dot{Q}_{loss} = q'_{loss}\ L_{col}\ n_{col} \tag{3.22}$$

Lastly, the piping heat losses are given by the area-specific rate of pipe loss (q''_{pipe}), multiplied by the solar field net aperture area (A_{net}).

$$\dot{Q}_{pipe} = q''_{pipe} A_{net} \tag{3.23}$$

The parameters used for the solar field calculations in design conditions and the resultant specifications are presented in Table 3.7.

Table 3.7 – Solar field design parameters

Parameter	Oil-based	Salt-based	Unit
Power			
Design point direct normal irradiance	921.00	921.00	W m^{-2}
Nominal heat output	357.04	329.12	MW_{th}
Assembly and dimensions			
Solar collector assembly model *	ET150	ET150	–
Nominal solar multiple	1	1	–
Gross aperture area	0.56	0.51	km^2
Net aperture area	0.53	0.49	km^2
Total land required	1.39	1.29	km^2
Collectors per loop	4	4	–
Number of loops	161	149	–
Number of solar collector assembles	644	596	–
Position			
Collectors azimuth angle +	0	0	°
Solar azimuth angle at design	220.12	220.12	°
Solar incidence angle at design	10.37	10.37	°
Fluid			
Heat transfer fluid	Therminol VP-1	Solar salt	–
Loop inlet pressure	50	16	bar
Loop outlet pressure	35	1	bar
Loop inlet temperature	317	296	℃
Loop outlet temperature	395	565	℃
Solar field total mass flow rate	1736	580	kg s^{-1}
Losses			
Incidence angle modifier	0.983	0.983	–
End loss factor	0.997	0.997	–
Shading losses factor	1	1	–
Optical losses due to wind factor	1	1	–
Mirror cleanliness factor	1	1	–
Field availability	1	1	–

Source: Elaborated by the author.

Note: *The Eurotrough ET150 properties are presented in Table 2.5; +The azimuth angle of all collectors in the field, where zero degrees is pointing toward the Equator, equivalent to a North-South tracking axis orientation (see Figure 2.15c.

The PTC rate of heat loss to the environment per unit of length (q_loss) due to radiation, conduction, and convection mechanisms, are calculated by the equations be-

low. The coefficients *a*, *b*, *c* and *d*, usually informed by the manufacturer are available in Table 2.5. This calculation depends on the ambient temperature T_{amb} and the average HTF temperature, given by the mean between inlet and outlet absorber temperatures (T_{out} and T_{in}, respectively).

$$\begin{aligned} q'_l = {} & a_0 + a_1\Delta T + a_2\Delta T^2 + a_3\Delta T^3 + a_4\Delta T^4 + G_n\frac{\eta_{opt}}{\eta_{opt,0}}(b_0 + b_1\Delta T + a_2\Delta T^2) \\ & + c_1 T + c_2 T^2 + c_3 T^3 + c_4 T^4 + G_n\frac{\eta_{opt}}{\eta_{opt,0}}(d_1 T + d_2 T^2) \end{aligned} \tag{3.24}$$

3.6 FACILITY CONTROL

As presented in Section 2.5, a CSP facility can be designed to supply different types of loads in the grid. The strategy adopted in this study is based on the intermediate load approach, aiming to develop the most competitive designs. Furthermore, the simulated plants were configured to combine a more extended dispatch period, with reduced investment costs, meeting the baseload dispatch without aiming for continuous plant operation. Nevertheless, the plants were simulated in a wide range of storage capacities, from 0 to 12 hours, which allows further analysis of the impact of the storage arrangement and HTFs on its performance.

A similar approach is also found in the SAM Physical Trough Model control method presented by Wagner and Gilman (2011), which, in association with EBSILON library examples, served as the basis for the developed model.

The algorithm developed in the scope of this study for the facility control was achieved by using the EbsScript environment in EBSILON. It was programmed to run at each simulation timestep in such a platform, splitting the plant operation into five possible modes (see Figure 3.10), mainly subordinate to solar irradiance and available stored energy; these modes are presented below.

- *Mode 1 – Solar field active and TES charging*. The available solar energy is more than enough to supply the power block full-load, and the storage is not fully charged. Consequently, the gross energy output is nominal, while the heat surplus is stored. If the plant energy input surpasses the power block and TES maximums, the collectors are partially deflected;

- *Mode 2 – Solar field active and TES on standby*. It happens during the day when the instantaneous DNI is not enough to power the power block and TES, when the storage is full, or both. On such occasions, the power block runs can run in partial or full-load, depending on the solar energy available, and the storage level does not change. If more energy is available at the power block than the nominal required by the Rankine Cycle, the collectors are partially deflected;

Figure 3.10 – Information flow in the control of topologies with storage

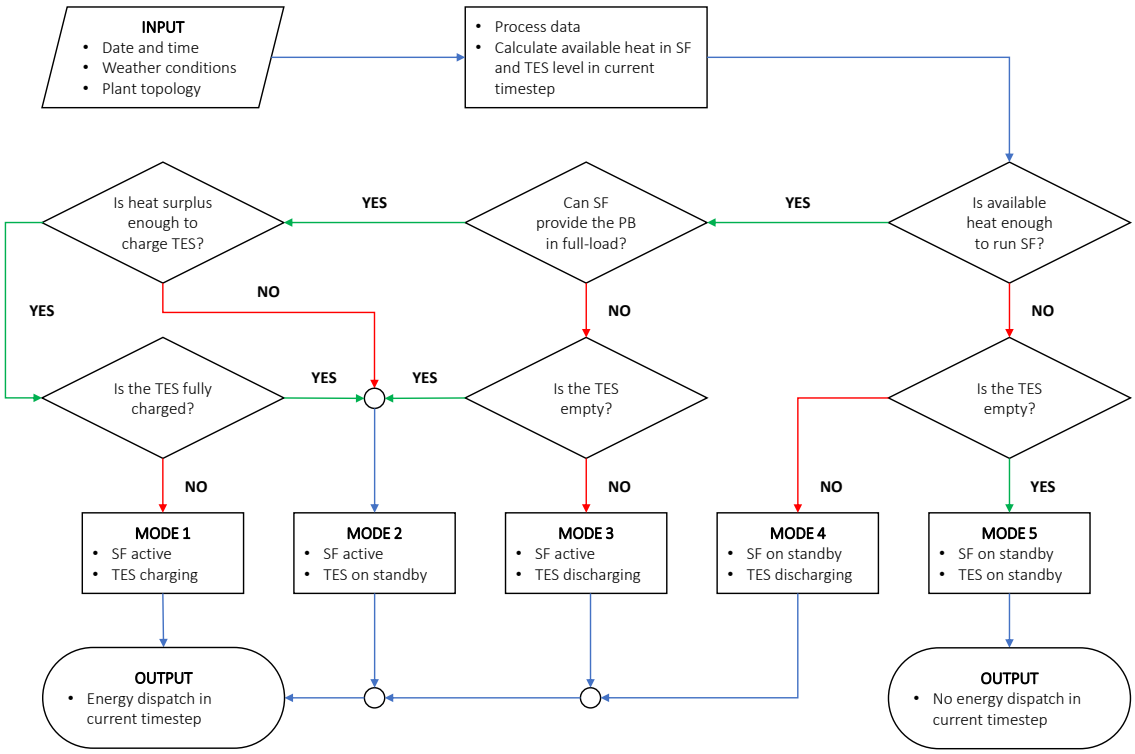

Source: Elaborated by the author.

- *Mode 3 – Solar field active and TES discharging*. The available DNI is not enough to run the power block in nominal charge, and the storage is not empty. In this case, the power block and TES both provide heat to the power block. If the additional heat from the TES is enough to complement the solar field output fully, the plant runs in full charge, otherwise in partial-load. The storage level decreases.

- *Mode 4 – Solar field on standby and TES discharging*. At night, when the storage is not empty. Consequently, the TES provides the energy to run the power block on partial-load or, ideally, nominal charge. The HTF does not circulate through the solar field, and the storage level decreases;

- *Mode 5 – Solar field and TES on standby*. It occurs when the storage is empty at nighttime or on overcast days, in which the solar irradiance is below the solar field cut-in value. In such a scenario, the plant output is null, and the TES remains unaltered;

In contrast, the operation control for topologies (ii) and (iv), their operation is simplified into only three modes by lacking TES system (see Figure 3.11). Therefore, the operation modes for such occasions are presented below:

Figure 3.11 – Information flow in the control of topologies without storage

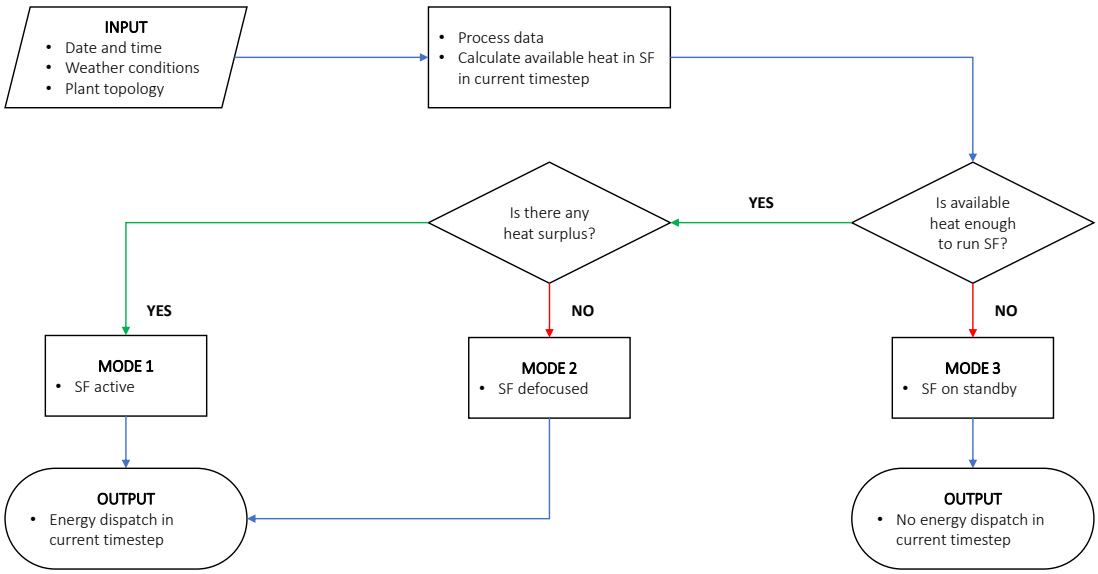

Source: Elaborated by the author.

- *Mode 1 – Solar field active*. The available heat at the solar field is enough to run the solar field and supply the power block in partial or full load configurations; it depends on the instantaneous DNI;
- *Mode 2 – Solar field defocused*. The available heat at the solar field is superior to the required by the power block in nominal conditions. Consequently, the collectors are partially deflected. The power block runs on full load, and the excess solar energy is not harnessed;
- *Mode 3 – Solar field on standby*. The available DNI is inferior to the solar field cut-in value. Therefore, the solar field and the power block remain on standby.

3.7 ECONOMIC MODEL

The equipment cost used in the plant must be defined to proceed with the economic analysis. For this, it was adopted the cost database developed for the SAM, reported in Turchi et al. (2019). This database does not include CSP-PTC-DMS plants, so a few costs were adapted when deemed appropriate, taking as a basis the reference values for SPT-DMS and LFR-DMS plants. These values were corrected for inflation. The nominal interest is based on Brazilian inflation and base interest rate in late 2019, given by IPCA and SELIC. Other corrections can also be performed to consider scale effects and the different materials used in the topologies. However, they were not considered, as explained in Section 3.1. An example of these corrections is the study by Starke (2019). It performs a 4E analysis (energetic, exergetic, exergoeconomic, and

environmental) for PTC-CSP facilities hybridized with fossil fuel and PV located in Bom Jesus da Lapa, and Crucero, in Chile.

It was first necessary to obtain the annual generation of the plant to perform the LCOE calculation. It was obtained through simulations of the same in EBSILON. During the system's useful life of 28 years (3 for construction and 25 for operation), as suggested by Wang (2019). In the first three years, the investment costs were divided equally. Then, the cash flows referring to energy dispatch revenues and operation and maintenance expenses from the fourth year were considered.

Following the economic model described in SAM (WAGNER; GILMAN, 2011), the system CAPEX is divided into two groups: direct and indirect costs. They are given by the sum of TDC and TIC.

$$CAPEX = TDC + TIC \tag{3.25}$$

The first group accounts for expenses related to specific plant systems. The TIC is given by the sum of the investments due to site improvements (C_{improv}) and the acquisition of the SCAs (C_{col}), HTF (C_{HTF}) [15], TES (C_{TES}), backup system (C_{BUS}), heat engine (C_{turb}), BOP (C_{BOP}) [16] associated feedstock and equipment.

$$TDC = C_{SF} + C_{TES} + C_{PB} = C_{impr} + C_{col} + C_{HTF} + C_{TES} + C_{BUS} + C_{turb} + C_{BOP} \tag{3.26}$$

Each of these costs is given by the following relations:

$$C_{SF} = C_{impr} + C_{col} + C_{HTF} = (c_{impr} + c_{col} + c_{HTF})\ 2.5\ A_{SF,gross} \tag{3.27}$$

$$C_{TES} = c_{TES}\ \dot{Q}_{TES,dis}\ \Delta t_{TES,dis} \tag{3.28}$$

$$C_{PB} = C_{BUS} + C_{turb} + C_{BOP} = c_{(}BUS + c_{turb} + c_{BOP})\ \dot{Q}_{PB,gross} \tag{3.29}$$

In turn, the indirect cots account for the expenses, not system-specific. The total indirect cost is the sum of land acquisition (C_{land}), EPC (C_{EPC}), and contingencies (C_{cont}).

$$TIC = C_{land} + C_{EPC} + C_{cont} \tag{3.30}$$

[15] The costs for site improvement and SCA and HTF acquisition are all related to the solar field.
[16] The costs for the backup system, heat engine and BOP are all related to the power block.

The following expressions give these parameters:

$$C_{land} = c_{land} \left(2.5\ A_{SF,gross} + A_{TES} + A_{PB}\right) \tag{3.31}$$

$$C_{EPC} = c_{EPC}\ TDC \tag{3.32}$$

$$C_{cont} = c_{cont}\ TDC \tag{3.33}$$

As for the OPEX, it accounts for the enterprise spending over one year to support its operation. It is given by the combination of fixed costs by the plant's capacity ($\dot{Q}_{PB,gross}$), variable costs by the plant's yearly net output (E_{net}), fuel acquisition, and insurance expenses. In this work, the OPEX was considered constant over the plant lifecycle, not corrected by inflation.

$$OPEX = c_{fix}\ \dot{Q}_{PB,gross} + c_{var}\ Q_{PB,net} + c_{fuel}\ c_{BUS} + c_{ins}\ TDC \tag{3.34}$$

Table 3.8 presents the specific equipment costs for thermal oil-based and molten salt-based (DMS) PTC plants. The equipment allocated in each system follows the classification presented in Kurup and Turchi (2015).

Although presenting the same mass storage capacity, cold and hot tanks do not have equal capital costs. Such difference is due, among other reasons, to the need for more insulation in hot tanks to reduce thermal losses to the environment. Such a fact can be observed in the work of Turchi et al. (2018), which compares the costs of different HSMs.

Finally, the LCOE was calculated according to the following Equation 2.13

3.8 PARAMETRIC ANALYSIS

A parametric analysis consists of the dependency evaluation of one or more variables from a given model. It is performed by varying such input parameters and assessing the model output.

Since the solar field size and the TES capacity have significant impacts on the facility performance, a parametric analysis was carried out to investigate their influences on two fundamental plant outputs: the LCOE, that express the cost of the generated electricity, and the CF, that measures the facility utilization. As discussed in Section 2.8, the LCOE has its limitations, and both VALCOE and LCOS can be complementary

Table 3.8 – Specific costs used at the economic analysis

Parameter	Oil-based	Salt-based	Unit
Investment			
Land cost	25	25	USD m^{-2}
Solar field	150	150	USD m^{-2}
Heat transfer fluid system	60	47	USD m^{-2}
Thermal energy storage	62	22	USD kWh^{-1}
Balance of plant	90	290	USD kW^{-1}
Power block	910	1040	USD kW^{-1}
Operation and maintenance			
Fixed annual cost	66	66	USD kW^{-1}
Variable annual cost	4.0×10^{-3}	3.5×10^{-3}	USD kWh^{-1}
Financing			
Discount rate	4.40	4.40	%
Inflation	4.19	4.19	%
Nominal discount rate	8.77	8.77	%
Insurance	0.50	0.50	%
Contingency	7.00	7.00	%
Engineering, procurement and construction	11.00	11.00	%

Source: Data from Turchi et al. (2019).

used. Nevertheless, for the calculation of the latter two, some assumptions are required that make difficult their comparison with other studies. Thus, such metrics were not evaluated in this study.

A hypothetical testing dataset was generated for combinations of solar fields with a SMs between 1 and 3 and TES with a capacity between 0 (no storage) and 12 hours were tested while keeping other parameters constant, resulting in 334 annual simulations in EBSILON Professional for the set of the four topologies. The domain resolutions for the SM and the TES capacity are 0.25 and 1 hour, respectively.

Subsequently, these analysis results were considered to delimit the most competitive plant settings for each scenario, i.e., the ones presenting the lowest LCOE.

3.9 CHAPTER CONCLUSIONS

This chapter included a description of the methodology applied in the development of this study. For this purpose, the procedures for sizing the CSP plants analyzed here were detailed. The components included in the plant structure and configuration are based on Andasol-1.

All the plants were sized for the locality of Bom Jesus da Lapa, which presents the country's highest annual direct normal irradiation and is situated in a semi-arid region with well-defined dry and wet seasons.

Following the design point method, there is an interrelation between the size of the solar field and the storage capacity. Because of this, first, the power block is sized.

Then, its net power is based on CSP-PTC plants under construction and development worldwide. At the same time, the steam turbine extraction pressures have been selected to result in constant saturation temperature ranges for each. In turn, the turbine off-design behavior followed the Stodola cone law.

The storage system was initially sized to provide the power block for one hour at full load, making it easily scalable to higher storage capacities. In this configuration, the heat demand for its supply was obtained and the mass flow of HSM to feed the power block, thus calculating the total mass of fluid required.

After determining the thermal demand of the two previous systems, the sizing of the solar field was presented, relying on the optical and thermal model of the PTC. It was verified that for the nominal configurations of the plant, there is a linear relationship between the SM and the capacity of the TES (in hours), given by the expression

$$\Delta t_{TES,cha} = 6\ SM - 6 \tag{3.35}$$

Therefore, considering a $SM = 1$, the plant only meets the thermal demand of the power cycle ($\Delta t_{TES,dis} = 0$). Likewise, for a plant with 12 hours of storage capacity, the solar field must be oversized in 200% ($SM = 3$) to supply the power block and the TES with their nameplate heat input (see Figure 3.12).

Figure 3.12 – Relation between the storage capacity and the solar multiple

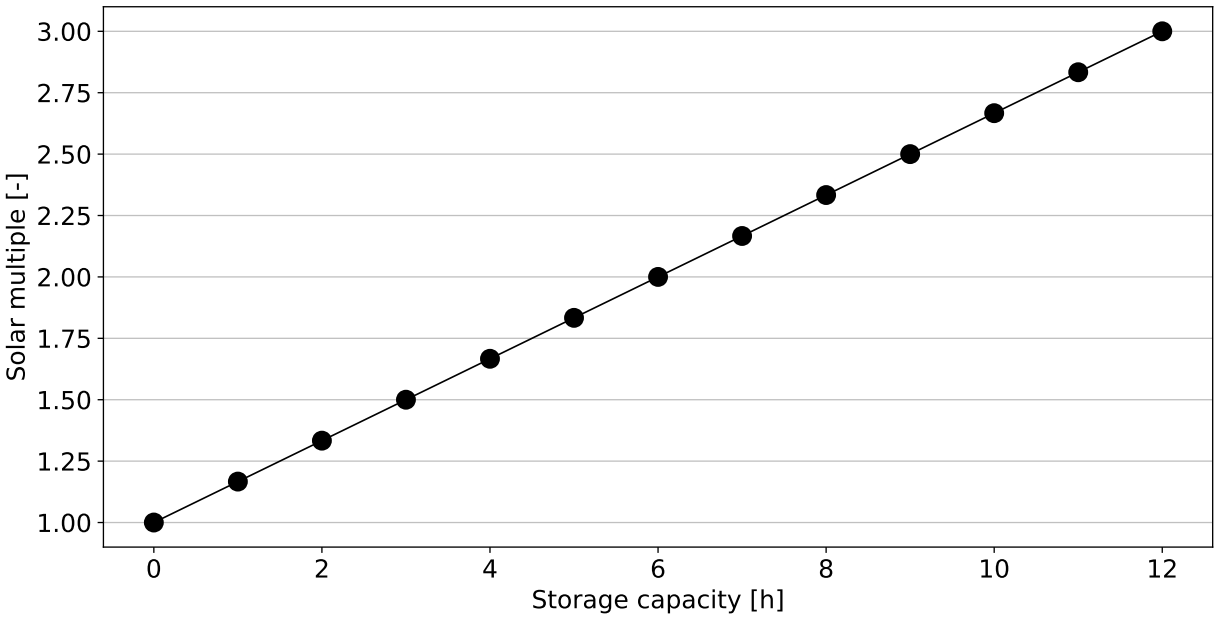

Source: Elaborated using Matplotlib (HUNTER, 2007).
Note: This curve represents the required solar field oversizing for the storage capacity required following the design point method, according to Wang (2019).

The chapter also briefly shows the logic developed for plant operation control and energy dispatch, based on the SAM physical trough model and examples present in EBSILON Professional.

Subsequently, the economic models developed to calculate the LCOE for the oil-based and salt-based plants were described. Finally, both the LCOE and the CF were optimized through parametric analysis. Different combinations of SM and storage capacities were addressed, resulting in 334 annual plant simulations.

4 RESULTS AND DISCUSSION

This chapter aims to present the main findings of this study. First the outputs of the parametric analysis performed for the four CSP topologies are shown; they are: (i) CSP-PTC plant with thermal oil as HTF at the solar field and a I2T molten salt TES; (ii) CSP-PTC plant with thermal oil as HTF at the solar field without the use of storage; (iii) CSP-PTC-DMS plant with molten salt both as HTF and HSM, with a D2T TES; (iv) CSP-PTC-DMS plant with molten salt as HTF at the solar field and without storage. After that, the plant with the lowest LCOE for each scenario is explored in more detail.

4.1 PARAMETRIC ANALYSIS

As previously mentioned, a sensitivity analysis was carried for each topology. It was done to obtain the lowest LCOE for each configuration. The independent variables explored were the SM (between 1 and 3, with a step of 0.25), and the TES storage capacity (within an hourly interval, between 0 and 12 hours). Once they present storage systems, the storage capacity for topologies (i) and (iii) is restricted to intervals between 1 and 12 hours. For topologies (ii) and (iv) that do not have storage capacity, 0 hours is considered. By varying such parameters, an amount of 234 simulations were required – 108 for topology (i); 9 for topology (ii); 108 for topology (iii); and 9 for topology (iv).

4.1.1 Levelized cost of energy

The LCOE outputs are presented graphically in Figure 4.1, which shows the multiple combinations of SM and storage capacity in a 3D space. In turn, Figure 4.2 shows the resultant LCOEs for different storage capacities. It is possible to observe the LCOEs obtained for the plants with thermal oil as HTF result LCOEs in a higher range than for the plants using molten salt, that results in a lower LCOE variability. The resultant data can be found in the A.

Due to the discrete interval of the parametric analyses' variables, these points were interpolated using SciPy's bisplrep function (VIRTANEN et al., 2020), aiming to obtain a continuous result over the analysis domain and better visualize the relationship between these three variables: SM, TES capacity, and LCOE. The resultant surfaces are presented in Figure 4.3.

It can be observed that for all arrangements, the use of TES provides a reduction in LCOE. For alternative (i), the storage employment results in lower LCOEs up to around six hours of capacity. In this range, the increased annual power generation by the TES provides higher revenues than the investment made in storage. In contrast, there is a tendency for CF convergence, as will be seen in the next section, which makes the CAPEX increase more significant than the resultant financial return. Such

Figure 4.1 – Levelized cost of energy output from the parametric analysis

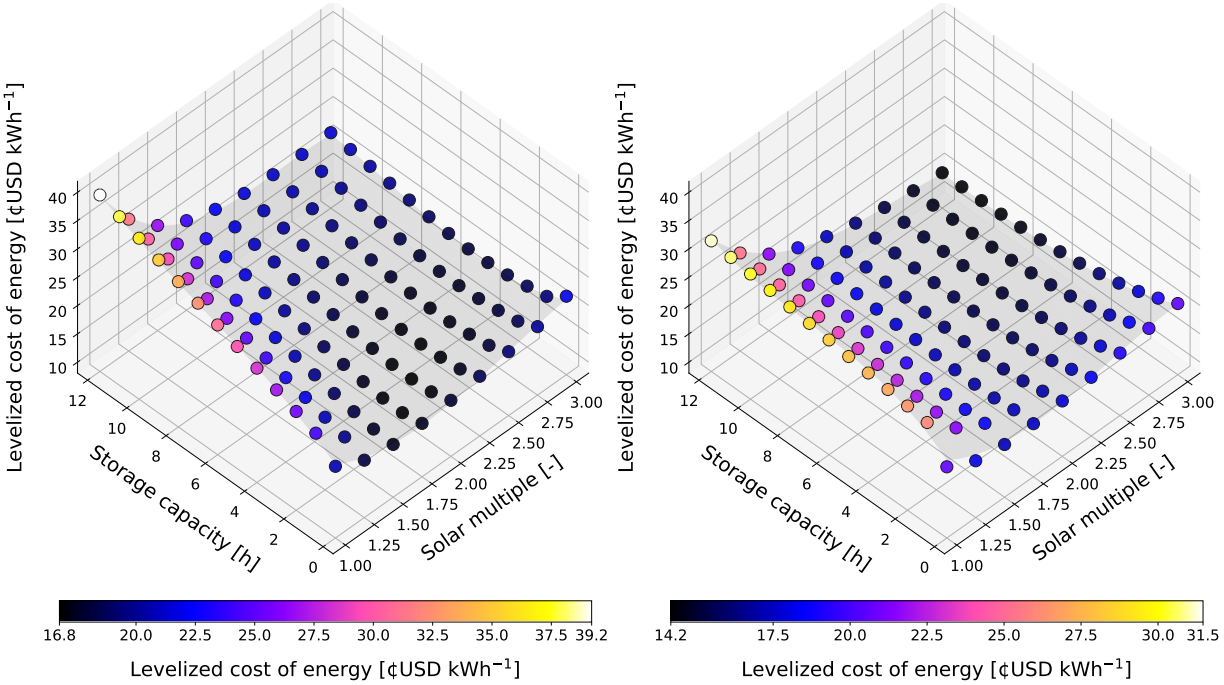

(a) Synthetic oil: topologies (i) and (ii)

(b) Molten salt: topologies (iii) and (iv)

Source: Elaborated using Matplotlib (HUNTER, 2007).

Figure 4.2 – Influence of the storage capacity and SM in the LCOE

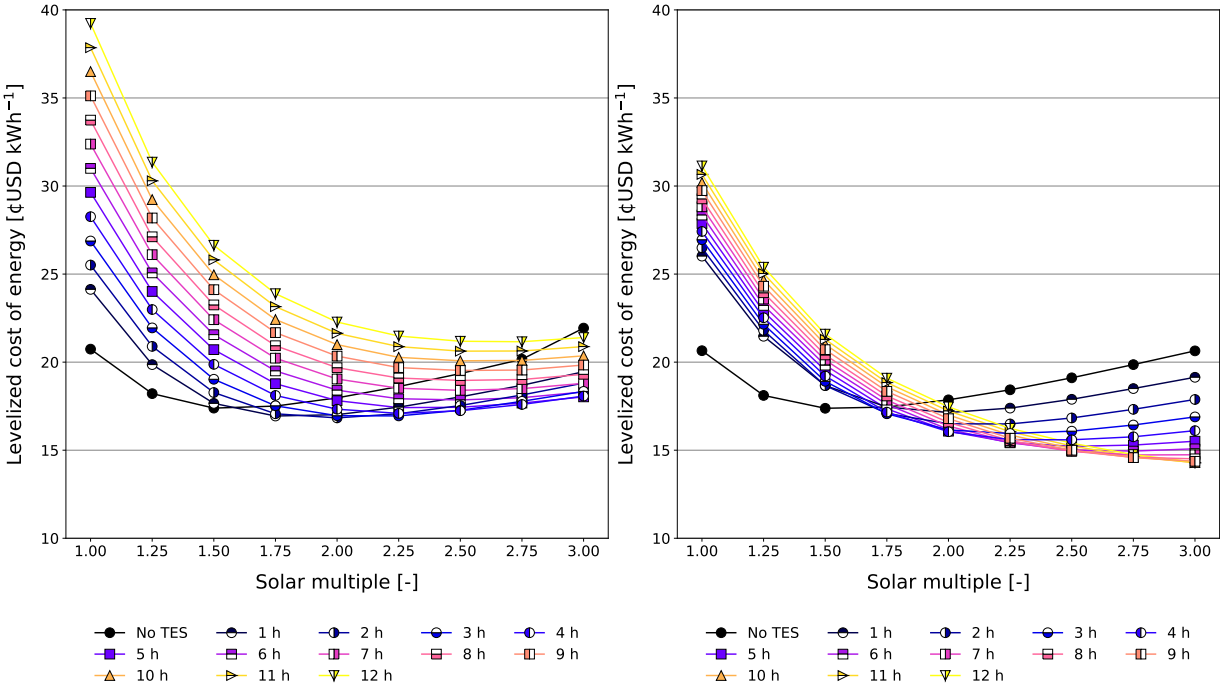

(a) Synthetic oil: topologies (i) and (ii)

(b) Molten salt: topologies (iii) and (iv)

Source: Elaborated using Matplotlib (HUNTER, 2007).

Note: The lines represent power plants with different TES capacities in the domain of the parametric analysis.

Figure 4.3 – Interpolated surface of levelized cost of energy

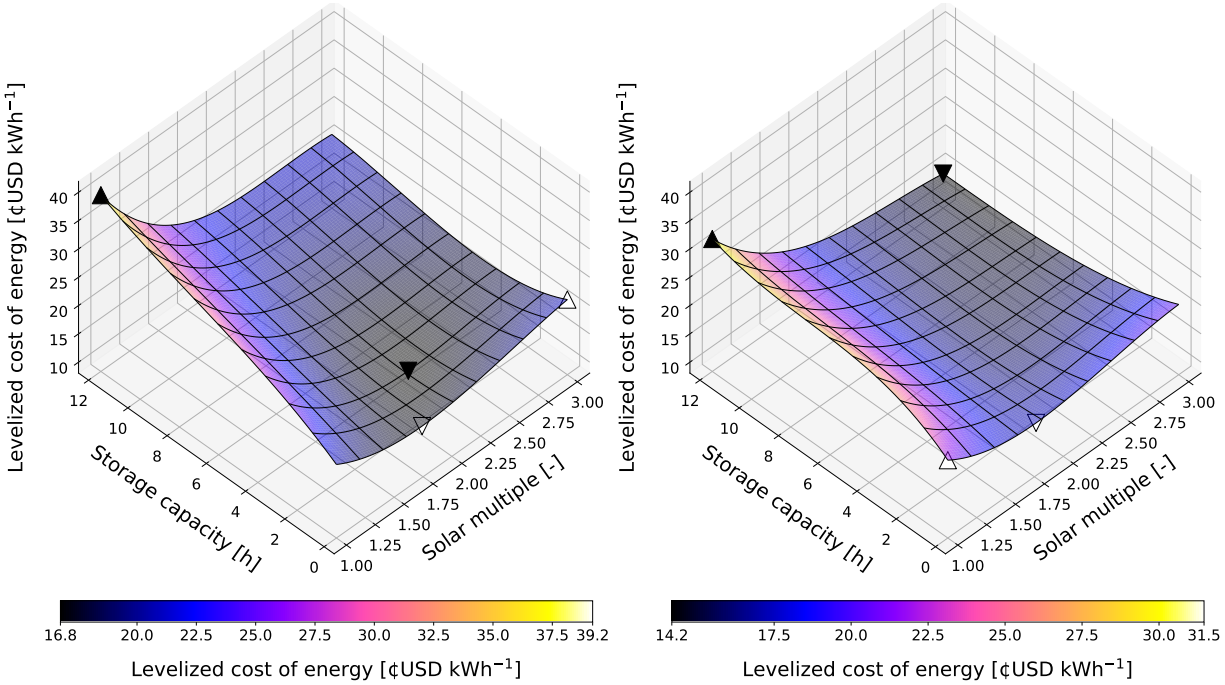

(a) Synthetic oil: topologies (i) and (ii)

(b) Molten salt: topologies (iii) and (iv)

Source: Elaborated using Matplotlib (HUNTER, 2007).

Note: The up-pointing triangle represents the highest LCOE with TES (black) and without (white), as the same pattern is followed for the down-pointing triangles.

Figure 4.4 – Upper view of the interpolated surfaces.

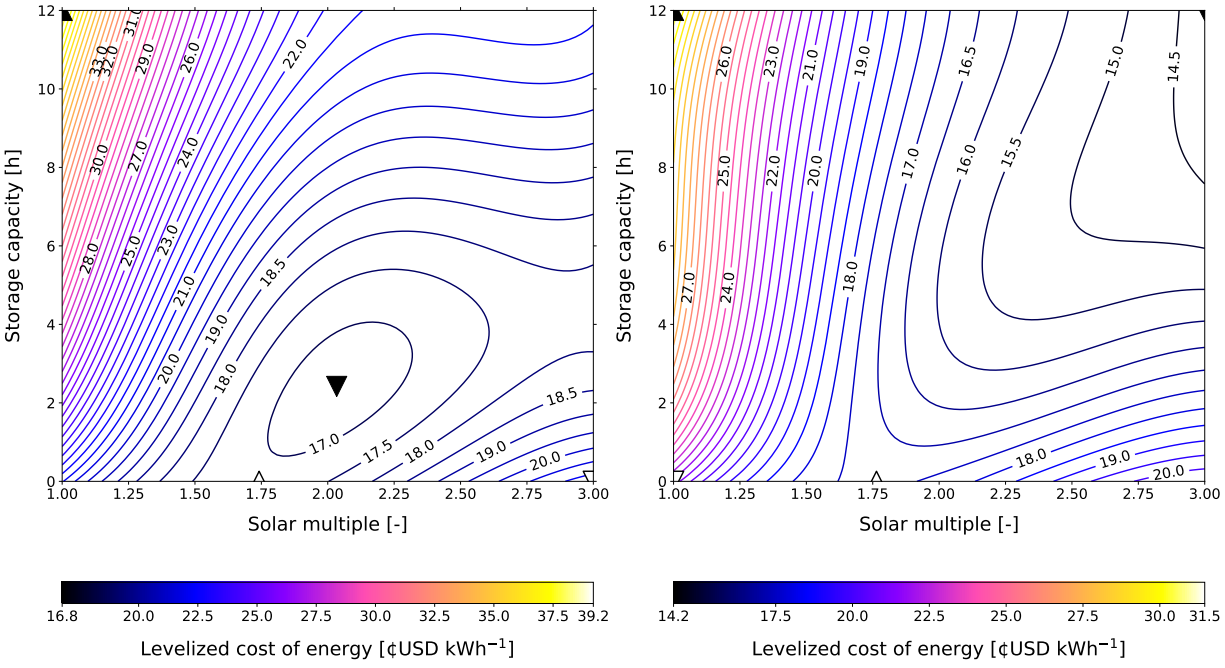

(a) Synthetic oil: topologies (i) and (ii)

(b) Molten salt: topologies (iii) and (iv)

Source: Elaborated using Matplotlib (HUNTER, 2007).

Note: This representations shows isolines for the levelized cost of energy at the parametric analysis domain. The pattern followed to represent the maximum and minimum points is the same as in the previous representations.

an analysis can also be done for the SM; for topology (i), the increase in SM, which is equivalent to an increase in the opening area of the solar field, provides higher power generation, which, up to around 2.00, is greater than the increase in the investment costs.

Something similar occurs with topology (ii), which consists of a CSP plant with thermal oil as HTF and does not have an energy storage system. However, even without storage capacity, it is possible to decrease the LCOE by increasing the solar field beyond the nominal value. For this configuration, the economic benefits of the increase are obtained for systems with SM with up to about 1.75.

On the other hand, for topology (iii), in the domain of the parametric analysis performed, there is a clear range of design values, approximately the straight line connecting points A (SM=1.75, TES=0 h) to point B (SM=3.00, TES=12 h) that provide the best combinations for DMS plants. This line shows that by increasing the storage capacity of the plant, the SM should be increased proportionally to enable the capture of the heat to be stored and use it in an economically efficient manner. It can also be seen that the lowest LCOE for the molten salt topologies in the solar field is obtained for a configuration with much higher storage capacities and SM than those using thermal oil. It happens primarily because the alternatives (iii) and (iv) operate their Rankine cycle at a higher temperature, which gives it higher thermal efficiencies. Thus this stabilization of the CF occurs later on for higher solar multiples. It also impacts the TES, since by raising the temperature of the stored fluid, a smaller amount of the same fluid is needed to supply the same thermal demand. With this, when using TES, there is a more significant relative advantage of the monotonically decreasing LCOE across the domain observed in the parametric analysis.

It can be inferred the lowest LCOE for topology (i), the CSP plant with I2T TES, is 16.77 ¢USD kWh^{-1}, achieved when a SM of 2.03 and a TES with 2.42 hours of capacity is used. For topology (iii), with a D2T TES configuration, the lowest LCOE is 14.18 ¢USD kWh^{-1}, is obtained for a SM of 3.00 and a TES capacity of 12 hours. As for the facilities without storage, the lowest LCOE for topology (ii) is 17.14 ¢USD kWh^{-1}, obtained for a SM of 1.74, and for topology (iv), it is 21.91 ¢USD kWh^{-1}, for a SM of as can be observed in Figure 4.5.

4.1.2 Capacity factor

A similar procedure was performed for the CFs. Figure 4.6 shows their distribution in a tridimensional space, while Figure 4.7 show isolines for each storage capacity simulated.

Like what was made for the LCOE, the parametric analysis results were interpolated for the CF. Figure 4.8 shows the interpolated surface, Figure 4.9 shows the interpolated SM-CF plane results.

Figure 4.5 – Range of levelized costs of energy in the parametric analysis domain

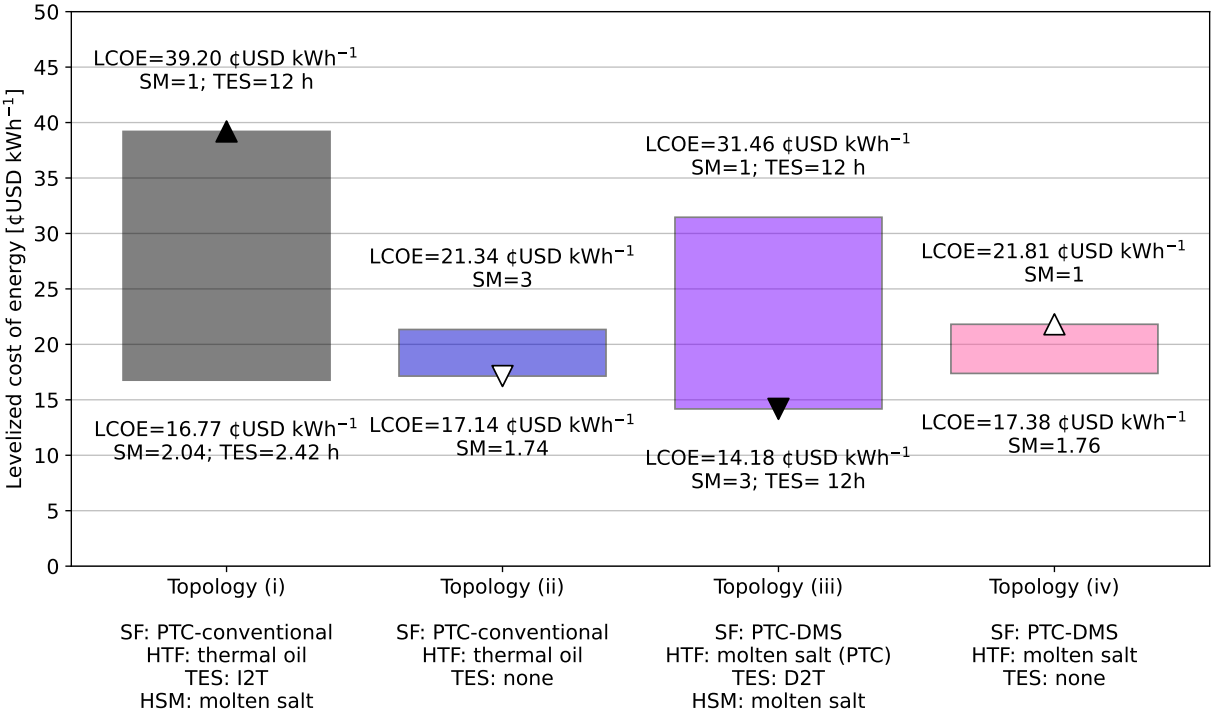

Source: Elaborated by the author using Matplotlib (HUNTER, 2007).

Note: The triangles facing up and down highlight the highest and lowest LCOEs, respectively, for plants with TES (black) and without TES (white).

For all arrangements, it can be observed that the use of TES provides a CF enhancement. The highest CF for each configuration is: topology (i) – 54.39%; topology (i), 38.56%; topology (ii), %; topology (i), %. These results are summarized in Figure 4.10. It can be observed that the best configuration for the CFdiverges from the nominal values (i.e., the ones specified by the design point method), as shown in Chapter 3, and also from the best design configuration for the LCOE. A larger power generation does not always mean higher specific revenue once the CAPEX, OPEX, and output increase at different rates.

For all alternatives, the CFincreases monotonically (i.e., when each variable increases, the CFincreases). Despite that, it can be noticed that the CFincrease slows down as far as the SM increases. It happens because the higher power surplus provided by a larger SF can be stored up to the TES capacity; beyond that point, it can not be used for a steam generation once the power block is already operating at full load and the storage capacity is already met, what causes energy waste. Therefore, this TES 'saturation' point occurs in increasingly higher SMs, as far as the TES capacity increases.

Figure 4.6 – Capacity factor output from the parametric analysis

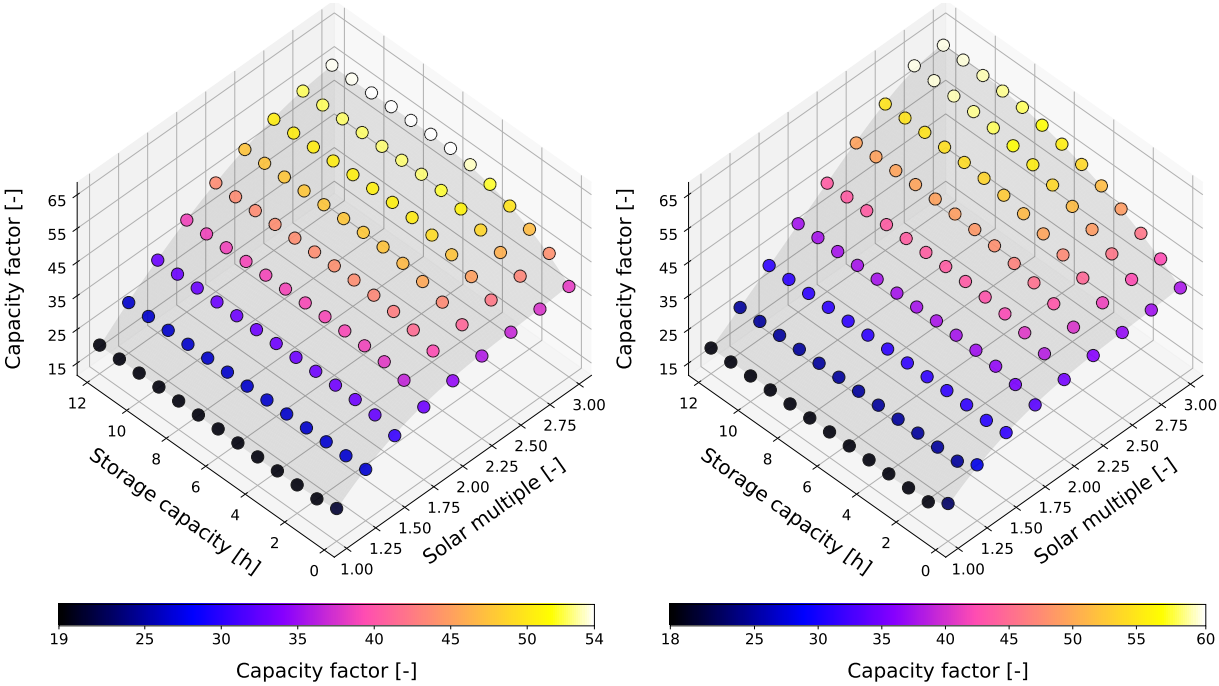

(a) Synthetic oil: topologies (i) and (ii)

(b) Molten salt: topologies (iii) and (iv)

Source: Elaborated using Matplotlib (HUNTER, 2007).

Figure 4.7 – Influence of the storage capacity and SM in the CF

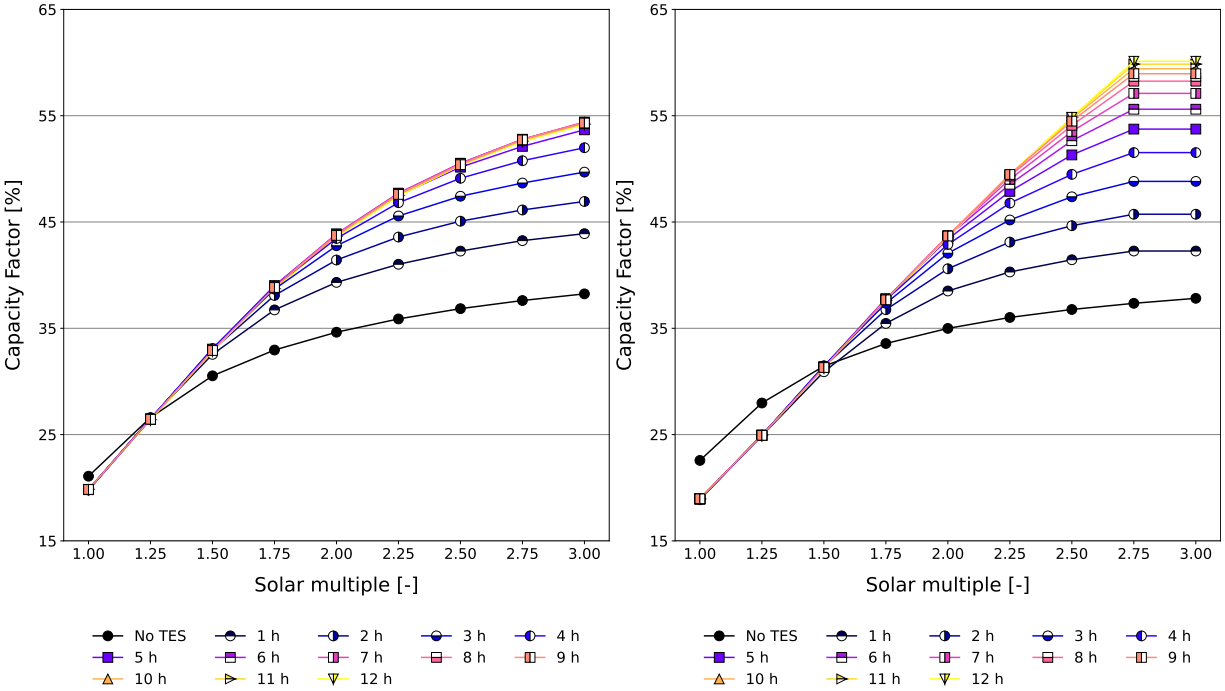

(a) Synthetic oil: topologies (i) and (ii)

(b) Molten salt: topologies (iii) and (iv)

Source: Elaborated using Matplotlib (HUNTER, 2007).

Note: The lines represent power plants with different TES capacities in the domain of the parametric analysis.

Figure 4.8 – Interpolated surface of capacity values

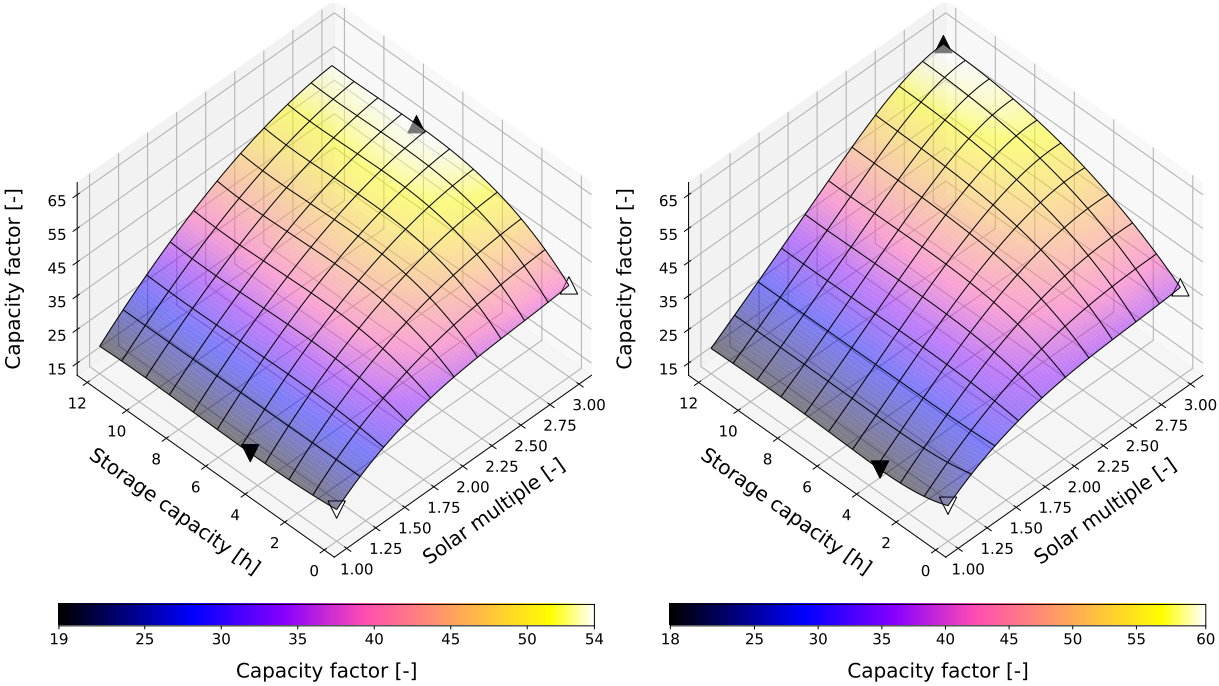

(a) Synthetic oil: topologies (i) and (ii) (b) Molten salt: topologies (iii) and (iv)

Source: Elaborated using Matplotlib (HUNTER, 2007).

Note: The up-pointing triangle represents the highest LCOE with TES (black) and without (white), as the same pattern is followed for the down-pointing triangles.

Figure 4.9 – Upper view of the interpolated surfaces shown above

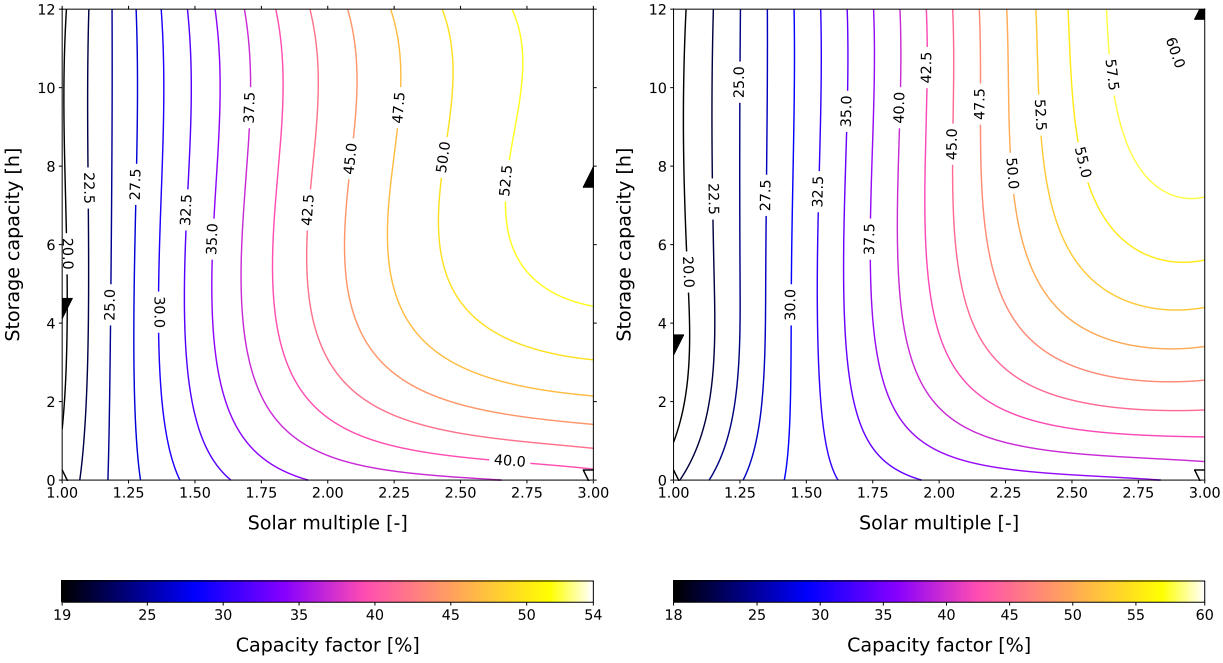

(a) Synthetic oil: topologies (i) and (ii) (b) Molten salt: topologies (iii) and (iv)

Source: Elaborated using Matplotlib (HUNTER, 2007).

Note: This representations shows isolines for the CF at the parametric analysis domain. The pattern followed to represent the maximum and minimum points is the same as in the previous representations.

Figure 4.10 – Range of capacity factors in the parametric analysis domain

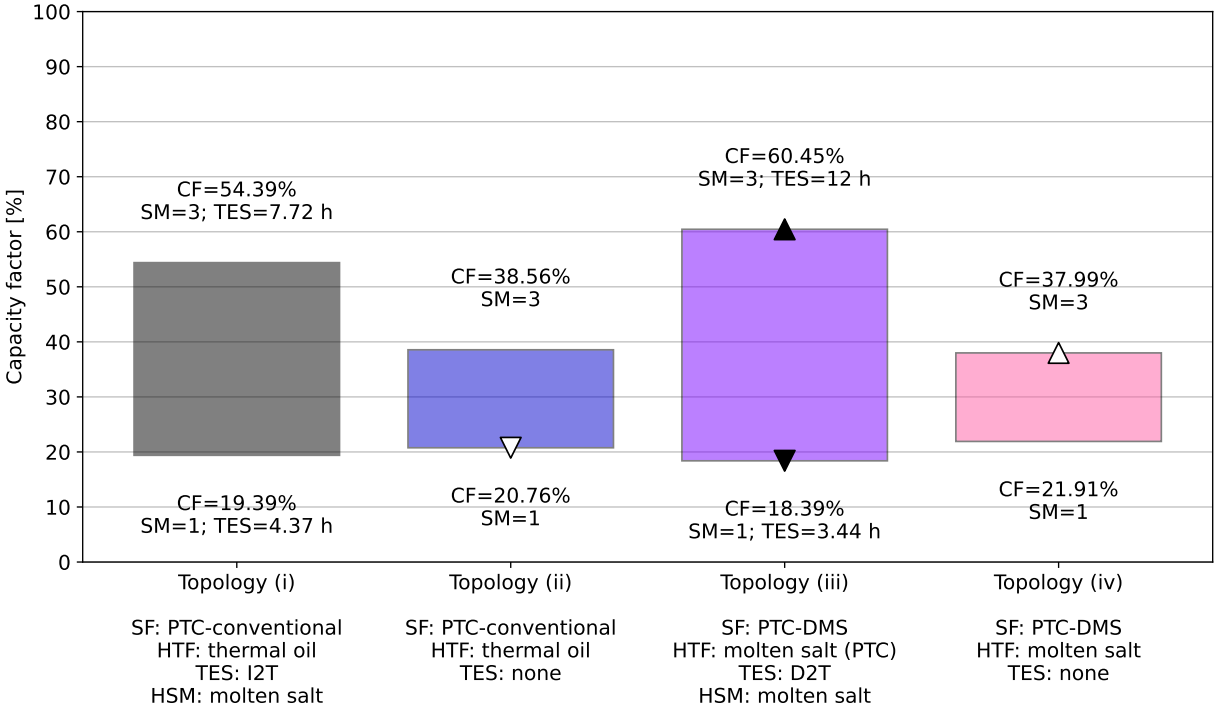

Source: Elaborated by the author using Matplotlib (HUNTER, 2007).
Note: The triangles facing up and down highlight the highest and lowest CFs, respectively, for plants with TES (black) and without TES (white).

4.2 TOPOLOGIES COMPARISON

From the interpolation of the parametric analysis results, the plant configuration was obtained with higher resolution, as shown in Table 4.1. With this, the plants were again simulated following these SM and TES capacity combinations. A comparison of these results is made in this section.

In both conventional topologies, the thermal oil is heated in the solar field to 395℃, providing steam generation at 375℃ and 100 bar in the power block. However, during the discharge process of TES from I2T, molten salt at about 385℃ is used in heating oil to approximately 375°. This temperature difference in the oil during operation in design configuration and during discharge reduces the thermal efficiency of the power block and, consequently, the plant as a whole.

Figure 4.11 – Visualization of plant status throughout the year

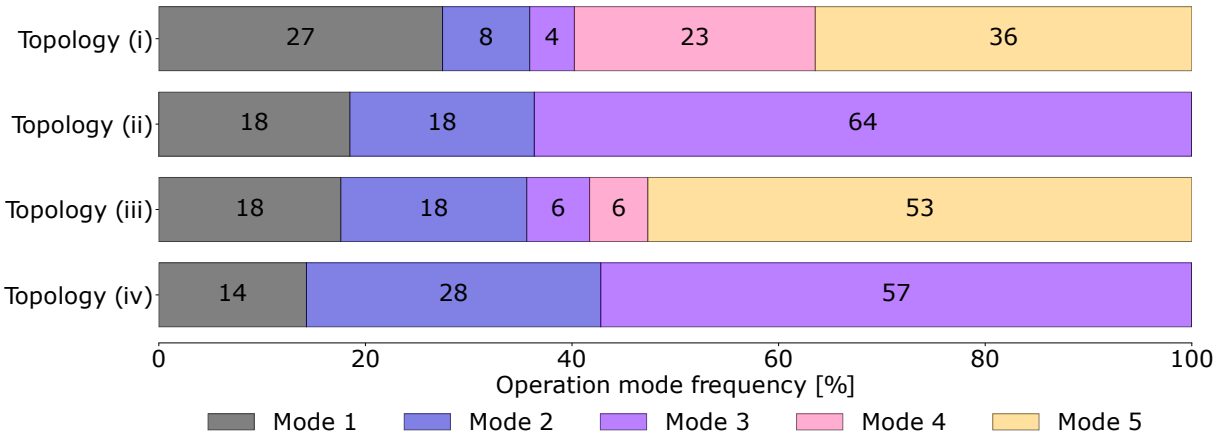

(a) Frequency of the plant operation modes

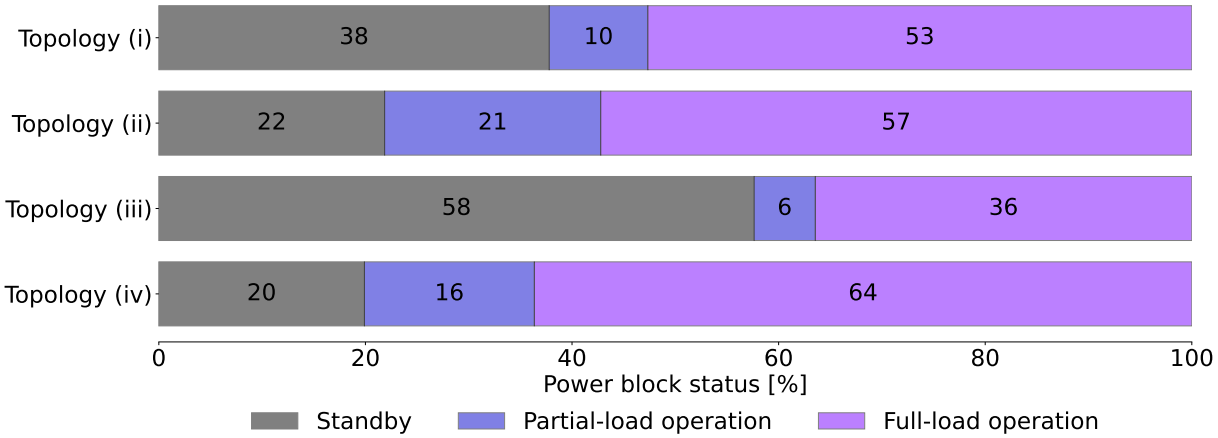

(b) Frequency of load cases at the power block

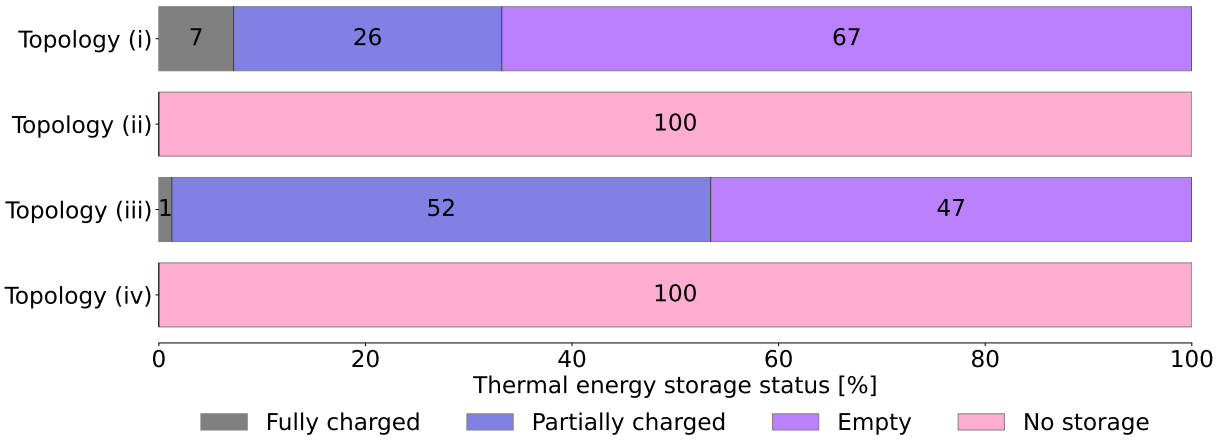

(c) Storage load status

Source: Elaborated using Matplotlib (HUNTER, 2007).
Note: One percent is equivalent to 3 days, 15 hours and 36 minutes throughout the year.

Table 4.1 – Main results for most cost-effective plant for each topology

Parameter	Topology (i)	Topology (ii)	Topology (iii)	Topology (iv)	Unit
Solar field					
Solar multiple	2.0	1.74	3.00	1.76	–
Available heat input	1446	1240	1777	1015	GWh
Solar power on absorbers	1636	1403	2232	1309	GWh
Heat loss by absorbers	119	106	357	240	GWh
Heat loss by piping	72	58	98	54	GWh
Heat absorbed by fluid	1275	1034	1723	864	GWh
Optical efficiency	62.33	59.41	67.92	61.54	%
Thermal efficiency	86.99	86.34	79.10	74.59	%
Solar field efficiency	54.22	51.29	53.72	45.90	%
Number of collectors	1309	1122	1785	1047	-
Total absorber tubes length	196	168	268	157	km
Total gross aperture area	1.13	0.97	1.54	0.90	km^2
Total net aperture area	1.07	0.92	1.46	0.86	km^2
Total facility footprint	2.84	2.44	3.87	2.28	km^2
Thermal energy storage					
Storage capacity	2.42	0.00	12.00	0.00	h
Stored energy	202	–	695	–	GWh
Hot tank temperature	385	–	565	–	℃
Cold tank temperature	323	–	319	–	℃
Hot tank level	30.11	–	30.72	–	%
Cold tank level	83.89	–	83.28	–	%
Stored fraction	15.29	–	40.15	–	%
Full-tank frequency	7.23	–	1.26	–	%
Empty tank frequency	66.80	–	46.58	–	%
Thermal energy storage footprint	0.01	0.01	0.01	0.01	km^2
Balance of plant					
Pumping energy demand	58	35	20	7	GWh
Pumping energy fraction	11.52	8.91	2.71	1.89	%
Power block					
Turbine gross capacity	138.89	138.89	138.89	138.89	MW
Turbine net capacity	125.00	125.00	125.00	125.00	MW
Gross output	503	395	725	366	GWh
Net output	445	360	706	359	GWh
Power block total heat input	1320	1058	1730	862	GWh
Capacity factor	40.67	32.87	64.43	32.82	%
Gross-to-net	88.48	91.09	97.29	98.11	%
Solar-to-electric efficiency	30.80	29.04	39.71	35.40	%
Thermal efficiency	33.73	34.02	40.77	41.71	%
Standby operation	52.66	57.21	36.45	63.65	%
Partial load operation	9.55	20.92	5.92	16.45	%
Full load operation	37.79	21.86	57.63	19.90	%
Power block footprint	0.01	0.01	0.01	0.01	km^2
Financial					
Capital costs	589.32	474.08	947.56	453.50	Mio.USD
Operation and maintenance costs	10.95	10.61	11.99	10.60	Mio.USD yr^{-1}
Levelized cost of energy	16.77	17.14	14.18	17.38	¢USD kWh^{-1}

Source: Elaborated by the author.
Note: *Annual average; $^{+}$annual total.

5 FINAL CONSIDERATIONS

The present study aimed to compare the thermodynamic and economic performance of two types of concentrated solar power plant arrangements. For this purpose, plants were modeled in four different scenarios. The first consists of a CSP-PTC plant using synthetic oil as HTF and molten salt as an HSM, used in TES with double indirect tank configuration. The second scenario is similar to the first, except that it does not have a TES. The third scenario uses molten salt both as the HTF and as HSM in a D2T configuration. The fourth scenario differs from the third by not having storage capacity. The plants' nominal net capacity is 125 MW. The location selected is Bom Jesus da Lapa, Bahia/Brazil, with the highest annual normal direct irradiation among all Brazilian sites, 2198 kWh m^2.

These plants' sizing followed the design point method, taking the summer solstice at noon as a reference. Then, these configurations were modeled in EBSILON Professional, in which the numerical simulations were performed in a quasi-dynamic regime. They were performed by varying two crucial factors in plant modeling: the solar multiple and the storage capacity. The solar multiple represents the ratio between the area of the solar field and the area needed to provide heat for power block and TES operation at nominal capacity. The storage capacity indicates the amount of energy the plant can store for later use. The parametric analysis sought to obtain the combination of parameters that provides the lowest LCOE and highest CF for each topology. Thus, the first output indicates the minimum energy selling price to provide a capital return, and the capacity factors indicate the equipment utilization.

It was identified that both solar field configurations (the first with oil as HTF, and the second with DMS) benefit from storage systems since such equipment extends their daily operation time and safeguards them from solar radiation fluctuations, often provided by atmospheric cloudiness. For the conventional solar field arrangement, there was a slight reduction in LCOE with the usage of TES, from 17.14 ¢USD kWh^{-1} without storage to 16.77 ¢USD kWh^{-1} when using it. However, the introduction of storage capacity caused a significant increase in the capacity factor, from 32.87% to 40.67%, resulting in higher power generation at the expense of higher initial investments. As for the DMS configuration, there was a significant reduction in LCOE, from 17.38 ¢USD kWh^{-1} to 14.18 ¢USD kWh^{-1} with the introduction of storage, and an significant increase in the capacity factor, from 32.82% to 64.43%.

When comparing the plants with the best performance, it is clear for both traditional CSP-PTC configuration and the DMS alternative that storage systems are essential equipment to provide more competitiveness to the CSP technology. It can enable it to compete and complement other energy sources currently available, bringing benefits from the reduction of unpredictability and costs, often associated with renew-

ables, and increase the flexibility of electricity dispatch, in alignment with consumers and the electricity sector managers demands. Moreover, the further development of TES and DMS has great potential for CSP. The results obtained indicate that its adoption increases solar field threshold temperature, from about 395 ℃ to about 565 ℃, and storage temperature, and consequently higher thermal efficiencies, storage density, and cost reduction. Another difference between the scenarios evaluated, referring to the TES configuration, shows the use of the same fluid in the solar field and the storage system provides higher thermal efficiencies for the power cycle, since the oil-salt heat exchangers, required by the I2T configuration, are not necessary by the D2T configuration. The storage temperature is virtually the same as that of the fluid from the solar field.

Other relevant observations made during this study show that when using the design point method for the specification of CSP, there is an interconnection between the size of the solar field, the storage capacity, and the nominal power block capacity. That, however, diverges from the most beneficial configurations from a technical or economic standpoint.

Despite the simplifications made to make such simulations and comparisons feasible, this study addresses a current issue in the context of concentrated solar power, whose main challenge in recent decades is the search for greater competitiveness. In this context, the optimization of design parameters and the comparative analysis between different solar field and thermal energy storage arrangements for CSP, among them the configuration of DMS and a direct double tank TES, still with the possibility of further development, aims to add to the literature and foster the discussion on energy transition.

5.1 RECOMMENDATIONS FOR FUTURE RESEARCH

From the research conducted over the last couple of years, several possibilities for further studies were identified, of which the following are highlighted below:

a) Validate the results with experimental data or even with data from an actual plant, as is the case of the HPS2 project plant, which aims to test storage systems similar to those simulated;

b) Follow the methodology described in this study in other simulation software such as Modelica, SAM, or TRNSYS and compare the results;

c) Expand the procedure described here to more plant configurations. For example, include other storage alternatives in the scope, such as DTC, ITC, passive, LTES or TCES. And also, compare the conventional and DMS alternatives to a DSG plant;

d) Expand the procedure described here to more storage alternatives, such as direct and indirect thermoclines, using ternary molten salts or thermal oil as HSM, analyze the influence of HSM on the results, as well as analyze LTES;

e) Deepen the thermoeconomic analysis performed here, taking into consideration exergetic and environmental aspects; item Include a probabilistic analysis of the LCOE and CF.

REFERENCES

ACHKARI, O.; FADAR, A. El. Latest developments on TES and CSP technologies – Energy and environmental issues, applications and research trends. **Applied Thermal Engineering**, v. 167, p. 114806, Feb. 2020. DOI: 10.1016/j.applthermaleng.2019.114806.

AKINYELE, D.O.; RAYUDU, R.K. Review of energy storage technologies for sustainable power networks. en. **Sustainable Energy Technologies and Assessments**, v. 8, p. 74–91, Dec. 2014. DOI: 10.1016/j.seta.2014.07.004.

ALDERSEY-WILLIAMS, J.; RUBERT, T. Levelised cost of energy – A theoretical justification and critical assessment. en. **Energy Policy**, v. 124, p. 169–179, Jan. 2019. DOI: 10.1016/j.enpol.2018.10.004.

ALOBAID, Falah; MERTENS, Nicolas; STARKLOFF, Ralf; LANZ, Thomas; HEINZE, Christian; EPPLE, Bernd. Progress in dynamic simulation of thermal power plants. en. **Progress in Energy and Combustion Science**, v. 59, p. 79–162, Mar. 2017. DOI: 10.1016/j.pecs.2016.11.001.

ANDREU-CABEDO, Patricia; MONDRAGON, Rosa; HERNANDEZ, Leonor; MARTINEZ-CUENCA, Raul; CABEDO, Luis; JULIA, J Enrique. Increment of specific heat capacity of solar salt with SiO2 nanoparticles. en. **Nanoscale Research Letters**, v. 9, n. 1, p. 582, Dec. 2014. DOI: 10.1186/1556-276X-9-582.

ASTARIZ, S.; VAZQUEZ, A.; IGLESIAS, G. Evaluation and comparison of the levelized cost of tidal, wave, and offshore wind energy. en. **Journal of Renewable and Sustainable Energy**, v. 7, n. 5, p. 053112, Sept. 2015. DOI: 10.1063/1.4932154.

AYDIN, Devrim; CASEY, Sean P.; RIFFAT, Saffa. The latest advancements on thermochemical heat storage systems. en. **Renewable and Sustainable Energy Reviews**, v. 41, p. 356–367, Jan. 2015. DOI: 10.1016/j.rser.2014.08.054.

BEHERA, Basanta Kumara. **Environmental technology and sustainability: physical, chemical and biological technologies for clean environmental management**. 1. ed. San Deigo: Elsevier, 2020.

BINOTTI, Marco; ASTOLFI, Marco; CAMPANARI, Stefano; MANZOLINI, Giampaolo; SILVA, Paolo. Preliminary assessment of sCO2 cycles for power generation in CSP

solar tower plants. en. **Applied Energy**, v. 204, p. 1007–1017, Oct. 2017. DOI: 10.1016/j.apenergy.2017.05.121.

BLANCO, Manuel; SANTIGOSA, Lourdes Ramirez (Eds.). **Advances in concentrating solar thermal research and technology**. Oxford: Woodhead Publishing, 2017. (Woodhead Publishing Series in Energy). OCLC: on1062320258.

BRAND, Bernhard; STAMBOULI, Amine Boudghene; ZEJLI, Driss. The value of dispatchability of CSP plants in the electricity systems of Morocco and Algeria. en. **Energy Policy**, v. 47, p. 321–331, Aug. 2012. DOI: 10.1016/j.enpol.2012.04.073.

BREEZE, Paul. Solar Power. In: POWER Generation Technologies. 3. ed. [S.l.]: Elsevier, 2019. P. 293–321. DOI: 10.1016/B978-0-08-102631-1.00013-4. Available from: https://linkinghub.elsevier.com/retrieve/pii/B9780081026311000134. Visited on: 6 Aug. 2020.

BUTTI, Ken; PERLIN, John. **A golden thread: 2500 years of solar architecture and technology**. London: Boyars, 1981.

CABEZA, Luisa F. **Advances in thermal energy storage systems: methods and applications**. [S.l.: s.n.], 2021. OCLC: 1202438045. Available from: https://www.sciencedirect.com/science/book/9780128198858. Visited on: 20 Aug. 2021.

CALLE, Alberto de la; BAYON, Alicia; PYE, John. Techno-economic assessment of a high-efficiency, low-cost solar-thermal power system with sodium receiver, phase-change material storage, and supercritical CO2 recompression Brayton cycle. en. **Solar Energy**, v. 199, p. 885–900, Mar. 2020. DOI: 10.1016/j.solener.2020.01.004.

CHAANAOUI, Meriem; VAUDREUIL, Sébastien; BOUNAHMIDI, Tijani. Benchmark of Concentrating Solar Power Plants: Historical, Current and Future Technical and Economic Development. en. **Procedia Computer Science**, v. 83, p. 782–789, 2016. DOI: 10.1016/j.procs.2016.04.167.

COWEN, Donald. **Archimedes and the Battle of Syracuse**. [S.l.: s.n.], 1981. University's Weaver Science-Engineering library.

DEMIREL, Yaşar; GERBAUD, Vincent. **Nonequilibrium Thermodynamics**. 4. ed. [S.l.]: Elsevier, 2019. DOI: 10.1016/C2017-0-02734-9. Available from: https://linkinghub.elsevier.com/retrieve/pii/C20170027349. Visited on: 19 Nov. 2021.

DINÇER, İbrahim; ROSEN, Marc. **Thermal energy storage: systems and applications**. 2. ed. Hoboken: John Wiley & Sons, 2011.

DLR. **Greenius Manual**. [S.l.: s.n.], 2018.

DOW. **Technical Data Sheet Dowtherm A**. [S.l.], 2021. Available from: https://www.dow.com/pt-br/document-viewer.html?ramdomVar=7891851074906667850&docPath=/content/dam/dcc/documents/en-us/productdatasheet/176/176-01463-01-dowtherm-a-tds.pdf. Visited on: 5 Oct. 2021.

DUFFIE, John A; BECKMAN, William A. **Solar engineering of thermal processes**. 4. ed. Hoboken: John Wiley & Sons, 2013. OCLC: 1047863094.

EASTMAN. **Technical Data Sheet Therminol® VP1 Heat Transfer Fluid**. [S.l.], 2019. Available from: https://productcatalog.eastman.com/tds/ProdDatasheet.aspx?product=71093459#_ga=2.246406852.175812311.1633443910-503879266.1633443910. Visited on: 5 Oct. 2021.

EPE. **Premissas e Custos da Oferta de Energia Elétrica: no horizonte 2050**. Português. Rio de Janeiro, Nov. 2018. P. 127. Available from: https://www.epe.gov.br/sites-pt/publicacoes-dados-abertos/publicacoes/PublicacoesArquivos/publicacao-227/topico-456/NT%20PR%20007-2018%20Premissas%20e%20Custos%20Oferta%20de%20Energia%20El%C3%A9trica.pdf. Visited on: 1 July 2020.

FELDHOFF, Jan Fabian; SCHMITZ, Kai; ECK, Markus; SCHNATBAUM-LAUMANN, Lars; LAING, Doerte; ORTIZ-VIVES, Francisco; SCHULTE-FISCHEDICK, Jan. Comparative system analysis of direct steam generation and synthetic oil parabolic trough power plants with integrated thermal storage. en. **Solar Energy**, v. 86, n. 1, p. 520–530, Jan. 2012. DOI: 10.1016/j.solener.2011.10.026.

FELDMAN, David; WU, Kevin; MARGOLIS, Robert. **H1 2021 Solar Industry Update**. [S.l.], July 2021. nrel/pr–7a40–80427, 1808491, mainid:42630. DOI: 10.2172/1808491. Available from: https://www.osti.gov/servlets/purl/1808491/. Visited on: 31 Aug. 2021.

FERREIRA, Willian Mendes. **Modelagem termodinâmica de uma planta fresnel com geração direta de vapor e armazenamento de energia térmica**. 2018. Dissertação de Mestrado em Engenharia Mecânica – Universidade Federal de Santa Catarina, Florianópolis.

GAUCHÉ, Paul; RUDMAN, Justine; MABASO, Mbalenhle; LANDMAN, Willem A.; BACKSTRÖM, Theodor W. von; BRENT, Alan C. System value and progress of CSP. en. **Solar Energy**, v. 152, p. 106–139, Aug. 2017. DOI: 10.1016/j.solener.2017.03.072.

GAZOLI, Jonas Rafael; JUNIOR, Nelson Ponce; SOUZA, Sergio Pereira de; PASCHOALOTTO, Luis Alexandre Catussi; SOUZA, Osvaldo José de. DIMENSIONAMENTO BÁSICO DO CAMPO SOLAR DE CONCENTRADORES CILINDRO-PARABÓLICO DA USINA TERMOSOLAR PORTO PRIMAVERA. pt, p. 10, 2018.

GEYER, Michael; OSUNA, Rafael; ESTEBAN, Antonio; SCHIEL, Wolfgang; SCHWEITZER, Axel; ZARZA, Eduardo; NAVA, Paul; LANGENKAMP, Josef; MANDELBERG, Eli. Eurotrough - Parabolic Trough Collector Developed for Cost Efficient Solar Power Generation, 2011.

GIL, Antoni; MEDRANO, Marc; MARTORELL, Ingrid; LÁZARO, Ana; DOLADO, Pablo; ZALBA, Belén; CABEZA, Luisa F. State of the art on high temperature thermal energy storage for power generation. Part 1—Concepts, materials and modellization. en. **Renewable and Sustainable Energy Reviews**, v. 14, n. 1, p. 31–55, Jan. 2010. DOI: 10.1016/j.rser.2009.07.035.

GUÉDEZ, Rafael. **A techno-economic framework for the analysis of Concentrating Solar Power plants with storage**. 2016. Doctoral Thesis – KTH Royal Institute of Technology, Stockholm.

HAHN, Philipp; MESQUITA, Marcelo; PEREIRA, Luciano Torres; ALENCAR, Carlos Artur; MATOS, Rogério A S; PEREIRA, Duarte; COSTA, Natasha. **Energia termossolar para a indústria: Brasil**. [S.l.]: Solar Payback, 2017.

HELLER, Peter W. (Ed.). **The performance of concentrated solar power (CSP) systems: analysis, measurement and assessment**. Cambridge: Woodhead Publishing, 2017. (Woodhead Publishing Series in Energy). OCLC: ocn952982969.

HO, Clifford Kuofei. **Software and codes for analysis of concentrating solar power technologies.** [S.l.], 2008.

HOU, Hongjuan; WU, Junjie; YANG, Yongping; HU, Eric; CHEN, Si. Performance of a solar aided power plant in fuel saving mode. en. **Applied Energy**, v. 160, p. 873–881, Dec. 2015. DOI: 10.1016/j.apenergy.2015.01.092.

HOU, Hongjuan; YANG, YongPing; HU, Eric; SONG, JiFeng; DONG, ChangQing; MAO, Jian. Evaluation of solar aided biomass power generation systems with parabolic trough field. en. **Science China Technological Sciences**, v. 54, n. 6, p. 1455–1461, June 2011. DOI: 10.1007/s11431-011-4366-4.

HUNTER, J. D. Matplotlib: A 2D graphics environment. **Computing in Science & Engineering**, v. 9, n. 3, p. 90–95, 2007. Publisher: IEEE COMPUTER SOC. DOI: 10.1109/MCSE.2007.55.

IEA. **Projected Costs of Generating Electricity 2020**. Paris, 2020. Available from: https://www.iea.org/reports/projected-costs-of-generating-electricity-2020.

IEA. **Technology Roadmap - Concentrating Solar Power**. Paris, 2010. Available from: https://www.iea.org/reports/technology-roadmap-concentrating-solar-power.

IEA. **Technology Roadmap - Solar Thermal Electricity**. Paris, 2014. Available from: https://www.iea.org/reports/technology-roadmap-solar-thermal-electricity-2014.

IEA. **World Energy Model**. Paris, 2021. Available from: https://www.iea.org/reports/world-energy-model.

IPCC. **Climate Change 2021: The Physical Science Basis. Contribution of Working Group I to the Sixth Assessment Report of the Intergovernmental Panel on Climate Change**. Ed. by V. Masson-Delmotte. [S.l.], 2021.

IRENA. **Electricity storage and renewables: Costs and markets to 2030**. Abu Dhabi: International Renewable Energy Agency, 2017.

IRENA. **Global Renewables Outlook: Energy transformation 2050**. Abu Dhabi: International Renewable Energy Agency, 2020a.

IRENA. **Green Hydrogen: A guide to policy making**. Abu Dhabi: International Renewable Energy Agency, 2020b.

IRENA. **Renewable Energy Cost Analysis - Concentrating Solar Power**. Abu Dhabi: International Renewable Energy Agency, 2012. Available from: https://irena.org/publications/2012/Jun/Renewable-Energy-Cost-Analysis---Concentrating-Solar-Power. Visited on: 1 Apr. 2021.

IRENA. **Renewable Power Generation Costs in 2018**. Abu Dhabi: International Renewable Energy Agency, 2019.

IRENA. **Renewable Power Generation Costs in 2020**. Abu Dhabi: International Renewable Energy Agency, 2021.

JONES-ALBERTUS, Becca. **Confronting the Duck Curve: How to Address Over-Generation of Solar Energy**. [S.l.: s.n.], 2017. Available from: https://www.energy.gov/eere/articles/confronting-duck-curve-how-address-over-generation-solar-energy. Visited on: 5 Oct. 2021.

JÜLCH, Verena. Comparison of electricity storage options using levelized cost of storage (LCOS) method. en. **Applied Energy**, v. 183, p. 1594–1606, Dec. 2016. DOI: 10.1016/j.apenergy.2016.08.165.

KALOGIROU, Soteris A. **Solar Energy Engineering**. [S.l.]: Elsevier, 2014. DOI: 10.1016/C2011-0-07038-2. Available from: https://linkinghub.elsevier.com/retrieve/pii/C20110070382. Visited on: 13 Jan. 2021.

KALOGIROU, Soteris A. Solar thermal collectors and applications. en. **Progress in Energy and Combustion Science**, v. 30, n. 3, p. 231–295, 2004. DOI: 10.1016/j.pecs.2004.02.001.

KEARNEY, D. et al. Engineering aspects of a molten salt heat transfer fluid in a trough solar field. en. **Energy**, v. 29, n. 5-6, p. 861–870, Apr. 2004. DOI: 10.1016/S0360-5442(03)00191-9.

KLASING, Freerk; ODENTHAL, Christian; TROST, Benjamin; HIRSCH, Tobias; BAUER, Thomas. Techno-economic assessment for large scale thermocline filler TES systems in a molten salt parabolic trough plant. In: p. 090017. DOI: 10.1063/1.5067111. Available from: http://aip.scitation.org/doi/abs/10.1063/1.5067111. Visited on: 12 Aug. 2020.

KRARTI, Moncef. **Optimal Design and Retrofit of Energy Efficient Buildings, Communities, and Urban Centers**. [S.l.]: Elsevier, 2018. DOI: 10.1016/C2016-0-02074-0. Available from: https://linkinghub.elsevier.com/retrieve/pii/C20160020740. Visited on: 18 June 2021.

KRYZA, Frank. The power of light : the epic story of man's quest to harness the Sun. en, p. 317, 2003.

KURUP, Parthiv; TURCHI, Craig S. **Parabolic Trough Collector Cost Update for the System Advisor Model (SAM)**. en. [S.l.], Nov. 2015. nrel/tp–6a20–65228, 1227713. DOI: 10.2172/1227713. Available from: http://www.osti.gov/servlets/purl/1227713/. Visited on: 7 Apr. 2021.

LEIVA-ILLANES, Roberto; ESCOBAR, Rodrigo; CARDEMIL, José M.; ALARCÓN-PADILLA, Diego-César. Thermoeconomic assessment of a solar polygeneration plant for electricity, water, cooling and heating in high direct normal irradiation conditions. en. **Energy Conversion and Management**, v. 151, p. 538–552, Nov. 2017. DOI: 10.1016/j.enconman.2017.09.002.

LI, Pei-Wen; CHAN, Cho Lik. **Thermal energy storage analyses and designs**. London, United Kingdom: Academic Press, an imprint of Elsevier, 2017. OCLC: ocn967501542.

LIU, Ming; STEVEN TAY, N.H.; BELL, Stuart; BELUSKO, Martin; JACOB, Rhys; WILL, Geoffrey; SAMAN, Wasim; BRUNO, Frank. Review on concentrating solar power plants and new developments in high temperature thermal energy storage technologies. en. **Renewable and Sustainable Energy Reviews**, v. 53, p. 1411–1432, Jan. 2016. DOI: 10.1016/j.rser.2015.09.026.

LOPES, Telma; FASQUELLE, Thomas; SILVA, Hugo G. Pressure drops, heat transfer coefficient, costs and power block design for direct storage parabolic trough power plants running molten salts. en. **Renewable Energy**, v. 163, p. 530–543, Jan. 2021. DOI: 10.1016/j.renene.2020.07.110.

LOVEGROVE, Keith; STEIN, Wes. **Concentrating solar power technology: principles, developments and applications**. Duxford, United Kingdom: Woodhead Publishing, 2020. OCLC: 1224579772. Available from: https://www.sciencedirect.com/science/book/9780128199701. Visited on: 20 Aug. 2021.

MALAGUETA, Diego; SZKLO, Alexandre; BORBA, Bruno Soares Moreira Cesar; SORIA, Rafael; ARAGÃO, Raymundo; SCHAEFFER, Roberto; DUTRA, Ricardo. Assessing incentive policies for integrating centralized solar power generation in the Brazilian electric power system. en. **Energy Policy**, v. 59, p. 198–212, Aug. 2013. DOI: 10.1016/j.enpol.2013.03.029.

MAO, Qianjun. Recent developments in geometrical configurations of thermal energy storage for concentrating solar power plant. en. **Renewable and Sustainable Energy Reviews**, v. 59, p. 320–327, June 2016. DOI: 10.1016/j.rser.2015.12.355.

MARTINS, João Humberto Serafim; OLIVEIRA, Lauro Augusto Jerônimo de; BAZZO, Edson; PASSOS, Júlio César. Comparative analysis of design point direct normal irradiance specification alternatives. en. In: COBEM. Florianópolis: ACBM, Nov. 2021. P. 1.

MARTINS, João Humberto Serafim; VELASQUEZ, Roberto Miguel Gutierrez; SILVA, Fabricio Polifke da; PASSOS, Júlio César. Direct Normal Irradiance forecasting using Numerical Weather Prediction and separation models. In: PROCEEDINGS of the 18th Brazilian Congress of Thermal Sciences and Engineering. Bento Gonçalves: ABCM, Nov. 2020. DOI: 10.26678/ABCM.ENCIT2020.CIT20-0266. Available from: http://abcm.org.br/anais-de-eventos/CIT20/0266. Visited on: 20 Apr. 2021.

MARUGÁN-CRUZ, Carolina; SERRANO, D.; GÓMEZ-HERNÁNDEZ, J.; SÁNCHEZ-DELGADO, S. Solar multiple optimization of a DSG linear Fresnel power plant. en. **Energy Conversion and Management**, v. 184, p. 571–580, Mar. 2019. DOI: 10.1016/j.enconman.2019.01.054.

MONTES, M.J.; ABÁNADES, A.; MARTÍNEZ-VAL, J.M. Performance of a direct steam generation solar thermal power plant for electricity production as a function of the solar multiple. en. **Solar Energy**, v. 83, n. 5, p. 679–689, May 2009a. DOI: 10.1016/j.solener.2008.10.015.

MONTES, M.J.; ABÁNADES, A.; MARTÍNEZ-VAL, J.M.; VALDÉS, M. Solar multiple optimization for a solar-only thermal power plant, using oil as heat transfer fluid in the parabolic trough collectors. en. **Solar Energy**, v. 83, n. 12, p. 2165–2176, Dec. 2009b. DOI: 10.1016/j.solener.2009.08.010.

MORAN, Michael J.; SHAPIRO, Howard N. (Eds.). **Fundamentals of engineering thermodynamics**. 8th ed. Hoboken, N.J: Wiley, 2014. OCLC: ocn879865441.

NREL. **System Advisor Model (SAM) Case Study: Andasol-1**. [S.l.], 2013.

OUYANG, Xiaoling; LIN, Boqiang. Levelized cost of electricity (LCOE) of renewable energies and required subsidies in China. en. **Energy Policy**, v. 70, p. 64–73, July 2014. DOI: 10.1016/j.enpol.2014.03.030.

PALACIOS, A.; BARRENECHE, C.; NAVARRO, M.E.; DING, Y. Thermal energy storage technologies for concentrated solar power – A review from a materials perspective. **Renewable Energy**, v. 156, p. 1244–1265, Aug. 2020. DOI: 10.1016/j.renene.2019.10.127.

PAWEL, Ilja. The Cost of Storage – How to Calculate the Levelized Cost of Stored Energy (LCOE) and Applications to Renewable Energy Generation. en. **Energy Procedia**, v. 46, p. 68–77, 2014. DOI: 10.1016/j.egypro.2014.01.159.

PELAY, Ugo; LUO, Lingai; FAN, Yilin; STITOU, Driss. Dynamic modeling and simulation of a concentrating solar power plant integrated with a thermochemical energy storage system. en. **Journal of Energy Storage**, v. 28, p. 101164, Apr. 2020. DOI: 10.1016/j.est.2019.101164.

PELAY, Ugo; LUO, Lingai; FAN, Yilin; STITOU, Driss; ROOD, Mark. Thermal energy storage systems for concentrated solar power plants. **Renewable and Sustainable Energy Reviews**, v. 79, p. 82–100, Nov. 2017. DOI: 10.1016/j.rser.2017.03.139.

PEREIRA, Enio Bueno et al. **Atlas brasileiro de energia solar**. 2. ed. São José dos Campos: INPE, 2017.

PETROLLESE, Mario; COCCO, Daniele; CAU, Giorgio; COGLIANI, Euro. Comparison of three different approaches for the optimization of the CSP plant scheduling. en. **Solar Energy**, v. 150, p. 463–476, July 2017. DOI: 10.1016/j.solener.2017.04.060.

QGIS DEVELOPMENT TEAM. **QGIS version 3.20.1-Odense**. [S.l.]: Open Source Geospatial Foundation, 2009. Available from: http://qgis.osgeo.org.

RAADE, Justin W.; PADOWITZ, David. Development of Molten Salt Heat Transfer Fluid With Low Melting Point and High Thermal Stability. en. **Journal of Solar Energy Engineering**, v. 133, n. 3, p. 031013, Aug. 2011. DOI: 10.1115/1.4004243.

REN21. **Renewables 2018. Global status report**. Paris, 2018. Available from: https://www.ren21.net/wp-content/uploads/2019/05/GSR2018_Full-Report_English.pdf.

REN21. **Renewables 2021 Global Status Report**. Paris, 2021. Available from: https://www.ren21.net/wp-content/uploads/2019/05/GSR2018_Full-Report_English.pdf.

RIFFELMANN, K.; RICHERT, T.; NAVA, P.; SCHWEITZER, A. Ultimate Trough® – A Significant Step towards Cost-competitive CSP. en. **Energy Procedia**, v. 49, p. 1831–1839, 2014. DOI: 10.1016/j.egypro.2014.03.194.

RITCHIE, Hannah; ROSER, Max. CO2 and Greenhouse Gas Emissions. **Our World in Data**, 2020a.

RITCHIE, Hannah; ROSER, Max. Energy. **Our World in Data**, 2020b.

SCHMIDT, Oliver; MELCHIOR, Sylvain; HAWKES, Adam; STAFFELL, Iain. Projecting the Future Levelized Cost of Electricity Storage Technologies. en. **Joule**, v. 3, n. 1, p. 81–100, Jan. 2019. DOI: 10.1016/j.joule.2018.12.008.

SEITZ, M.; CETIN, P.; ECK, M. Thermal Storage Concept for Solar Thermal Power Plants with Direct Steam Generation. en. **Energy Procedia**, v. 49, p. 993–1002, 2014. DOI: 10.1016/j.egypro.2014.03.107.

SHARMA, R.K.; GANESAN, P.; TYAGI, V.V.; METSELAAR, H.S.C.; SANDARAN, S.C. Developments in organic solid–liquid phase change materials and their applications in

thermal energy storage. en. **Energy Conversion and Management**, v. 95, p. 193–228, May 2015. DOI: 10.1016/j.enconman.2015.01.084.

SOLARGIS. **Solar resource maps of Brazil**. English. [S.l.: s.n.], 2019. Available from: https://solargis.com/maps-and-gis-data/download/brazil. Visited on: 7 July 2020.

SOLARPACES. **Concentrating Solar Power Projects**. [S.l.: s.n.], Mar. 2021. Número de chamada: 5. Available from: https://solarpaces.nrel.gov/.

STARKE, Allan R. **Analise exergoeconômica de uma central de concentração solar de coletores cilindro-parabólicos hibridizada com combustível fóssil e sistema fotovoltaico**. 2019. Tese de Doutorado em Engenharia Mecânica – Universidade Federal de Santa Catarina, Florianópolis.

STEAG. **EBSILON Professional Online Help**. Zwingenberg: STEAG Energy Services GmbH, 2021. Available from: https://help.ebsilon.com/EN/webframe.html#Conventions.html. Visited on: 14 Aug. 2020.

STEAG. **EBSILON®Professional Version 15.00**. Zwingenberg: STEAG Energy Services GmbH, 2020. Version 15.00. Available from: https://www.steag-systemtechnologies.com/en/products/ebsilon-professional/. Visited on: 14 Aug. 2020.

STRAUB, Jeremy. In search of technology readiness level (TRL) 10. en. **Aerospace Science and Technology**, v. 46, p. 312–320, Oct. 2015. DOI: 10.1016/j.ast.2015.07.007.

TEMLETT, Robert. **Dynamic process modelling of the HPS2 solar thermal molten salt parabolic trough test facility**. 2018. Dissertação de Mestrado em Engenharia Mecânica – University of Cape Town, Cape Town. Available from: http://hdl.handle.net/11427/29990.

TIAN, Y.; ZHAO, C.Y. A review of solar collectors and thermal energy storage in solar thermal applications. en. **Applied Energy**, v. 104, p. 538–553, Apr. 2013. DOI: 10.1016/j.apenergy.2012.11.051.

TURCHI, Craig S. **Parabolic Trough Reference Plant for Cost Modeling with the Solar Advisor Model (SAM)**. en. [S.l.], July 2010. nrel/tp–550–47605, 983729. DOI: 10.2172/983729. Available from: http://www.osti.gov/servlets/purl/983729-0gy2U4/. Visited on: 5 Oct. 2021.

TURCHI, Craig S.; BOYD, Matthew; KESSELI, Devon; KURUP, Parthiv; MEHOS, Mark S.; NEISES, Ty W.; SHARAN, Prashant; WAGNER, Michael J.; WENDELIN, Timothy. **CSP Systems Analysis - Final Project Report**. en. [S.l.], May 2019. nrel/tp–5500–72856, 1513197. DOI: 10.2172/1513197. Available from: http://www.osti.gov/servlets/purl/1513197/. Visited on: 7 Apr. 2021.

TURCHI, Craig S.; VIDAL, Judith; BAUER, Matthew. Molten salt power towers operating at 600–650 °C: Salt selection and cost benefits. en. **Solar Energy**, v. 164, p. 38–46, Apr. 2018. DOI: 10.1016/j.solener.2018.01.063.

VIRTANEN, Pauli et al. SciPy 1.0: Fundamental Algorithms for Scientific Computing in Python. **Nature Methods**, v. 17, p. 261–272, 2020. DOI: 10.1038/s41592-019-0686-2.

WAGNER; GILMAN, P. **Technical Manual for the SAM Physical Trough Model**. en. [S.l.], June 2011. nrel/tp–5500–51825, 1016437. DOI: 10.2172/1016437. Available from: http://www.osti.gov/servlets/purl/1016437/. Visited on: 7 Apr. 2021.

WAGNER, Patrick Hubert. **Thermodynamic simulation of solar thermal power stations with liquid salt as heat transfer fluid**. 2012. PhD thesis.

WANG, Zhifeng. **Design of Solar Thermal Power Plants**. [S.l.]: Academic Press, 2019. DOI: 10.1016/B978-0-12-815613-1.00003-1. Available from: https://www.sciencedirect.com/science/article/pii/B9780128156131000031.

WESTON, Kenneth C. **Energy conversion**. St. Paul: West Pub. Co, 1992.

WORLD BANK. **The World Bank Annual Report 2020**. [S.l.]: World Bank, Washington, DC, Oct. 2020. DOI: 10.1596/978-1-4648-1619-2. Available from: http://hdl.handle.net/10986/34406. Visited on: 20 Aug. 2021.

ZAVERSKY, Fritz; GARCÍA-BARBERENA, Javier; SÁNCHEZ, Marcelino; ASTRAIN, David. Transient molten salt two-tank thermal storage modeling for CSP performance simulations. en. **Solar Energy**, v. 93, p. 294–311, July 2013. DOI: 10.1016/j.solener.2013.02.034.

APPENDIX A – LIST OF PUBLICATIONS

In the scope of this research, several technical and academic studies were produced, this being one of the objectives defined by the ANEEL/CGT Eletrosul R&D project. In addition to this study, the following documents were produced by the author.

Journal articles under review

FERREIRA, Willian Mendes; MARTINS, João Humberto Serafim; JUNIOR, Jorge AlbertoLewis Esswein; FILHO, Victor César Pigozzo; PASSOS, Júlio César. Modeling of a linear Fresnel direct steam generation solar thermal power plant with sensible-latent thermal energy storage: A case study for Northeastern Brazil. en. **Energy**, p. 37.

Conference papers featured in proceedings

MARTINS, João Humberto Serafim; OLIVEIRA, Lauro Augusto Jerônimo de; BAZZO, Edson; PASSOS, Júlio César. Comparative analysis of design point direct normal irradiance specification alternatives. en. In: COBEM. Florianópolis: ACBM, Nov. 2021. P. 1.

MARTINS, João Humberto Serafim; PASSOS, Julio César. Assessment of concentrated solar power design parameters for levelized cost of energy reduction and capacity factor enhancement. In: PROCCEEDINGS SWC 2021. [S.l.: s.n.], Oct. 2021.

MARTINS, João Humberto Serafim; VELASQUEZ, Roberto Miguel Gutierrez; SILVA, Fabricio Polifke da; PASSOS, Júlio César. Direct Normal Irradiance forecasting using Numerical Weather Prediction and separation models. In: PROCEEDINGS of the 18th Brazilian Congress of Thermal Sciences and Engineering. Bento Gonçalves: ABCM, Nov. 2020. DOI: 10.26678/ABCM.ENCIT2020.CIT20-0266. Available from: http://abcm.org.br/anais-de-eventos/CIT20/0266. Visited on: 20 Apr. 2021.

MILANI, Rodrigo; MARTINS, João Humberto Serafim; VELASQUEZ, Roberto Miguel Gutierrez; POZZATTI, Luis Felipe; MEYER, Breno Torres. Análise de competitividade e penetração de plantas CSP de coletores cilindro-parabólicos no mercado de energia brasileiro. In: ANAIS CBENS 2020. Fortaleza: ABENS, Oct. 2020. Available from: https://anaiscbens.emnuvens.com.br/cbens/article/view/798.

VELASQUEZ, Roberto Miguel Gutierrez; MARTINS, João Humberto Serafim; MILANI, Rodrigo; POZZATTI, Luis Felipe; MEYER, Breno Torres. Análise técnico-econômica comparativa das tecnologias de concentração heliotérmica em localidades brasileiras. In: CIES 2020 - Comunicações. Lisboa: [s.n.], Nov. 2020. Publisher: LNEG - Laboratório Nacional de Energia e Geologia. DOI: 10.34637/CIES2020.1.2032. Available from: http://hdl.handle.net/10400.9/3370. Visited on: 20 Apr. 2021.

VELASQUEZ, Roberto Miguel Gutierrez; MARTINS, João Humberto Serafim; POZZATTI, Luis Felipe; ROSA, Hobed; GAZOLI, Jonas Rafael. Determinação da cadeia de nacionalização tecnológica para geração heliotérmica. pt. In: ANAIS XXV SNPTEE. Belo Horizonte: [s.n.], Nov. 2019a. P. 9.

VELASQUEZ, Roberto Miguel Gutierrez; MILANI, Rodrigo; GAZOLI, Jonas; KULZER, Dirceu; ROSA, Hobed; POZZATTI, Luis Felipe; MARTINS, João Humberto Serafim. Regulatory impacts on CSP distributed generation enterprises in Brazil. en. In: BOOK of Abstracts. Paris: [s.n.], Apr. 2019b. P. 7.

APPENDIX B – PARAMETRIC ANALYSIS RESULTS

The following tables present the numeric result from the parametric analysis, performed to identify the relation between the SM and TES capacity at the LCOE and the CF. The domain of the input variables is:

- *Solar multiple.* between 1.00 and 3.00, with a 0.25 interval;
- *Storage capacity.* between 0 and 12 hours, with a 1 hour interval.

It is important to highlight the configurations with $TES_{cap} > 0$ are covered by topologies (i) - which uses synthetic oil as HTF - and (iii) - which uses molten salt as HTF. Plants with $TES_{cap} = 0$ are simulated using topologies (ii) and (iv).

B.1 LEVELIZED COST OF ENERGY

Tables B.1 and B.2 presents the LCOE outputs from the parametric analysis.

Table B.1 – Levelized cost of energy, for topologies (i) and (ii), which use synthetic oil as heat transfer fluid.

SM [-]	Storage capacity [h]												
	0	1	2	3	4	5	6	7	8	9	10	11	12
1.00	20.7	24.1	25.5	26.9	28.3	29.6	31.0	32.4	33.7	35.1	36.5	37.9	39.2
1.25	18.2	19.9	20.9	21.9	23.0	24.0	25.1	26.1	27.1	28.2	29.2	30.3	31.4
1.50	17.4	17.7	18.3	19.0	19.9	20.7	21.6	22.4	23.2	24.1	25.0	25.8	26.6
1.75	17.5	16.9	17.1	17.5	18.1	18.8	19.5	20.2	20.9	21.7	22.4	23.2	23.9
2.00	18.0	17.0	16.8	17.0	17.3	17.8	18.4	19.0	19.7	20.3	21.0	21.6	22.3
2.25	18.6	17.4	17.1	16.9	17.1	17.4	17.9	18.5	19.1	19.7	20.3	20.9	21.5
2.50	19.4	18.0	17.5	17.3	17.2	17.4	17.9	18.4	19.0	19.5	20.1	20.6	21.2
2.75	20.2	18.7	18.1	17.8	17.6	17.7	18.0	18.5	19.0	19.6	20.1	20.6	21.2
3.00	21.9	19.5	18.8	18.3	18.1	18.0	18.3	18.8	19.3	19.8	20.4	20.9	21.4

Source: Elaborated by the author.

Table B.2 – Levelized cost of energy, for topologies (iii) and (iv), which use molten salts as heat transfer fluid.

SM [-]	Storage capacity [h]												
	0	**1**	**2**	**3**	**4**	**5**	**6**	**7**	**8**	**9**	**10**	**11**	**12**
1.00	20.7	26.0	26.5	27.0	27.4	27.9	28.4	28.8	29.3	29.7	30.2	30.7	31.1
1.25	18.1	21.5	21.8	22.2	22.5	22.9	23.2	23.6	23.9	24.3	24.7	25.0	25.4
1.50	17.4	18.7	18.7	18.9	19.2	19.5	19.8	20.1	20.4	20.7	21.0	21.3	21.6
1.75	17.5	17.5	17.1	17.1	17.2	17.4	17.6	17.8	18.1	18.3	18.6	18.8	19.1
2.00	17.9	17.1	16.5	16.2	16.1	16.1	16.2	16.4	16.6	16.8	17.0	17.2	17.5
2.25	18.4	17.4	16.5	16.0	15.6	15.4	15.4	15.5	15.5	15.7	15.9	16.1	16.2
2.50	19.1	17.9	16.8	16.1	15.6	15.2	15.0	14.9	15.0	15.0	15.1	15.2	15.4
2.75	19.9	18.5	17.3	16.4	15.8	15.3	15.0	14.7	14.6	14.6	14.6	14.7	14.8
3.00	20.6	19.1	17.9	16.9	16.1	15.5	15.1	14.7	14.5	14.4	14.3	14.3	14.3

Source: Elaborated by the author.

B.2 CAPACITY FACTOR

Tables B.3 and B.4 presents the CF outputs from the parametric analysis.

Table B.3 – Capacity factor, in percentage, for topologies (i) and (ii), which use synthetic oil as heat transfer fluid.

SM [-]	Storage capacity [h]												
	0	**1**	**2**	**3**	**4**	**5**	**6**	**7**	**8**	**9**	**10**	**11**	**12**
1.00	21.1	19.8	19.8	19.8	19.8	19.8	19.8	19.8	19.8	19.8	19.8	19.8	19.8
1.25	26.6	26.5	26.5	26.5	26.5	26.5	26.5	26.5	26.5	26.4	26.4	26.4	26.4
1.50	30.5	32.5	33.0	33.1	33.1	33.0	33.0	33.0	33.0	32.9	32.9	32.9	32.9
1.75	33.0	36.7	38.1	38.7	38.9	39.0	39.0	38.9	38.9	38.8	38.8	38.7	38.7
2.00	34.6	39.3	41.4	42.8	43.4	43.8	43.9	43.9	43.8	43.7	43.7	43.7	43.6
2.25	35.9	41.0	43.6	45.6	46.8	47.5	47.7	47.7	47.6	47.6	47.6	47.5	47.4
2.50	36.8	42.3	45.1	47.4	49.1	50.2	50.5	50.5	50.5	50.4	50.4	50.4	50.3
2.75	37.6	43.2	46.1	48.7	50.8	52.1	52.8	52.8	52.8	52.7	52.7	52.6	52.6
3.00	38.2	43.9	46.9	49.7	52.0	53.7	54.4	54.4	54.4	54.3	54.3	54.2	54.2

Source: Elaborated by the author.

Table B.4 – Capacity factor, in percentage, for topologies (iii) and (iv), which use molten salts as heat transfer fluid.

SM [-]	**Storage capacity [h]**												
	0	**1**	**2**	**3**	**4**	**5**	**6**	**7**	**8**	**9**	**10**	**11**	**12**
1.00	22.6	18.9	18.9	18.9	18.9	18.9	18.9	18.9	19.0	19.0	19.0	19.0	19.0
1.25	28.0	24.9	24.9	24.9	24.9	24.9	24.9	24.9	24.9	24.9	24.9	24.9	24.9
1.50	31.4	30.9	31.4	31.5	31.4	31.4	31.4	31.4	31.3	31.3	31.3	31.3	31.3
1.75	33.6	35.5	36.8	37.4	37.7	37.8	37.8	37.7	37.7	37.7	37.6	37.6	37.6
2.00	35.0	38.5	40.6	42.1	42.9	43.4	43.7	43.7	43.7	43.7	43.7	43.6	43.5
2.25	36.0	40.3	43.1	45.2	46.8	47.9	48.6	49.0	49.3	49.5	49.5	49.4	49.4
2.50	36.8	41.5	44.7	47.4	49.5	51.3	52.7	53.5	54.1	54.5	54.7	54.8	54.9
2.75	37.4	42.3	45.7	48.8	51.5	53.7	55.6	57.1	58.3	59.0	59.4	59.9	60.1
3.00	37.8	42.3	45.7	48.8	51.5	53.7	55.6	57.1	58.3	59.0	59.4	59.9	60.1

Source: Elaborated by the author.